CHAPTER 1

Introduction

1.1 Background

Cost effective and highly efficient renewable energy is becoming ever more important due to the rising energy price and the serious issue of global warming from burning the fossil fuels. Among these, solar cells, which utilize a non-exhaustible and green solar energy, are being developed as a promising solution. Especially, organic solar cells (OSCs)[1-3] offer a promising alternative to inorganic solar cells, which have been the main stream of solar cell researches, due to their low cost, easy fabrication, and compatibility with flexible substrates over a large area. Since their first report,[4] the power conversion efficiency (PCE) of OSCs has steadily increased and now reached up to 4-7 %.[5-8] However, further enhancement of the PCE together with the low-cost fabrication is still required for practical applications.[9]

In the early 1990s, PCEs in single component intrinsic semiconductor type OSCs were still limited to less than 0.1 %[10-13] (Figure 1.1a). This was mainly due to the weak driving force to dissociate the relatively high binding energy of photo-generated excitons of organic semiconducting materials, ranging between 0.1 and 1 eV,[14-18] and secondly the free carriers had the very low mobilities even though they were created by exciton dissociation in photoactive layer. One key OSC structures to solve these problems was made by introducing another layer, which could act as electron-acceptor, to the electron-

donor photoactive layer in order for both layers to have offset energy bands.[1,4,20] Excitons generated near the heterojunction could diffuse to the interface between two semiconductors and undergo forward electron or hole transfer (Figure 1.1b). This charge transfer led to the spatial separation of the electron and hole, thereby preventing direct recombination and allowing the transport of electrons to one electrode and holes to the other.

The external quantum efficiency (EQE) of OSC based on exciton dissociation at a donor-acceptor interface is $\eta_{EQE} = \eta_A \times \eta_{ED} \times \eta_{CC}$. Here, η_A is the absorption efficiency. The exciton diffusion efficiency, η_{ED}, is the fraction of photogenerated excitons that reaches a donor-acceptor interface before recombining. The carrier collection efficiency, η_{CC}, is the probability that a free carrier, generated at a donor-acceptor interface by dissociation of an exciton, reaches its corresponding electrode. Typically, in bilayer donor-acceptor OSC, η_{CC} is approaching almost 100%. Because there were essentially no minority free carriers in the undoped semiconductors, there was little chance of carrier recombination once the charges moved away from the interface, despite the long transit times to the electrodes. However, since the exciton diffusion length, which has been measured to be 4-20 nm[20-24] is typically an order of magnitude smaller than the thickness to fully absorb the light, a large fraction of the photogenerated excitons remains unused for photocurrent generation,[1] limiting η_{EQE} and hence the PCE of this type of planar junction cell.

This limitation was overcome by the concept of the bulk heterojunction (BHJ) (Figure 1.1c), where the donor and acceptor materials are intimately blended throughout the bulk,[25-27] In this way, excitons do not need to travel long distances to reach the donor-

acceptor interface, and charge separation can take place throughout the whole depth of the photoactive layer. Thus the active zone for photocurrent generation extends throughout the volume maximizing η_{ED}. However, due to the randomly distributed blend morphologies inducing the poor free carrier pathways, η_{CC} can be significantly decreased, therefore it is one of the most important tasks to optimize free charge carrier pathways while preserving the domain size within the exciton diffusion length for high efficiency BHJ OSC.

For this purpose, a number of works, based on poly(3-hexylthiophene) (P3HT) : [6,6]-phenyl C_{61} butyric acid methyl ester (PCBM) as a model system, have reported ways to optimize BHJ blends morphology. Nowadays, thermal annealing (TA) and solvent-assisted annealing (SAA) treatments after spin-casting the blend film are widely accepted as general approaches to control the blend morphology for high efficiency polymer solar cells, because well-organized interpenetrating networks composed of highly crystallized components can be achieved. However, recent works that investigated phase separation of components in the vertical direction (*i.e.* normal to the film and electrode surface) revealed that the BHJ structures fabricated by these methods do not have optimized morphology: a non-uniform vertical distribution exists with P3HT phase dominant near the cathode and PCBM phase dominant near the anode was observed. Such non-uniform distribution is opposite to the ideal solar cell structure that requires a donor rich phase near the anode and an acceptor rich phase near the cathode, and therefore unfavorable to charge transport to the electrodes. In addition, both annealing processes require relatively long processing time (*e.g.* tens of minutes for TA or a few hours for SAA) and spin-casting deposition can only be applied to small and rigid

substrate, making these approaches not suitable to practical large area and mass production of polymer solar cells. Even though high-speed fabrication processes on flexible substrates have been reported, their device performances still cannot compare to those of spin-casting based polymer solar cells, followed by further post-treatments. This is because the traditional high speed roll-to-roll coating method may not provide sufficient annealing time for crystallization and hence result in lower device efficiency. In order to solve these problems, we need an advanced processing inducing uniform and favorable vertical distribution and compatible to high speed fabrication such as roll-to-roll process.

More importantly, the most ideal OSC structure to achieve high efficiency OSCs is interdigitated networks of an electron-donor and an electron-acceptor material, as shown Figure 1.1d. It is desirable to limit the size of each domain to within the exciton diffusion length. By making such controlled nanoscale morphology between the donor and the acceptor, and having the donor-acceptor interface vertically oriented to the cathode and the anode, the excitons can be fully dissociated to electrons and holes, and can be efficiently transported to the electrodes before recombination, maximizing both η_{ED} and η_{CC}. There have been previous attempts to realize the idealized OSC structures, however, no one has successfully demonstrated these types of structures within 20 nm domain scale using the conjugate polymer and fullerene derivate as a donor and acceptor pair, which have shown the state-of-the-art PCE in the OSC research. One of the major challenges to realize this type of structure is the difficulty to access those periodic pillar and hole structures of tens of nanometer pitch. Electron beam lithography and focused ion beam (FIB) lithography are widely used methods to fabricate these types of patterns

for which conventional photolithography faces resolution limit. However, the time consuming process and the high cost associated with such techniques seriously restrict the large-scale production of high density nanopatterns. As alternatives, nanotemplate approaches using track-etched membrane[5] and anodized aluminum oxide (AAO) have been extensively used to produce tens of nanometer scale patterns. However the poor adhesion of template to a substrate, the harsh processing conditions to remove the template or the resolution of the patterns often limit these pattern transferring techniques.

Recently, the self-assembly behavior of diblock copolymers has drawn significant attentions for nanotemplate fabrication. It is well known that the self-organization of block copolymer can access complex nanostructures. The density and the dimension of such self-organized nanostructures are usually beyond the reach of typical conventional top-down nanofabrication techniques. Furthermore, various techniques that have been developed to control the orientation of the nanoscale morphology in the thin film make it possible for these self-organized nanostructures to be used as templates for various applications. Despite the numerous advantages of these nanotemplates fabricated by block copolymer self-assembly, the long processing time needed to develop the self-assembled structures has drastically reduced the potential impact of this versatile nanopatterning technique. To overcome this limitation, we need reliable and practical methods such as nanoimprint lithography (NIL) for high speed nanopatterning. Such an approach represents a big step forward to mass production of nanostructures with dimension, density and areal coverage only accessible by the block copolymer self-assembly process.

As another promising approach for efficient OSC, the effects of plasmonic nanostructures and light trapping structures on OSCs are recently highlighted, because those nanostructures potentially provide an effective means to improve the efficiency of OSCs by enhancing the absorption of light even in a very thin organic material layer; increasing η_A without decreasing η_{ED} or η_{CC}. This approach in principle can address the mismatch problems between the short exciton diffusion length in organic semiconductor materials and the large thickness required to fully absorb sunlight.

Surface plasmon resonance (SPR) has been exploited in many photonic applications due to their unique capabilities of localizing light at nanoscale dimensions. They are surface waves whose electromagnetic field is confined to the vicinity of the metal dielectric interface. When the condition of the resonance is fulfilled, this confinement leads to an enhancement of the electromagnetic field at the interface and this aspect has been utilized in many nearfield surface plasmon-based applications. Since the thickness of the organic semiconductors in OSCs is about several tens of nanometer, which coincides with the field decay length of SPR in typical dielectric layer, SPR enhancement is naturally suited to increase the optical absorption of the organic semiconductors. Though there have been previous reports to demonstrated relative enhancement of the optical absorption by the SPR effect in OSCs, only limited enhancement of PCE near the resonance wavelength due to the overall transmittance reduction, induced by the additional metal structure, was achieved or non-regular nanoparticles having the difficulties in controlling the dimension and uniformity are introduced in OSCs. To make this approach practical, an effective fabrication technique that can produce large-area and uniform metallic nanostructures are needed. Furthermore, if we can add periodic

nanostructure at the backside of OSC, we can further enhance the optical path length across a broad wavelength range of incident light.

We can also focus on alternative applications of OSCs, which complements the efforts in improving its PCE and practical fabrication methods, by considering their versatility. By integrating the OSCs with other functional devices, we can still find ways that OSC researches have to pursue in the future. Recently, a number of approaches have been explored to scavenge energy from environments, however, little attention has been paid to the significant light energy wasted in displays used in our everyday lives. For example, in the prevailing liquid crystal displays (LCD), only 3-8 % of the backlight can reaches our eyes, where most of light energy is absorbed by the colorant-based filters and polarizers. Therefore, approaches that can recycle or harvest the absorbed energy to generate useful electrical power could lead to revolutionary energy-saving e-media. This aspect is especially promising when considering the widely used devices such as e-book that consumes little power, or mobile devices (such as cell phones) that are in standby mode 95 % of the time. Such dual-functionality can also be exploited to make colored OPV panels for both decoration and light energy harvesting.

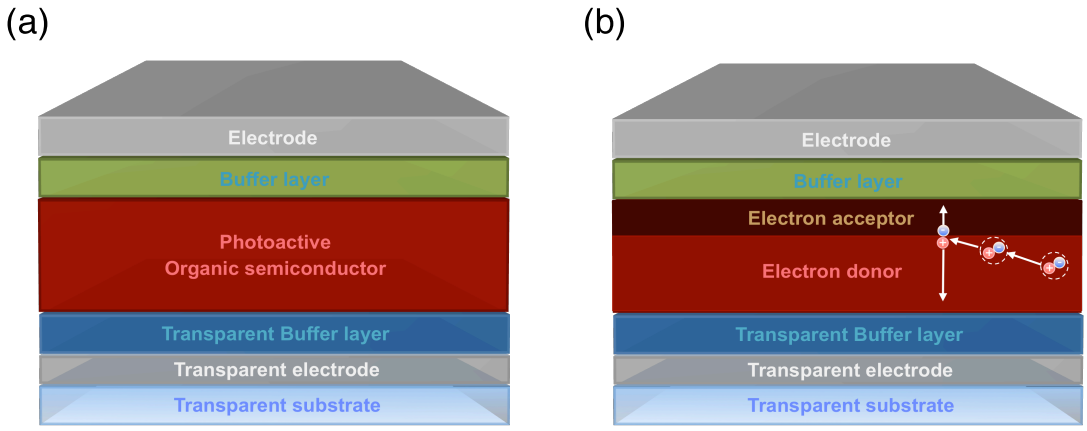

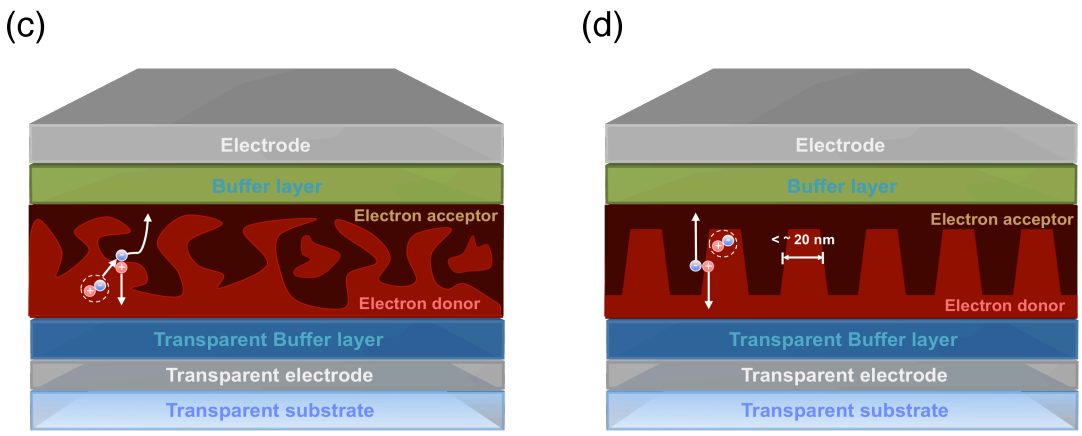

Figure 1.1 Four device architectures of conjugated polymer-based photovoltaic cells: (a) Single-layer OSC; (b) Bilayer OSC; (c) Disordered bulk heterojunction; (d) Ordered heterojunction.

1.2 Goal of research

I have been dedicated to developing ways to realize low-cost, high efficiency and scalable OSCs. For this purpose, my research has been focused on various nanostructures, which can be usable to maximize the performances of OSCs, and the effective fabrication processes to achieve those nanostructures. Furthermore novel device concepts based on those nanostructures have been investigated.

Firstly, nanostructures in photoactive layers were controlled to achieve more efficient OSC devices. A new process named as evaporation of solvent through surface encapsulation and with induced alignment of polymer chains by applied pressure (ESSENCIAL) inducing superior nanoscale BHJ morphology compared with conventional spin-casting based thermal and solvent annealed structures was developed, and new type of heterojunction nanostructure based on bilayer layout, approaching about 100% internal quantum efficiency, was introduced. Moreover, sub-20 nm scale nanopillar

structures were fabricated to realize the ideal interdigitated heterojunction. All these nanostructures could be realized by advanced processing that can be extended to high-speed manufacturing toward low-cost and highly efficient OSCs. Secondly, various nanostructures such as plasmonic nanostructures and light trapping structures were successfully introduced to OSC devices, ultimately improving the performance of OSCs. Lastly, photonic nanostructures that can simultaneously function as color filters and solar cells are designed, and their versatile properties are studied using simulation and experiments.

1.3 Organization of thesis

The organization of the thesis is as follows: Chapter 2 introduces the ESSENCIAL process that can induce optimized BHJ morphology, and its application to roll-to-roll process is also addressed in this chapter. Chapter 3 describes the way to further improve the PCE of BHJ OSCs by controlling the interface between photoactive layer and electrode. Chapter 4 presents a new type of heterojunction photoactive layer based on bilayer structure giving superior performance compared with BHJ structure. Chapter 5 introduces the efficient method to fabricate sub-20 nm nanopillar structure for ideal interdigitated heterojunction. Chapter 6 describes the effect of plasmonic nanostructures and light trapping structures on OSC devices for light management toward higher PCE. Chapter 7 shows the new conceptual dual-function devices working as color filter and solar cell for versatility of OSC devices. Chapter 8 summarizes all the work done in this thesis.

1.4 References

1. Peumans, P, Yakimov, A. & Forrest, S. R. Small molecular weight organic thin-film photodetectors and solar cells. *J. Appl. Phys.* **2003**, 93, 3693-3723.
2. Hoppe, H., Sariciftci, N. S. Organic solar cells: An overview. *J. Mater. Res.* **2004**, 19, 1924-1945.
3. Coakley, K. M. & McGehee, M. D. Conjugated polymer photovoltaic Cells. *Chem. Mater.* **2004**, 16, 4533-4542.
4. Tang, C. W. Two-layer organic photovoltaic cell. *Appl. Phys. Lett.* **1986**, 48, 183-185.
5. Li, G., Shrotriya, V., Huang, J., Yao, Y., Moriarty, T., Emery, K & Yang, Y. High-efficiency solution processable polymer photovoltaic cells by self-organization of polymer blends. *Nature Mater.* **2005**, 4, 864-868.
6. Ma, W., Yang, C., Gong, X., Lee, K. & Heeger, A. J. Thermally stable, efficient polymer solar cells with nanoscale control of the interpenetrating network morphology. *Adv. Funct. Mater.* **2005**, 15, 1617-1622.
7. Kim, J. Y., Lee, K., Coates, N. E., Moses, D., Nguyen, T.-Q., Dante, M. & Heeger, A. J. Efficient tandem polymer solar cells fabricated by all-solution processing. *Science* **2007**, 317, 222-225.
8. Park, S. H., Roy, A., Beaupre, S., Cho, S., Coates, N., Moon, J. S., Moses, D., Leclerc, M., Lee, K. & Heeger, A. J. Bulk heterojunction solar cells with internal quantum efficiency approaching 100%. *Nature Photon.* **2009**, 3, 297-302.
9. Gilles, D., Markus, C. S. & Christoph, J. B. Polymer-fullerene bulk-heterojunction solar cells. *Adv. Mater.* **2009**, 21, 1323-1338.

10. Karg, S., Riess, W., Dyakonov, V. & Schwoerer, M. Electrical and optical characterization of poly(phenylene-vinylene) light emitting diodes. *Synth. Met.* **1993**, 54, 427-433.

11. Yu, G., Zhang, C. & Heeger, A. J. Dual-function semiconducting polymer devices: light-emitting and photodetecting diodes. *Appl. Phys. Lett.* **1994**, 64, 1540-1542.

12. Yu, G., Pakbaz, K. & Heeger, A. J. Semiconducting polymer diodes: large size, low cost photodetectors with excellent visible–ultraviolet sensitivity. *Appl. Phys. Lett.* **1994**, 64, 3422-3424.

13. Marks, R. N., Halls, J. J. M., Bradley, D. D. C., Friend, R. H. & Holmes, A. B. The photovoltaic response in poly(*p*-phenylene vinylene) thin-film devices. *J. Phys.*: *Condens. Matter.* **1994**, 6, 1379-1394.

14. Pope, M. & Swenberg, C. E. Electronic processes in organic crystals and polymers; 2nd edn. Oxford University Press: New York, 1999.

15. Sariciftci, N. S. Primary photoexcitations in conjugated polymers: molecular exciton versus semiconductor band model; World Scientific: Singapore, 1997.

16. Chandross, M., Mazumdar, S., Jeglinski, S., Wei, X., Vardeny, Z. V., Kwock, E. W. & Miller, T. M. Excitons in poly(*para*-phenylenevinylene). *Phys. Rev. B* **1994**, 50, 14702-14705.

17. Campbell, I. H., Hagler, T. W., Smith, D. L. & Ferraris, J. P. Direct measurement of conjugated polymer electronic excitation energies using metal/polymer/metal structures. *Phys. Rev. Lett.* **1996**, 76, 1900-1903.

18. Knupfer, M. Exciton binding energies in organic semiconductors. *Appl. Phys. A* **2003**, 77, 623-626.

19. Sariciftci, N. D., Braun, D., Zhang, C., Srdanov, V. I., Heeger, A. J., Stucky, G. & Wudl, F. Semiconducting polymer-buckminsterfullerene heterojunctions: Diodes, photodiodes, and photovoltaic cells. *Appl. Phys. Lett.* **1993**, *62*, 585-587.

20. Halls, J. M., Pichler, K., Friend, R. H., Moratti, S. C. & Holmes, A. B. Exciton diffusion and dissociation in a poly(p-phenylenevinylene)/C_{60} heterojunction photovoltaic cell. *Appl. Phys. Lett.* **1996**, 68, 3120-3122.

21. Pettersson, L. A. A., Roman, L. S. & Inganäs, O. Modeling photocurrent action spectra of photovoltaic devices based on organic thin films. *J. Appl. Phys*. 1999, 86, 487-496.

22. Theander, M., Yartsev, A., Zigmantas, D., Sundström, V., Mammo, W., Anderson, M. R. & Inganäs, O. Photoluminescence quenching at a polythiophene/C_{60} heterojunction. *Phys. Rev. B* **2000**, 61, 12957-12963.

23. Savenije, T. J., Warman, J. M. & Goossens, A. Visible light sensitisation of titanium dioxide using a phenylene vinylene polymer. *Chem. Phys. Lett.* **1998**, 287, 148-153.

24. Haugeneder, A., Neges, M., Kallinger, C., Spirkl, W., Lemmer, U., Feldman, J., Scherf, U., Harth, E., Gugel, A. & Mullen, K. Exciton diffusion and dissociation in conjugated polymer/fullerene blends and heterostructures. *Phys. Rev. B* **1999**, 59, 15346-15351.

25. Yu, G. & Heeger, A. J. Charge separation and photovoltaic conversion in polymer composites with internal donor/acceptor heterojunctions. *J. Appl. Phys.* **1995**, 78, 4510-4515.

26. Yu, G., Gao, J., Hummelen, J. C., Wudl, F. & Heeger, A. J. Polymer photovoltaic cells: enhanced efficiencies via a network of internal donor-acceptor heterojunctions. *Science* **1995**, 270, 1789-1791.

27. Halls, J. J. M., Walsh, C. A., Greenham, N. C., Marseglia, E. A., Friend, R. H., Moratti, S. C. & Holmes, A. B. Efficient photodiodes from interpenetrating polymer networks. *Nature* **1995**, 376, 498-500.

CHAPTER 2

Facile Route to Polymer Solar Cells with Optimum Bulk Heterojunction Morphology Readily Applicable to a Roll-to-roll Process without Sacrificing High Device Performances

2.1 Introduction

Solar cells are being developed as a promising solution to the energy crisis and environmental pollution.[1] Among these, bulk heterojunction (BHJ) polymer solar cells have shown strong potential for low cost, easy processable and flexible solar cells with acceptable efficiencies.[2-7] As an example, BHJ polymer solar cell can also be fabricated by solution-based continuous roll-to-roll process as recently been demonstrated.[8-10] Polymer BHJ structures, which have been exploited to give the highest efficiencies for polymer solar cells, are composed of interpenetrating nanoscale networks of electron-donor (*e.g.* conjugated polymers) and electron-acceptor (*e.g.* soluble fullerene derivatives) with domain sizes on the order of exciton diffusion length and with large interfacial areas between the domains.[3-7] Therefore such network can facilitate efficient dissociation of photo-induced excitons at the domain interface. This advantage has made this approach a strong candidate for high efficiency polymer solar cells. However, randomly distributed blend morphologies in BHJ structures inevitably require external treatment to form effective pathway for the photo-generated charges to reach each electrode. Accordingly, optimizing blend morphology to provide effective charge pathway as well as large

interfacial area is one of the most crucial issues to achieve high efficiency polymer solar cells using BHJ structures.

For this purpose, a number of works, based on poly(3-hexylthiophene) (P3HT) : [6,6]-phenyl C_{61} butyric acid methyl ester (PCBM) as a model system, have reported ways to optimize BHJ blends morphology. Nowadays, thermal annealing (TA) and solvent-assisted annealing (SAA) treatments after spin-casting the blend film are widely accepted as general approaches to control the blend morphology for high efficiency polymer solar cells, because well-organized interpenetrating networks composed of highly crystallized components can be achieved.[5,6,11] However, recent works that investigated phase separation of components in the vertical direction (*i.e.* normal to the film and electrode surface) revealed that the BHJ structures fabricated by these methods do not have optimized morphology: a non-uniform vertical distribution exists with P3HT phase dominant near the cathode and PCBM phase dominant near the anode was observed.[12-15] Such non-uniform distribution is opposite to the ideal solar cell structure that requires a donor rich phase near the anode and an acceptor rich phase near the cathode, and therefore unfavorable to charge transport to the electrodes. In addition, both annealing processes require relatively long processing time (*e.g.* tens of minutes for TA[5] or a few hours for SAA[6]) and spin-casting deposition can only be applied to small and rigid substrate, making these approaches not suitable to practical large area and mass production of polymer solar cells. Even though high-speed fabrication processes on flexible substrates have been reported, their device performances still cannot compare to those of spin-casting based polymer solar cells, followed by further post-treatments.[8-10] This is because the traditional high speed roll-to-roll coating method may not provide

sufficient annealing time for crystallization and hence result in lower device efficiency.[8-10]

Here, we introduce a novel route that allows evaporation of solvent through surface encapsulation and with induced alignment (ESSENCIAL) of polymer chains by applied pressure. The essence of this approach is to utilize a gas-permeable cover layer for solvent evaporation that simultaneously protect the otherwise free surface and induce shear flow of the blend solution by an applied pressure. The process leads to optimized morphology, more uniform distribution and crystallinity of the components favorable for charge generation and transportation that cannot be achieved by conventional TA and SAA methods. Comparisons among structures fabricated by different methods were made by measurement of quantum efficiency, absorbance, X-ray photoelectron spectroscopy (XPS), and hole- and electron-mobilities. Furthermore, the effect of domain features of the components on efficient exciton dissociation were studied using atomic force microscopy (AFM) and photoluminescence (PL). The power conversion efficiency was obtained by *J-V* measurement based on isolated cathode geometry in order not to overestimate the efficiency commonly occurred in devices previously reported by using cross-bar electrode geometry.[16,17] Our results revealed that this new ESSENCIAL method not only induces much uniformly distributed interpenetrating continuous pathways having finer nanodomains with high crystallinity, but also is applicable to high-speed dynamic process which is ultimately demonstrated in a roll-to-roll process while preserving high device performances.

2.2 Experimental details

2.2.1 Device fabrication

Polymer solar cells have the following planar configuration: transparent substrate/ITO/PEDOT:PSS/P3HT:PCBM/LiF/Al. ITO coated substrates (Delta Technologies, LTD) were cleaned in acetone and isopropyl alcohol (IPA) under sonication for 20 min, respectively, and treated by O_2 plasma for 60 s. Cleaned substrates were then transferred to a N_2 purged glove box and the filtered PEDOT:PSS (H.C. Starck, Clevios PH 500) was spin-casted onto the ITO electrodes to deposit ~45 nm thick layer which was subsequently baked at 115 °C for 15 min. For the active layer, P3HT (Rieke Metals Inc., 4002-E, ~91 % regioregularity) and PCBM (American Dye Source, Purity: > 99.5 %) were used as received, and blend solutions were prepared by dissolving both components in 1,2-dichlorobenzene with 1:1 ratio by weight. The solution was stirred for ~12 h in the N_2 purged glove box to give homogeneous blend system and filtered using a 0.45 μm filter. The thermal annealed devices were fabricated by spin-casting blend solution onto the PEDOT:PSS layer for 90 s and subsequent annealing at 130 °C for 20 min. After thermal treatment, LiF (1 nm) and Al (80 nm) electrodes were deposited by thermal evaporator at pressure of 8×10^{-7} mbar through the circular-shaped shadow masks with 3.5 mm diameter. As for the solvent annealed devices, spin-casting time was reduced to 30 s to retain certain amount of residual solvent in the blend film and the sample was immediately covered by glass petri dish to slowly evaporate the solvent for 2 h. The ESSENCIAL process was performed by squeezing blend solution between a modified PDMS silicone film that is gas-permeable and solvent-resistant with minimal deformation[31] and a ITO substrate coated with PEDOT:PSS. After separating the silicone

film, the blend film was baked at 130 °C for 1 min before further electrode deposition. The effects of thermal treatment time on the device performances of the ESSENCIAL-treated samples have been consistent from 1 min to 20 min. The thickness of the blend film fabricated by the ESSENCIAL method was controlled by changing the concentration of P3HT:PCBM solution (from 0.2 wt%:0.2 wt% to 4 wt%:4 wt%) and the applied pressure (from 0.1 psi to 20 psi), and the solvent evaporation time was changed from tens of minutes to a few seconds depending on the applied pressure. We did not find any significant differences to the performances of the ESSENCIAL-based devices that have the same thickness but were fabricated by different conditions such as the concentration of solution, applied pressure, or processing time. Every device fabricated in this work has ~240 nm thickness of active layer, which was measure by Dektek profiler. To confirm the effect of PEDOT:PSS layer to the device performances, O_2 plasma treated ITO substrates were also used to substitute the PEDOT:PSS/ITO substrate.

Hole-only devices have a structure: transparent substrate/ITO/PEDOT:PSS /P3HT:PCBM/MoO_3/Al. After following the processes mentioned above, 20 nm MoO_3 was deposited onto the active layer instead of LiF and Al deposition through the shadow mask completed device fabrication. Electron-only devices have a structure: transparent substrate/ITO/Cs_2CO_3 /P3HT:PCBM/LiF/Al. 0.2 wt% Cs_2CO_3, dissolved in 2-ethoxyethanol, was spin-casted on ITO substrate and subsequently baked at 170 °C for 20 min. The remaining procedures such as active layer deposition and cathode deposition were chosen according to different type of processing.

2.2.2 Device performance measurements

Current versus voltage characteristics were measured with HP4156B semiconductor analyzer by illuminating the polymer solar cells with AM 1.5 G simulated sun light using Oriel Solar Simulator at the irradiation intensity of 100 mW cm^{-2}, which was calibrated by power meter (OPHIR, Nova-Oriel) and a reference silicon solar cell. Incident photon to collected charge carrier efficiency (IPCE) spectra for EQE were measured with a 150 W Oriel Solar Simulator light source, an Acton Research Corp. Spectra-Pro 275 monochromator, a chopper wheel, and a Stanford Research 830 Lock-In Amplifier. The photocurrents were measured and normalized against a Hammamatsu Si photodiode reference, and long pass filters were used to block transmission of any stray 2^{nd} or 3^{rd} diffractions outside of the range of interest.

2.2.3 Morphology characterization

The absorption spectra of polymer blend were measured using a Varian Cary 50 UV/Vis spectrophotometer. Photoluminescence spectra were obtained using PTI Quantamaster spectrofluorometer equipped with an integrating sphere. A Digital Instruments NanoScope IIIa-Phase Atomic Force Microscope was used to obtain the AFM images.

2.2.4 Roll-to-roll process for polymer solar cells

The modified PDMS silicone sheet film was rolled around a nitrile rubber-coated nylon fabric belt that is wrapped around two polytetrafluoroethylene (PTFE) rollers. Liquid phase blend solution was continuously coated on the ITO substrate between the

upper and lower rollers and the solvent evaporated through the gas-permeable silicone film while the roller pressure is applied. Web speed (10-20 mm s^{-1}) was controlled by an AC motor controller. Rolling force is measured in real-time by a flexible force sensor (Tekscan, Inc.) and adjusted by a clamping device. The squeezed flow behavior of the solution in the roll-to-roll process follows the dynamic elastic contact model and the thickness of liquid coating is controlled by the solution concentration, the roller pressure and the rolling speed.[30] The blend-film coated ITO substrate separates from the silicone film continuously as the web moves forward. After 1 min heating at 130 °C, thermal deposition of LiF and Al completed devices.

2.3 Results and discussion

The ESSENCIAL process is depicted in Figure 2.1a. P3HT:PCBM blend were used as a model system, and the blend solution was placed on a transparent anode substrate and capped with a gas-permeable silicone film where pressure is applied. The induced shear flow could help align the polymer chains while the solvent evaporates through the silicone film. The solidified blend layer remained on the substrate after removing the silicone film. Interestingly, poly(3,4-ethylenedioxythiophene):poly(styrenesulfonate) (PEDOT:PSS) layer, widely used on top of transparent anode in organic solar cells, was not indispensable to this processing, and will be further explained later with roll-to-roll application. The thickness of the active layer can be controlled by adjusting the solution concentration and the applied pressure, and the evaporation and solidification time can be reduced to a few seconds by controlling the applied pressure. Detailed information on processing conditions is explained in the Experimental section.

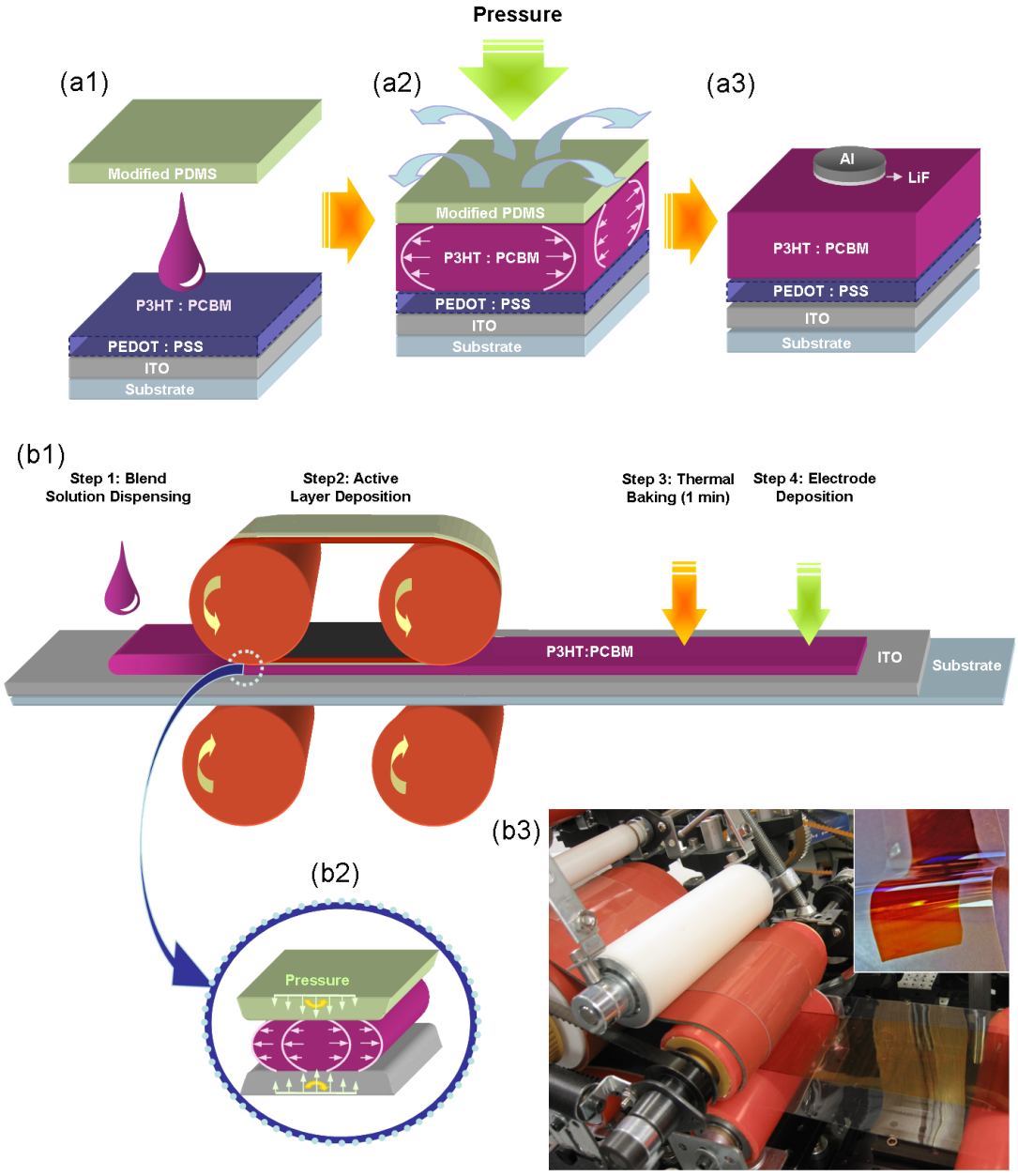

Figure 2.1 (a) Schematic of the ESSENCIAL process for fabricating polymer solar cells: (a1) Applying blend solution; (a2) Active layer formation during solvent evaporation under pressure; (a3) Isolated island-type electrode deposition on top of polymer blend film after removing the PDMS stamp. Note that PEDOT:PSS layer is not indispensable to this processing as described in the text. (b) Roll-to-roll processing for polymer solar cells: (b1) Schematic of roll-to-roll process for polymer solar cell fabrication; (b2) A schematic to depict the squeezed flow behavior of solution during dynamic roll-to-roll process. The thickness of liquid coating is affected by concentration of solution, roller pressure and rolling speed according to the dynamic elastic contact model; (b3) A photograph of the roll-to-roll apparatus and process. The inset image is the resultant flexible polymer solar cell before electrode deposition.

Firstly, the effects of different processing methods on the crystallinity of the conjugate polymer were investigated by absorbance spectroscopy. The chain ordering of the conjugate polymer in a BHJ structure is one of the essentials to achieve improved crystallinity for high efficiency solar cell, because the improved organization of polymer chains facilitates hole transport and the long conjugation length enhances the absorption of light resulting in efficient exciton generation.[18] Thus, the conjugate polymer with high crystallinity such as P3HT is advantageous. The absorption spectrum of the blend film fabricated by ESSENCIAL method was compared with that made by the spin-casting method in Figure 2.2a. To further evaluate the efficiency of the ESSENCIAL method, the samples treated by TA and SAA after spin-casting, which were generally used to improve the crystallinity of the P3HT, were also examined. A shear stress applied to polymer solution, which causes the organization of polymer, across entire depth between two plates is much more effective than that between a plate and air surface (*e.g.* spin-casting), which is continuously decreased from the plate and subsequently zero at air interface.[19] Therefore, as expected, enhanced vibronic peaks in the absorbance spectra as well as significant red-shift, which indicate a higher degree of ordering of P3HT chains,[20] were observed in the ESSENCIAL sample. Additionally this processing could be completed in just a few seconds, but the enhancement found in this sample was much higher than that in samples thermally annealed for 20 min and was even comparable to that of the solvent-assisted annealed sample in which P3HT crystals were slowly grown for 2 h. Such property permits this method to be applied to high speed roll-to-roll process and can produce well-ordered P3HT domains.

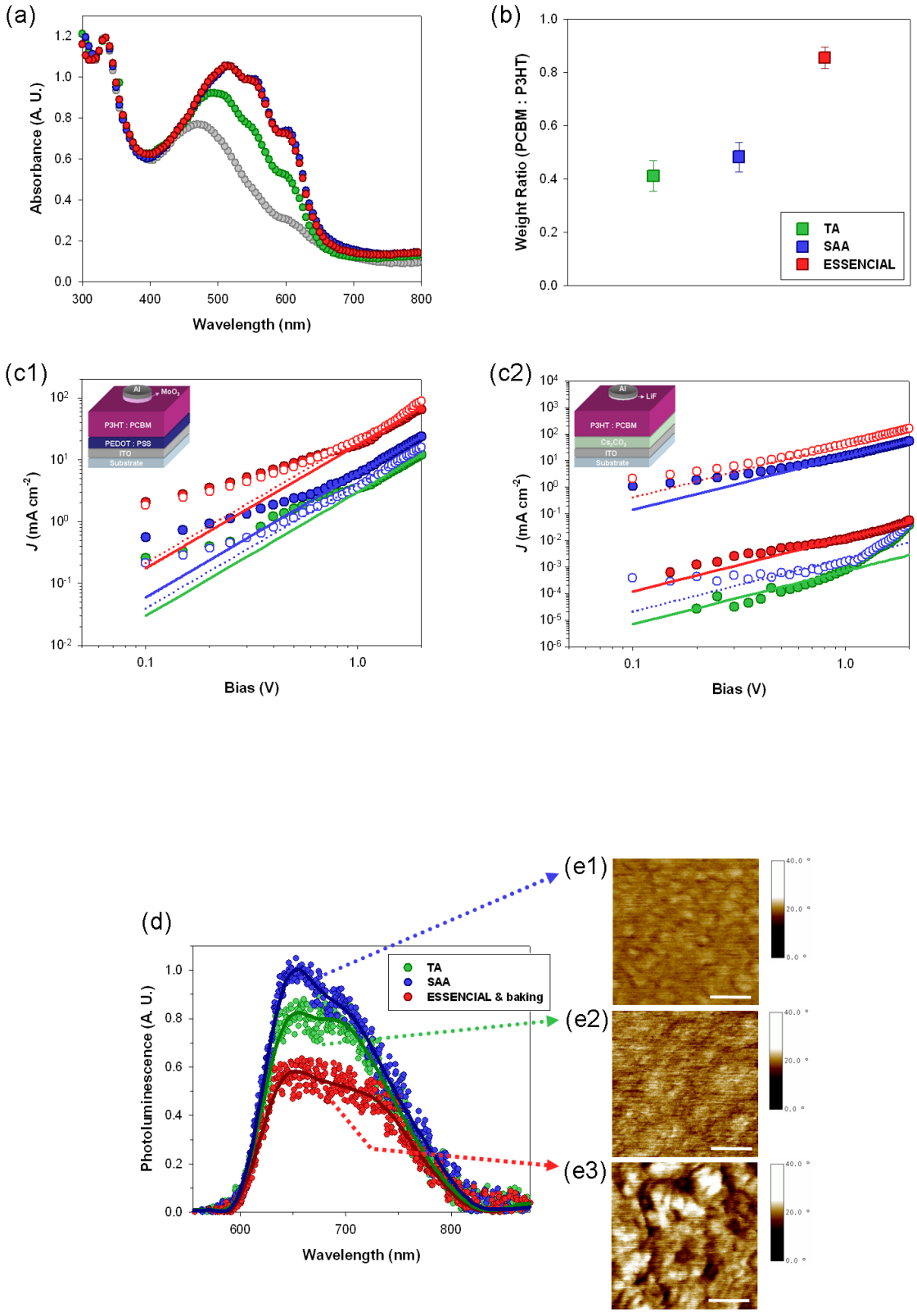
(a)
Absorbance (A. U.)
Wavelength (nm)
(b)
Weight Ratio (PCBM : P3HT)
TA
SAA
ESSENCIAL
(c1)
J (mA cm-2)
Bias (V)
Al
MoO3
P3HT : PCBM
PEDOT : PSS
ITO
Substrate
(c2)
J (mA cm-2)
Bias (V)
Al
LiF
P3HT : PCBM
Cs2CO3
ITO
Substrate
(d)
Photoluminescence (A. U.)
Wavelength (nm)
TA
SAA
ESSENCIAL & baking
(e1)
(e2)
(e3)

Figure 2.2 Characteristics of bulk heterojunction structures obtained by different processing methods. Circle, square, diamond, and triangle represent the blend films made by spin-casting, thermal annealing, solvent-assisted annealing, and ESSENCIAL process, respectively. (a) Absorption spectra of the blend films. The spectra have been normalized to the PCBM peak around 325 nm. (b) Weight ratio of PCBM to P3HT calculated by X-ray photoelectron spectroscopy results for different processing methods. The error bars represent standard deviation. (c) Measured log$J$–log$V$ plots under dark condition for hole- and electron-only devices. Symbols are experimental data and lines are the fit to the experimental data by SCLC model showing linear line with slope = 2 at the log scale. Open symbols and dotted lines represent further thermally annealed results. The applied bias voltage is corrected for the built-in potential due to the difference in work function of the two electrodes. Insets are schematics of the device structures: (c1) hole-only devices; (c2) electron-only devices. (d) Photoluminescence spectra of blend films. ESSENCIAL sample was further treated by heat: filled symbols and lines represent experimental data and their polynomial regressions, respectively. (e) Atomic force microscope phase images. The images in (e1-e3) correspond to solvent-assisted annealed sample, thermal annealed sample and heat-treated ESSENCIAL sample, respectively. The white scale bars represent 50 nm.

In addition to improved polymer crystallinity, the nanodomains of each blend component should be well-connected in order for holes from charge-separated excitons to be effectively transported to anode, and the electrons to cathode through continuous pathways. However, the non-uniform distribution of the donor and acceptor components found in spin-casted sample, even after TA or SAA, is not helpful to the effective charge transport to the electrodes.[12-15] This non-uniform distribution of components in vertical direction is a consequence of the surface energy difference between P3HT (26.9 m N m^{-2}) and PCBM (37.8 m N m^{-2}), which pushes P3HT to the low surface energy air surface to minimize the overall free energy.[13-15] In contrast, much uniform vertical distribution is expected for films prepared by the ESSENCIAL process, because the gas-permeable silicone film effectively provides a higher surface energy than that of air surface. XPS results shown in Figure 2.2b clearly illustrate these trends. Though the weight ratio of PCBM to P3HT in the blend solution is 1:1, the weight ratio of PCBM to P3HT of thermal and solvent-assisted annealed samples measured at the top surface were 0.411 and 0.488, respectively, which indicates a large accumulation of P3HT at the top. But the

ESSENCIAL sample produced much more balanced value (0.855), which implies more uniform distribution of components in the vertical direction. In order to confirm that the uniformly distributed components in ESSENCIAL-treated sample are truly beneficial to effective charge transport by providing more continuous pathways through the film, we constructed hole- and electron-only devices in order to evaluate the charge transport properties in the phase-separated blend film.[21,22] The hole-only device was fabricated by replacing LiF with high work-function molybdenum oxide (MoO_3) to block the injection of electrons from the Al cathode, and electron-only device by using low work function cesium carbonate (Cs_2CO_3) to replace PEDOT:PSS to block the hole injection from the ITO anode.[22] Both hole- and electron-mobility were calculated using space-charge-limited-current (SCLC) model at low voltage (Equation 2.1):[23]

$$J = \frac{9}{8}\varepsilon_o\varepsilon_r\mu\frac{V^2}{L} \qquad \textbf{(Equation 2.1)}$$

where $\varepsilon_o\varepsilon_r$ is permittivity of the component, μ is the carrier mobility, and L is thickness. As shown Figure 2.2c1, the hole-mobility of the thermal annealed sample shows the lowest value ($\mu_h \sim 1.57\times10^{-4}$ cm^2 V^{-1} s^{-1}) due to relatively poor crystallinity of polymers in such samples. In comparison, the hole-mobility of the ESSECIAL-treated sample ($\mu_h \sim 1.15\times10^{-3}$ cm^2 V^{-1} s^{-1}) was much higher, and also higher than solvent-assisted annealed sample ($\mu_h \sim 3.29\times10^{-4}$ cm^2 V^{-1} s^{-1}), even though the two types of samples showed similar polymer crystallinity in the absorbance measurement (Figure 2.2a). This means that the uniformly distributed P3HT polymer domains facilitate the hole transport and the most optimized hole-transporting pathways were obtained in the ESSENCIAL sample across

the entire depth of the device. Meanwhile, it was known that insufficient crystallinity of P3HT in the thermal annealed sample is due to the rapidly grown large PCBM crystal domains,[24] which hampers further crystallization of P3HT. But in solvent-assisted annealed sample, the mild growth of PCBM provides sufficient time for P3HT to be fully crystallized, leading to much balanced crystalline morphologies of the two domains.[25] Therefore, contrary to the rapidly grown large aggregation of PCBM that produces poor electron pathways and significantly lower electron-mobility in the thermal annealed sample, the well-balanced PCBM pathway developed in the solvent-assisted annealed sample showed higher electron-mobility ($\mu_e \sim 4.95\times10^{-4}$ $cm^2\ V^{-1}\ s^{-1}$) as shown Figure 2.2c2. On the other hand, an interesting effect was observed for various samples after further TA: for the ESSENCIAL sample where the electron-mobility was drastically increased to the highest value (from 3.61×10^{-7} to 1.46×10^{-3} $cm^2\ V^{-1}\ s^{-1}$), but the solvent-assisted annealed sample treated by further TA showed reduced electron-mobility similar to that of thermal annealed sample. We believe that PCBM molecules in ESSENCIAL sample, which are not well-organized to form efficient electron pathways before TA, are effectively crystallized; and due to the suppression by the uniformly distributed P3HT polymers they are not overgrown to large aggregates even after thermal treatment. Consequently well-organized PCBM pathways are formed among P3HT polymers to give optimized interpenetrating structures after the thermal treatment. However, in the case of solvent-assisted annealed sample, non-uniformly accumulated PCBM molecules can easily assemble to large PCBM aggregates due to weaker suppression effect by the P3HT during the TA, which inevitably produce poor electron pathways and result in depletion of PCBM in regions within the network structure. Additionally, the effects of further heat

treatment were not significant to the hole-mobilities of the solvent-assisted annealed sample (from 3.29×10^{-4} to 2.20×10^{-4} $cm^2\ V^{-1}\ s^{-1}$) and the ESSENCIAL-treated sample (from 1.15×10^{-3} to 1.26×10^{-3} $cm^2\ V^{-1}\ s^{-1}$) due to sufficiently crystallized P3HTs obtained under both processing conditions (Figure 2.2c1). Consequently, the most optimized transport pathways for both charge carriers were achieved in the heat-treated ESSENCIAL sample, and well-balanced mobilities ($\mu_e/\mu_h \sim 1.16$) was obtained. Even though the electron-mobilities of thermally annealed device and solvent-assisted annealed device with further heat-treatment were not well-matched with SCLC model, the significantly lower expected values ($10^{-8} \sim 10^{-7}$ $cm^2\ V^{-1}\ s^{-1}$) do not affect any conclusions here. The carrier mobilities depending on different processing methods are summarized in Table 1.

Table 2.1 The calculated carrier mobilities depending on the different processing methods.

Method	Carrier mobility [10^{-4} $cm^2\ V^{-1}\ S^{-1}$]		Ratio [μ_e/μ_h]
	Electron [μ_e]	Hole [μ_h]	
TA	-	1.57	-
SAA	4.95	3.29	1.50
ESSENCIAL [a]	14.60	12.60	1.16

[a] ESSENCIAL sample was further treated by heat.

As a last aspect, the domain size in the BHJ structures and their effects on the exciton quenching were investigated using AFM and PL shown in Figure. 2.2d and 2.2e. Compared with the non-uniform mixture where one phase is dominant at one surface, more uniformly mixed donor and acceptor phases throughout the film are expected to have finer interpenetrating nanodomains that are advantageous to efficient dissociation of

photo-generated excitons, and hence result in suppressed PL from the donor polymer. It has been reported that the PL of annealed sample is enhanced as compared with just spin-casted film, because the higher crystallinity induced by annealing gives relatively poor exciton dissociation due to the reduction of interfacial area between the donor and acceptor domains.[26] However, the improved charge transport of the annealed samples due to increased crystallinity can offset the poor exciton dissociation effect, still producing high efficiency solar cells.[27] Therefore, the solvent assisted-annealed sample having higher crystallinity than the thermal annealed sample showed well-defined domains in AFM phase images, and this improved crystallinity induced the enhancement of PL in Figure. 2.2d. As for the heat-treated ESSENCIAL sample, finer interpenetrating networks than the solvent-assisted annealed sample was expected due to the more uniform distribution of the blend, and well-defined nanodomains were much more discernable in AFM phase images. These uniformly distributed and fine interpenetrating nanodomains not only permit good charge pathways, but also facilitate the efficient exciton dissociation therefore suppressing the PL from the donor, and consequently gave the lowest PL in Figure 2.2d.

The device performances including power conversion efficiency (PCE) and *J–V* curves measured under AM 1.5 G simulated sun light (at 100 mW cm^{-2} intensity) were summarized in Figure 2.3. In device fabrication, isolated island-type metallic cathode was used to exclude the overestimation of the photocurrent commonly occurred in devices using cross-bar type electrodes;[16,17] In our former report, PCE could be overestimated as much as by 30 %, and could be even higher depending on electrode design and measurement conditions.[17] The devices fabricated by the ESSENCIAL method followed

by baking showed the highest PCE due to the optimized domain morphologies and charge pathways that resulted in both increased short circuit current and fill factor (Figure 2.3c and 2.3d). The favorable morphology also led to the lowest series resistance (~ 1.2 Ω cm^2) as expected. The improvement of PCE was confirmed by improved external quantum efficiency (EQE) in the range from 350 nm to 650 nm. The detailed measured values are shown in Figure 2.3b.

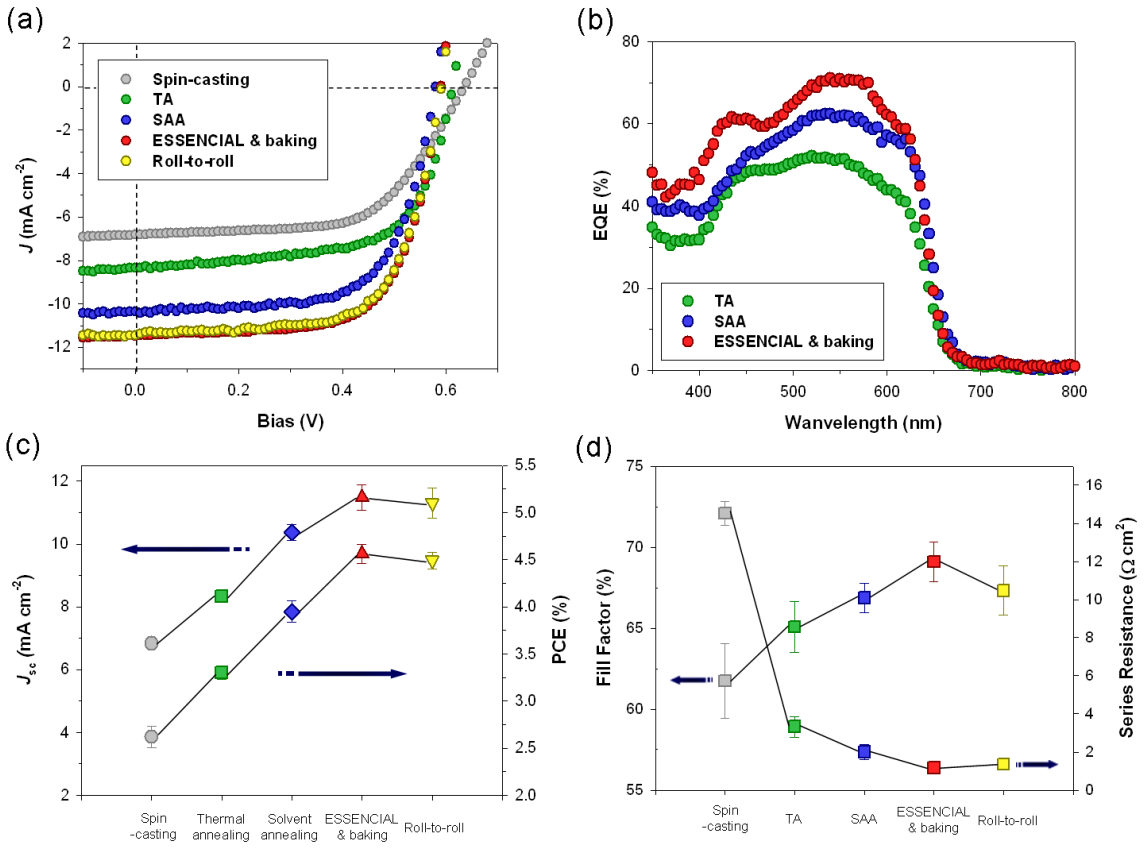

Figure 2.3 Device performances depending on different processing methods. Symbols are as in Figure 2.2 and inverse triangle symbol is added for devices made by roll-to-roll process. All data were measured at AM 1.5 G / 100 mW cm^{-2} (a) *J–V* plots. (b) External quantum efficiency. (c) Power conversion efficiency (PCE) and short circuit current density (J_{sc}). The error bars represent standard deviation. (d) Fill factor (FF) and series resistance (R_s). Average solar cell characteristics

are summarized as follows: spin-casting (J_{sc} = 6.67 mA cm^{-2}, V_{oc} = 0.65 V, FF = 61.7 %, R_s = 14.5 Ω cm^2, PCE = 2.50 %); thermal annealing (J_{sc} = 8.14 mA cm^{-2}, V_{oc} = 0.61 V, FF = 65.1 %, R_s = 3.3 Ω cm^2, PCE = 3.23 %); solvent-assisted annealing (J_{sc} = 10.11 mA cm^{-2}, V_{oc} = 0.58 V, FF = 66.9 %, R_s = 2.0 Ω cm^2, PCE = 3.84 %); heat treated ESSENCIAL (J_{sc} = 10.68 mA cm^{-2}, V_{oc} = 0.60 V, FF = 69.1 %, R_s = 1.2 Ω cm^2, PCE = 4.46 %); roll-to-roll (J_{sc} = 10.59 mA cm^{-2}, V_{oc} = 0.60 V, FF = 67.3 %, R_s = 1.4 Ω cm^2, PCE = 4.40 %). The PV cells fabricated by roll-to-roll processing were prepared without PEDOT:PSS layer.

Before advancing toward the roll-to-roll fabrication, another remarkable merit of the ESSENCIAL-based device is addressed. PEDOT:PSS is the most widely used buffer layer between ITO anode and the active organic semiconductor to improve the performances of polymer solar cells. One of the important roles of this PEDOT:PSS layer is to provide efficient electron blocking[28] to prevent electron leakage from the BHJ acceptors.[29] If PEDOT:PSS is not used, our experiments on the annealed devices after spin-casting showed the significant drop of fill factor (*e.g.* from 65.1 to 54.8 %) that result in much reduction in PCE. However, the ESSENCIAL-based device shows only small drop of fill factor (*e.g.* from 69.1 to 67.3 %) that result in negligible effect to PCE. This effect is consistent to the improved morphology in ESSENCIAL devices discussed above. Because in the devices with spin-casted film, large amount of PCBM are non-uniformly assembled near the ITO anode inducing electron leakage. However, the uniform distribution of components in ESSENCIAL-based devices drastically reduces these electron leakage pathways. Therefore, this observation alone can be an important evidence for the uniform distribution of components in the blend film fabricated by ESSENCIAL. Moreover, avoiding the use of PEDOT:PSS can significantly reduce the processing time as it eliminates the PEDOT:PSS coating and the baking step to remove residual H_2O molecules from PEDOT:PSS used in conventional fabrications, which is especially attractive for high-speed roll-to-roll processing. The advantages of

ESSENCIAL method to induce superior BHJ morphology in short processing time pave the way to scalable high efficiency polymer solar cells fabrication. Here, we demonstrated fabrication of polymer solar cells using a roll-to-roll apparatus composed of dual rollers and tensioned belt covered with gas-permeable silicone film, which enables coating of polymer blend with uniform thickness and fast solvent evaporation in a continuous fashion (Figure 2.1b). According to the dynamic elastic contact model developed for the roll-to-roll nanoimprinting[30] (Figure 2.1b2), the thickness of coated active layer can be controlled by the solution concentration and roller pressure, which is the same condition as the small scale ESSENCIAL experiment discussed earlier, and the film uniformity can be preserved by the belt tension during the solvent evaporation process. Figure 2.1b3 and inset image show 3 inches wide uniform BHJ active layer film made of P3HT:PCBM blend on ITO coated PET substrate for flexible solar cells using the continuous roll-to-roll process. After 1 min baking, LiF and Al cathode were deposited, and a PCE (~ 3.5 %) comparable with the small scale ESSENCIAL experiment was achieved using the roll-to-roll process as shown in Figure 2.3.

2.4 Conclusion

In conclusion, the novel ESSENCIAL-based technique developed in this work shows the most optimum BHJ morphology compared with conventional methods and permits us to realize high efficiency polymer solar cell using high seed roll-to-roll process. More importantly, we believe that this new process is equally applicable to BHJ structures using other materials (*e.g.* the low band gap polymer semiconductors that demonstrated

higher PCE[7]), making it a potential manufacturing technique for mass production of low cost high efficiency polymer solar cells.

2.5 References

1. Morton, O. Solar energy: A new day dawning?: Silicon Valley sunrise. *Nature* **443**, 19–22 (2006).
2. Sariciftci, N. S., Smilowitz, L., Heeger, A. J. & Wudl, F. Photoinduced electron transfer from a conducting polymer to buckminsterfullerene. *Science* **258,** 1474–1476 (1992).
3. Yu, G., Gao, J., Hummelen, J. C., Wudl, F. & Heeger, A. J. Polymer photovoltaic cells: enhanced efficiencies via a network of internal donor-acceptor heterojunctions. *Science* **270**, 1789–1791 (1995).
4. Halls, J. J. M., Walsh, C. A., Greenham, N. C., Marseglia, E. A., Friend, R. H., Moratti, S. C. & Holmes, A. B. Efficient photodiodes from interpenetrating polymer networks. *Nature* **376**, 498–500 (1995).
5. Ma, W., Yang, C., Gong, X., Lee, K. & Heeger, A. J. Thermally stable, efficient polymer solar cells with nanoscale control of the interpenetrating network morphology. *Adv. Funct. Mater.* **16**, 1617–1622 (2005).
6. Li, G., Shrotriya, V., Huang, J., Yao, Y., Moriarty, T., Emery, K. & Yang, Y. High-efficiency solution processable polymer photovoltaic cells by self-organization of polymer blends. *Nature Mater.* **4**, 864–868 (2005).

7. Chen, H.-Y., Hou, J., Zhang, S., Liang, Y., Yang, G., Yang, Y., Yu, L., Wu, Y. & Li, G. Polymer solar cells with enhanced open-circuit voltage and efficiency. *Nature Photon.* **3**, 649–653 (2009).

8. Krebs, F. C., Gevorgyan, S. A. & Alstrup, J. A roll-to-roll process to flexible polymer solar cells: model studies, manufacture and operational stability studies. *J. Mater. Chem.* **19**, 5442–5451 (2009).

9. Krebs, F. C. All solution roll-to-roll processed polymer solar cells free from indium-tin-oxide and vacuum coating steps. *Org. Electron.* **10**, 761–768 (2009).

10. Blankenburg, L., Schultheis, K., Schache, H., Sensfuss, S. & Schrödner, M. Reel-to-reel wet coating as an efficient up-scaling technique for the production of bulk-heterojunction polymer solar cells. *Sol. Energy Mater. Sol. Cells* **93**, 476–483 (2009).

11. Bavel, S. S. v., Sourty, E., With, G. d. & Loos, J. Three-dimensional nanoscale organization of bulk heterojunction polymer solar cells. *Nano Lett.* **9**, 507–513 (2009).

12. Campoy-Quiles, M. Ferenczi, T., Agostinelli, T., Etchegoin, P. G., Kim, Y., Anthopoulos, T. D., Stavrinou, P. N., Bradley, D. D. C. & Nelson, J. Morphology evolution via self-organization and lateral and vertical diffusion in polymer:fullerene solar cell blends. *Nature. Mater.* **7**, 158–164 (2008).

13. Yao, Y., Hou, J., Xu, Z., Li, G. & Yang, Y. Effects of solvent mixtures on the nanoscale phase separation in polymer solar cells. *Adv. Funct. Mater.* **18**, 1783–1789 (2008).

14. Xu, Z., Chen, L.-M., Yang, G., Huang, C.-H., Hou, J., Wu, Y., Li, G., Hsu, C.-S. & Yang, Y. Vertical phase separation in poly(3-hexylthiophene): fullerene derivative

blends and its advantage for inverted structure solar cells. *Adv. Funct. Mater.* **19**, 1227–1234 (2009).

15. Germack, D. S., Chan, C. K., Hamadani, B. H., Richter, L. J., Fischer, D. A., Gundlach, D. J. & DeLongchamp, D. M. Substrate-dependent interface composition and charge transport in films for organic photovoltaics. *Appl. Phys. Lett.* **94**, 233303 (2009).
16. Cravino, A., Schilinsky, P. & Brabec, C. J. Characterization of organic solar cells: the importance of device layout. *Adv. Funct. Mater.* **17**, 3906–3910 (2007).
17. Kim, M.-S., Kang, M.-G., Guo, L. J. & Kim, J. Choice of electrode geometry for accurate measurement of organic photovoltaic cell performance. *Appl. Phys. Lett.* **92**, 133301 (2008).
18. Coakley, K. M. & McGehee, M. D. Conjugated polymer photovoltaic cells. *Chem. Mater.* **16**, 4533–4542 (2004).
19. Kim, S.-S., Na, S.-I., Jo, J., Tae, G. & Kim, D.-Y. Efficient polymer solar cells fabricated by simple brush painting. *Adv. Mater.* **19**, 4410–4415 (2007).
20. Sunderberg, M., Inganas, O., Stafstrom, S., Gustafsson, G. & Sjogren, B. Optical absorption of poly(3-alkylthiophenes) at low temperatures. *Solid State Commun.* **71,** 435–439 (1989).
21. Mihailetchi, V. D., Koster, L. J. A., Blom, P. W. M., Melzer, C., Boer, B. d., Duren, J. K. J. & Janssen, R. A. J. Compositional dependence of the performance of poly(*p*-phenylene vinylene):methanofullerene bulk-heterojunction solar cells. *Adv. Funct. Mater.* **15**, 795–801 (2005).

22. Shrotriya, V., Yao, Y., Li, G. & Yang, Y. Effect of self-organization in polymer/fullerene bulk heterojunctions on solar cell performance. *Appl. Phys. Lett.* **89**, 063505 (2006).

23. Lampert, M. A. & Mark, P. *Current Injection in Solids* (Academic, New York, 1970).

24. Swinnen, A., Haeldermans, I., Ven, M. v., D'Haen, J., Vanhoyland, G., Aresu, S., D'Olieslaeger, M. & Manca, J. Tuning the dimensions of C_{60}-based needlelike crystals in blended thin films. *Adv. Funct. Mater.* **16**, 760–765 (2006).

25. Jo, J., Kim, S.-S., Na, S.-I., Yu, B.-K. & Kim, D.-Y. Time-dependent morphology evolution by annealing processes on polymer:fullerene blend solar cells. *Adv. Funct. Mater.* **19**, 866–874 (2009).

26 Kim, Y., Cook, S., Tuladhar, S. M., Choulis, S. A., Nelson, J, Durrant, J. R., Bradley, D. D. C., Giles, M., Mcculloch, I., Ha, C.-S. & Ree, M. A strong regioregularity effect in self-organizing conjugated polymer films and high-efficiency polythiophene:fullerene solar cells. *Nature Mater.* **5**, 197–203 (2006).

27. Li, G., Shrotriya, V., Yao, Y., Huang, J. & Yang, Y. Manipulating regioregular poly(3-hexylthiophene) : [6,6]-phenyl-C_{61}-butyric acid methyl ester blends—route towards high efficiency polymer solar cells. *J. Mater. Chem.* **17**, 3126–3140 (2007).

28. Koch, N., Elschner, A. & Johnson, R. L. Green polyfluorene-conducting polymer interfaces: Energy level alignment and device performance. *J. Appl. Phys.* **100**, 024512 (2006).

29. Irwin, M. D., Buchholz, D. B., Hains, A. W., Chang, R. P. H. & Marks, T. J. p-Type semiconducting nickel oxide as an efficiency-enhancing anode interfacial layer in polymer bulk-heterojunction solar cells. *PNAS* **105**, 2783–2787 (2008).

30. Ahn, S. H. & Guo, L. J. Large-area roll-to-roll and roll-to-plate nanoimprint lithography: a step toward high-throughput application of continuous nanoimprinting. *ACS Nano* **3**, 2304–2310 (2009).

31. Pina-Hernandez, C., Kim, J.-S., Guo, L. J. & Fu, P.-F. High throughput and etch selective nanoimprinting and stamping based on fast thermal-curable polydimethysiloxanes *Adv. Mater.* **2007**, *19*, 1222.

CHAPTER 3

Additional Improvement of Power Conversion Efficiency from Bulk Heterojunction Polymer Solar Cells: the Effect of C_{60} Buffer Layer in Cathode Interface

3.1 Introduction

As explained in chapter 2, bulk heterojunction (BHJ) polymer solar cell is one of the most promising candidates toward high efficiency polymer solar cells.[1-6] However, the non-uniform vertical distribution in photoactive layer[7-10] induced by the difference of surface energy during spin-casting is opposite to the ideal solar cell structure that requires a electron-donor rich phase near the anode and an acceptor rich phase near the cathode, and therefore unfavorable to charge transport to the electrodes.

In chapter 2, we have shown that much uniform vertical distribution, which is advantageous to photogenerated exciton dissociation and charge transportation, can be achieved by casting the blend solution using ESSENCIAL process, which means evaporation of solvent through surface encapsulation and with induced alignment of polymer chains by applied pressure.[11] However, the vertical distribution of blend components even in ~ 250 nm thickness photoactive layer was not completely uniform (the weight ratio of PCBM to P3HT in ESSENCIAL samples is about 0.9, as shown in Figure 2.2 b).[11] Furthermore, as the thickness of the photoactive layer is increased, which is advantageous to the absorption of the light, the non-uniformity of component become significant. We found that, in thick photoactive layer of BHJ polymer solar cells (over

300 nm), the electron mobility is significantly lower than the hole mobility and the contact resistance at the top cathode, which affects the transportation of photo-generated electron, is too high to efficiently transfer the electrons. Therefore, if we can improve the uniformity of component in vertical direction within thick photoactive layer over 300 nm, which can sufficiently absorb light, we can expect further improvement of the power conversion efficiency (PCE) of BHJ structure.

In this work, we have controlled the vertical distribution of thick BHJ layer over 300 nm, composed of poly(3-hexylthiophene) (P3HT) : [6,6]-phenyl C_{61} butyric acid methyl ester (PCBM) blend, by additional thin C_{60} layer. Our measurement results of space-charge-limited-current (SCLC) model at low voltage[12] and carrier extraction by linearly increasing voltage (CELIV) method[13,14], based on single carrier devices, showed that the electron mobility of BHJ devices was significantly increased to be compatible to hole mobility after adding C_{60} layer. Furthermore, this additional C_{60} layer decreased the contact resistance between the active layer and the top cathode helping efficient electron transportation, ultimately improving the PCE of polymer solar cells.

3.2 Experimental details

3.2.1 Polymer solar cells fabrication & device performance measurements

Polymer solar cells were fabricated by spin-casting method followed by thermal annealing and ESSENCIAL process, as explained in section 2.2.1. The additional C_{60} layer was thermally evaporated at pressure of 8×10^{-7} mbar before depositing LiF and Al cathode. The device performances were measured with Keithley 2400 system by

illuminating the polymer solar cells with AM 1.5 G simulated sun light using Oriel Solar Simulator at the irradiation intensity of 100 mW cm^{-2}, as explained in section 2.2.2.

3.2.2 Photo-CELIV measurement

Our photo-CELIV (Carrier Extraction by Linearly Increasing Voltage) measurements were performed at room temperature. A short N_2 gas laser (337 nm, PTI GL-3300) pulse by 1.5 ns pulse width and 0.2 mJ pulse energy was illuminated on device samples to generate charge carriers within photo-active layers. The generated charge carriers were then extracted by a linearly increasing reverse bias pulse (triangle-shaped voltage pulse). The voltage pulse was created by HP 3314A function generator. The delay time (t_{del}) between the laser flash and the triangular bias pulse was in the range from 1 to 200 μs, which was controlled by SRS DG535 digital delay/pulse generator (Stanford Research Systems). An optical sample stage and two micro manipulators were utilized to set anode/cathode electrical contacts, through which the voltage pulses (widths of t_p= 100 μs by 10 kHz frequency) were assigned. The peak voltage in reverse direction was V_a= 1 V~2 V applied on the Al cathode electrode, with varied offset bias V_{off} in forward direction, which was set to compensate an initial built-in potential. We then monitored the resulting current as a function of time using the 50 Ω input of a digital storage oscilloscope (DSO7054A, Agilent Technologies).

3.3 Results and discussion

Figure 3.1 shows that the device performances of BHJ solar cells composed of P3HT: PCBM blend depending on the thickness of photoactive layer. Although the active layer

thickness is increased, the overall PCEs are not significantly improved and start to decrease in both thermally annealed spin-casted devices and ESSENCIAL devices, even with slightly increased photocurrents. This is mainly due to the decreased fill factor according to the increased thickness, which is usually found in non-favorable morphology of electron-donor and acceptor. The vertical non-uniformity, inducing poor charge transportation and intermixing of components, is one of the important factors inducing these types of inferior morphology. This non-uniform distribution is mostly due to the different surface energy of components in blend during conventional spin-casting process. Therefore the thermal annealed devices based on spin-casting process show much lower overall PCEs as well as the larger decrease of fill factor compared with those fabricated by ESSENCIAL process that induces the relatively uniform vertical distribution.[11] The overall PCEs in thermal annealed devices start to decrease over ~ 300 nm active layer thickness.

ESSENCIAL process, which uses the gas-permeable film providing a higher surface energy than air, is helpful to improve the vertical uniformity by preventing one component having lower surface energy from migrating to the top surface. However, these effects, mostly originated from the change of components at the photoactive layer surface, are expected to become less effective as the thickness of active layer is increased. Therefore, the overall PCE cannot be continuously improved by simply increasing thickness and the PCEs start to slightly decrease over ~ 400 nm active layer thickness.

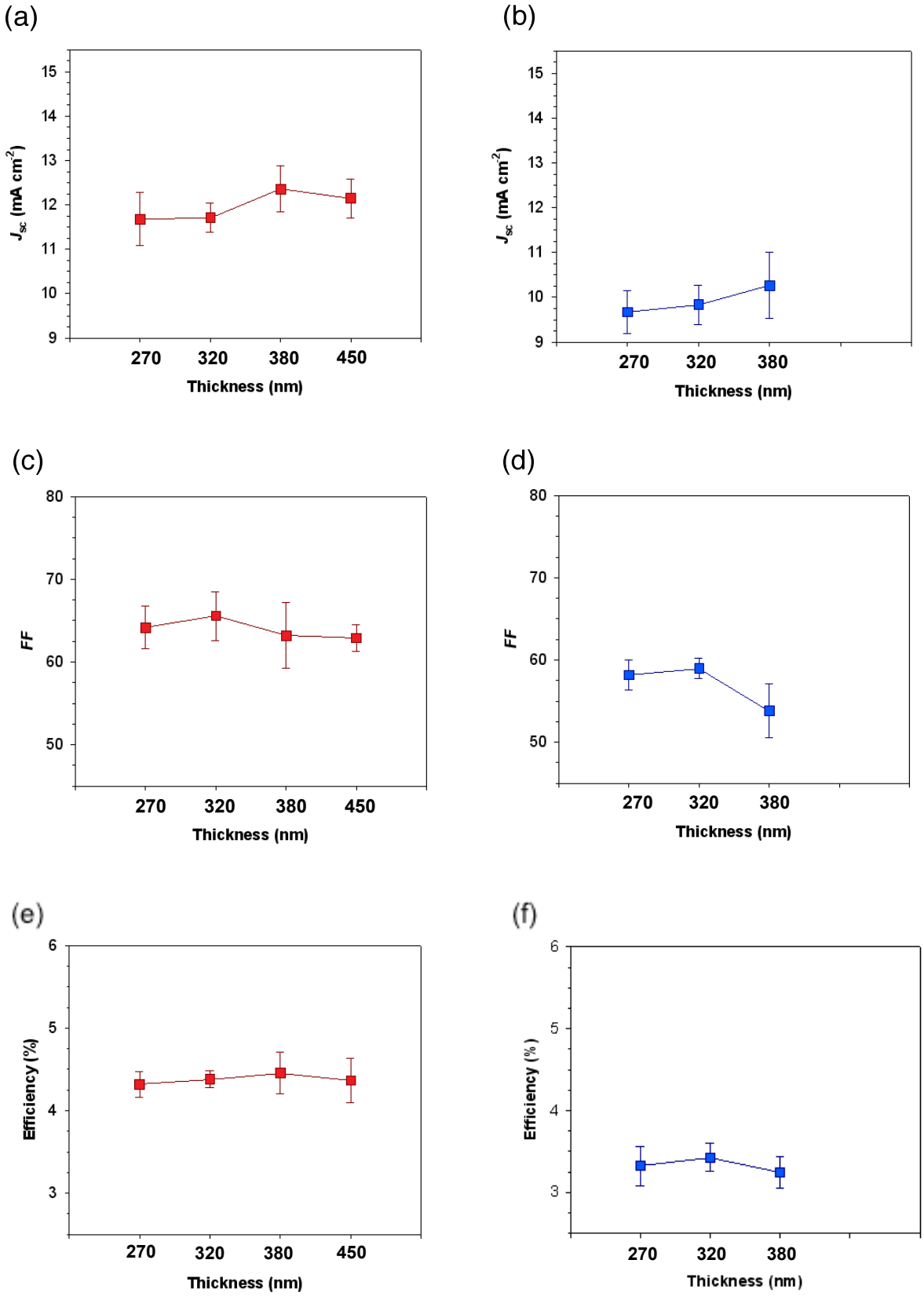
(a)
(b)
(c)
(d)
(e)
(f)
J_{sc} (mA cm^{-2})
FF
Efficiency (%)
Thickness (nm)
270
320
380
450

Figure 3.1 The performance of P3HT:PCBM BHJ solar cells according to the photoactive layer thickness. Short circuit current of (a) ESSENCIAL and (b) thermal annealed devices; Fill factor of (c) ESSENCIAL and (d) thermal annealed devices; Power conversion efficiency of (e) ESSENCIAL and (f) thermal annealed devices.

Meanwhile, it is noteworthy that ESSENCIAL devices show much smaller drop of fill factor around 400 nm thickness compared with thermally annealed devices showing significant drop of fill factor around this thickness. Even in device having the 450 nm thickness photoactive layer, the fill factor of ESSENCIAL devices still remains over 60 %, which means the optimized photoactive layer morphology is not fully destroyed, yet. Therefore, we can presume that the inefficient photocurrent generation in this thicker photoactive layer is due to some other reasons not related with the morphology of photoactive layer, *e.g.* the poor transportation of generated photo-carriers at the interface between the active layer and electrode. In order to check the bottleneck carriers in this device, we have constructed single carrier devices to measure the mobility. The hole-only device was fabricated by replacing LiF with high work-function molybdenum oxide (MoO_3) to block the injection of electrons from the Al cathode, and electron-only device by using low work function cesium carbonate (Cs_2CO_3) to replace PEDOT:PSS to block the hole injection from the ITO anode.[15] Both hole- and electron-mobility were firstly calculated using SCLC model at low voltage (Equation 2.1).[12] As shown in Table 3.1, electron mobility in ESSENCIAL devices is about a half of hole mobility and that in thermal annealed device is about a third of hole mobility, which means electron transportation is not efficient in these devices.

Table 3.1 The calculated carrier mobilities by SCLC model depending on the different processing methods.

Method	Carrier mobility [10^{-4} cm^2 V^{-1} S^{-1}]	
	Hole [μ_e]	Electron [μ_h]
[a]ESSENCIAL	11.5	5.25
Thermal	3.27	1.23

In order to improve the electron transportation, we inserted thin (~ 5 nm) C_{60} acceptor layer, which can help to relive vertical non-uniformity and may help to extract electron at the cathode side. The changes of carrier mobilities with additional C_{60} layer were further verified by photo-CELIV method. The photo-CELIV is a powerful tool permitting us to calculate the mobility of carrier and recombination in low conductivity materials. When the reverse bias is applied with the rise speed A (V s^{-1}) to give triangular-shape voltage pulse in low conductivity materials such as organic solar cells, the rectangular-shape current transient having constant value $j(0)$ (C s^{-1}), which means capacitive displacement current, is measured as a electrical signal. In this condition, when the laser signal is exposed to the devices, the photo-charges are generated in the photoactive layer, and they are either recombined or extracted by the electric field. By measuring t_{max}, which show the maximun photocurrent, and comparing the ratio of extracted current (Δj) to constant current ($j(0)$), we can calculate the mobility value using Equation 3.1.

$$\mu = \frac{2d^2}{3At_{max}^2\left[1+0.36\frac{\Delta j}{j(0)}\right]} \qquad \text{if } \Delta j \le j(0) \qquad \textbf{(Equation 3.1)}$$

where *d* is the thickness of photoactive layer. All the carrier mobility results with and without C_{60} layer, characterized by SCLC and photo-CELIV, are summarized in Table 3.2. In both thermally annealed and ESSENCIAL devices, hole mobilities are almost similar even after adding additional C_{60} layer. However, the electron mobility was drastically increased after adding C_{60} layer, resulting in better charge balance between hole and electron. The detailed photo-CELIV transients are shown in Figure 3.2. Because the measured photo-CELIV signal in hole-only device did not efficiently show capacitive displacement current and the measured Δj is larger than $j(0)$, which deviate from the precondition of Equation 3.1, the values themselves are not reliable. However, the trends of hole mobility changes, not altered after adding C_{60}, is reliable and the deviations from real values do not affect any conclusion is this work. The overall mobility of holes and electrons is higher in ESSENCIAL device, having much more uniform vertical distribution, than those in thermal annealed devices, indicating that vertical uniformity affect the transportation of both charge carriers.

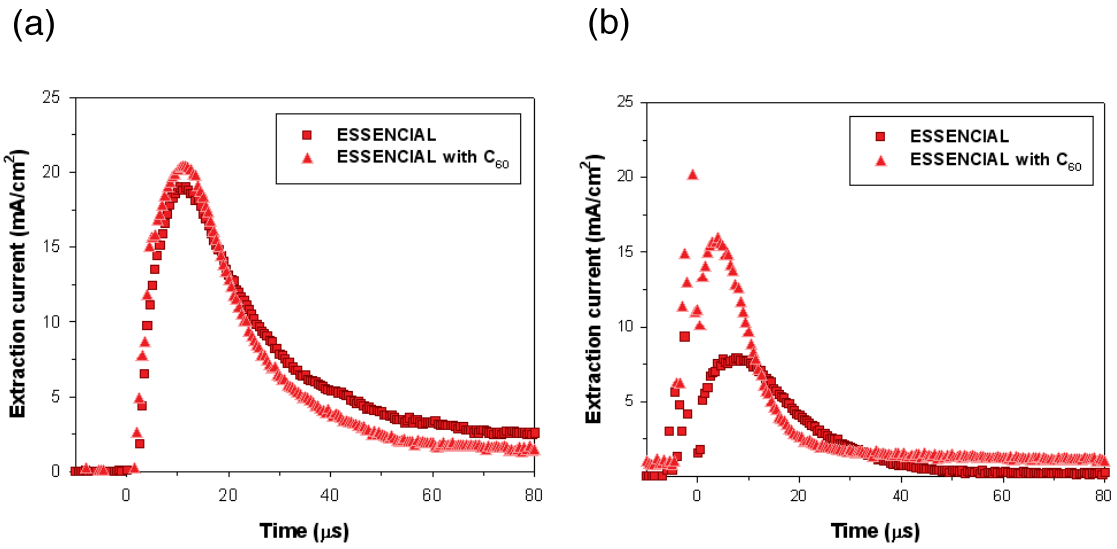

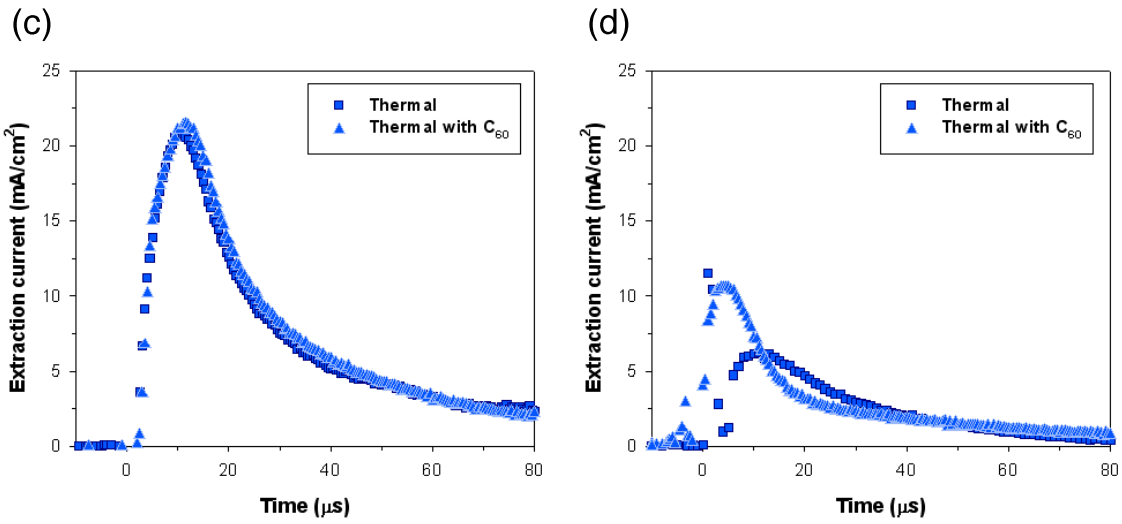

Figure 3.2 Photo-CELIV transient of single carrier devices with C_{60} layer (triangle) and without C_{60} layer (square): (a) Hole-only devices by ESSENCIAL; (b) Electron-only devices by ESSENCIAL; (c) Hole-only devices by thermal annealing; (d) Electron-only devices by thermal annealing.

Table 3.2 The calculated carrier mobilities by SCLC model and photo-CELIV depending on the different processing methods. The values in brackets may be deviated from real values.

Method		Carrier mobility [10^{-4} cm^2 V^{-1} S^{-1}]			
		Hole [μ_e]		Electron [μ_h]	
		No C_{60}	With C_{60}	No C_{60}	With C_{60}
ESSENCIAL	SCLC	11.5	10.90	5.25	13.60
	CELIV	(4.66)	(3.56)	0.90	2.10
Thermal	SCLC	3.27	3.35	1.23	5.84
	CELIV	(2.22)	(1.95)	0.27	1.32

The effect of additional C_{60} layer on charge transportation was also evaluated by measuring the contact resistance between photoactive layer and electrode. By measuring

the resistance between electrodes depending on the distance of the electrodes, we can calculate the contact resistances (Equation 3.2). The measured resistance is composed of contact resistances, series resistance and sheet resistance as shown in Figure 3.3a.

$$\frac{V}{I} = R = 2R_c + 2R_s + R_o \frac{L}{W} \qquad \textbf{(Equation 3.2)}$$

where V is bias, I is current, R is the total resistance, R_c is contact resistance, R_s is series resistance, and R_o is sheet resistance. L and W are the distance between Al electrodes and the width of Al electrode, respectively.

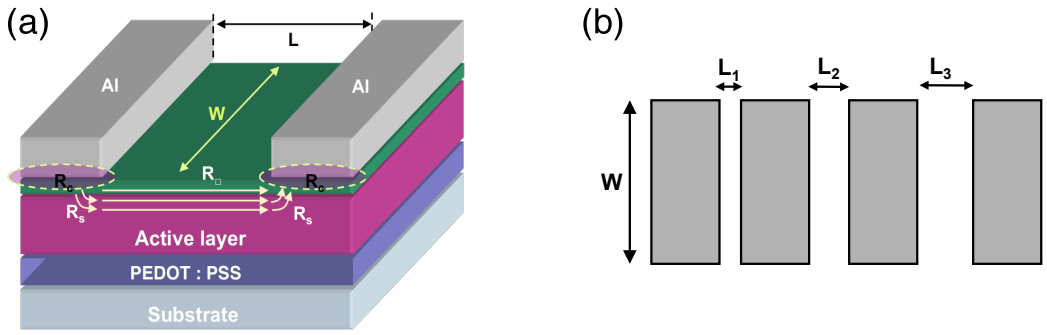

Figure 3.3 (a) The device architecture for contact resistance measurement. (b) Dimensional parameters of electrodes for contact resistance measurement. L and W are the distance between Al electrodes and the width of Al electrode, respectively.

Therefore, after fixing the width of electrode, we can plot the resistance according to the distance of electrode. The slope of this plot represents the sheet resistance and the intercept at the y-axis is the contact resistance. The calculated contact resistances in both ESSENCIAL and thermal annealed devices with and without C_{60} layer are summarized in

Table 3.3. In both cases, the contact resistances were significantly reduced after introducing additional C_{60} layer, which suggest efficient charge carrier transportation through the interface (Figure 3.4a-d). Another interesting feature in these experiments is that the contact resistances calculated in ESSENCIAL devices are much smaller than those in thermally annealed devices. In order to find out the reason, we have measured the contact resistance of PCBM single layer and P3HT single layer with LiF/Al electrode. As shown in Figure 3.4e and f, the resistances of PCBM and electrode contact showed the similar scale values (kilo ohm) with those in ESSENCIAL devices and they were much smaller than those of P3HT and electrode contact (mega ohm scale), which shows the similar scale with those in thermal annealed devices. Therefore, we can conclude that larger quantity of P3HT domains assembled in at the top surface of the thermally annealed photoactive layer induce poor electron transportation to cathode resulting in lower PCE. In contrast, enough amount of PCBM at the surface of ESSENCIAL devices forms good contact between the photoactive layer and electrode, giving efficient electron transportation to electrode. Moreover, the additional C_{60} layer can facilitate the transportation of electron at the interface in both types of devices.

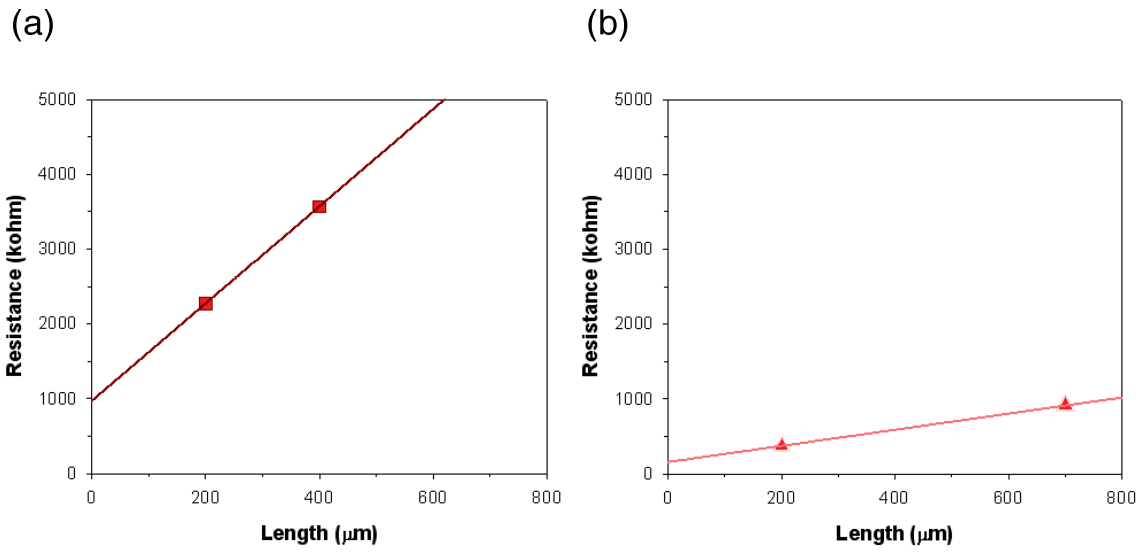

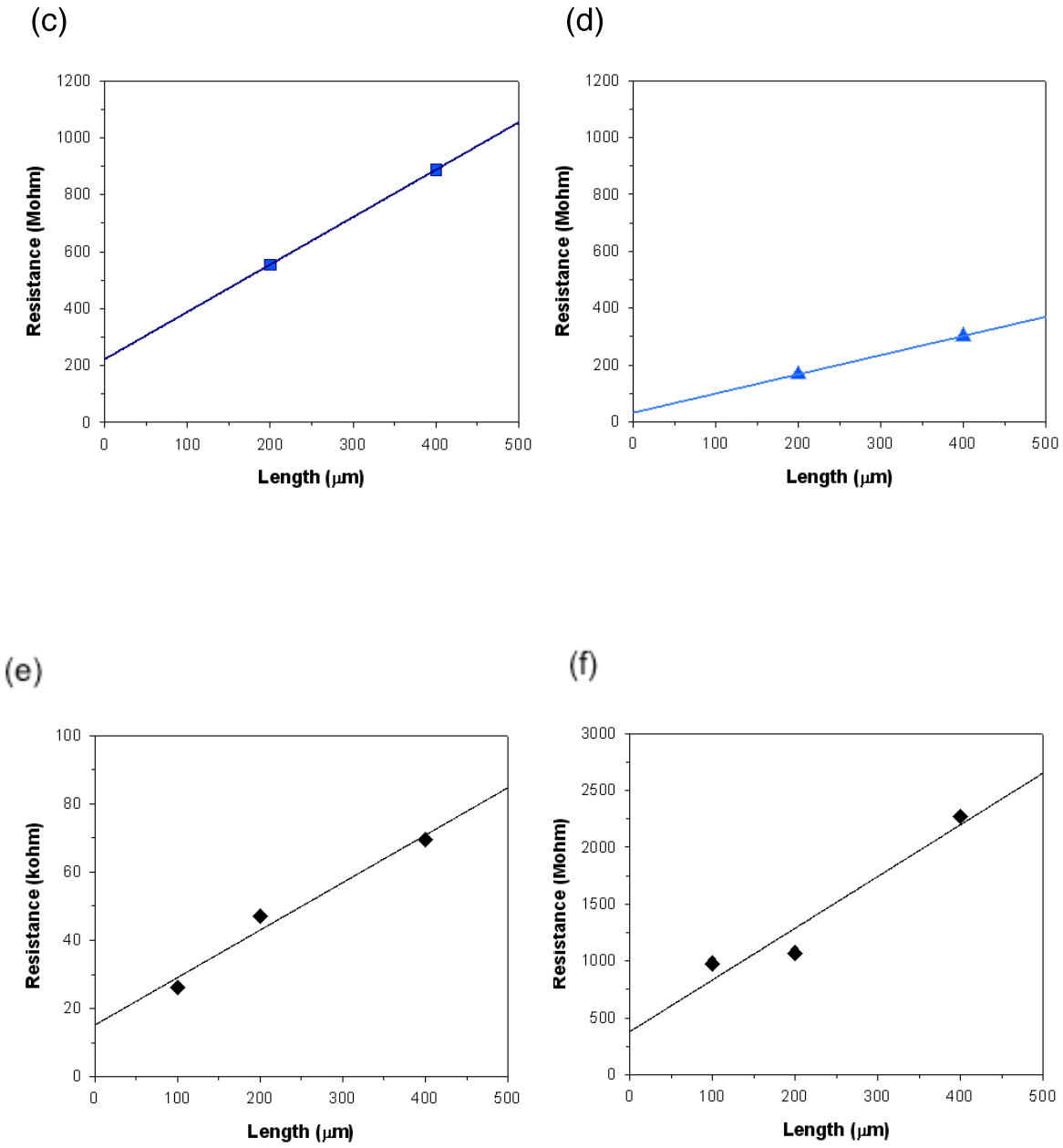

Figure 3.4 The measured resistances according to the distance between LiF/Al electrodes. The intercepts in y-axis mean the contact resistances, R_c: (a) ESSENCIAL without C_{60}; (b) ESSENCIAL with C_{60}; (c) thermal annealed devices without C_{60}; (d) thermal annealed device with C_{60}; (e) PCBM single layer; (f) P3HT single layer.

Table 3.3 Summary of the calculated contact resistances.

Method	Contact resistance	
	Without C_{60}	With C_{60}
ESSENCIAL	1000 kΩ	150 kΩ
Thermal	220 MΩ	30 MΩ
PCBM single layer	15 kΩ	
P3HT single layer	380 MΩ	

The device performances are summarized in Figure 3.5. After adding additional thin C_{60}, device performances were significantly improved. 380 nm and 320 nm active layer thickness are optimized photoactive layer thickness values in ESSENCIAL and thermal annealed devices, respectively. In the case of ESSENCIAL devices, we could achieved around 5.50 % PCE, which is one of the highest value obtained from P3HT:PCBM system.

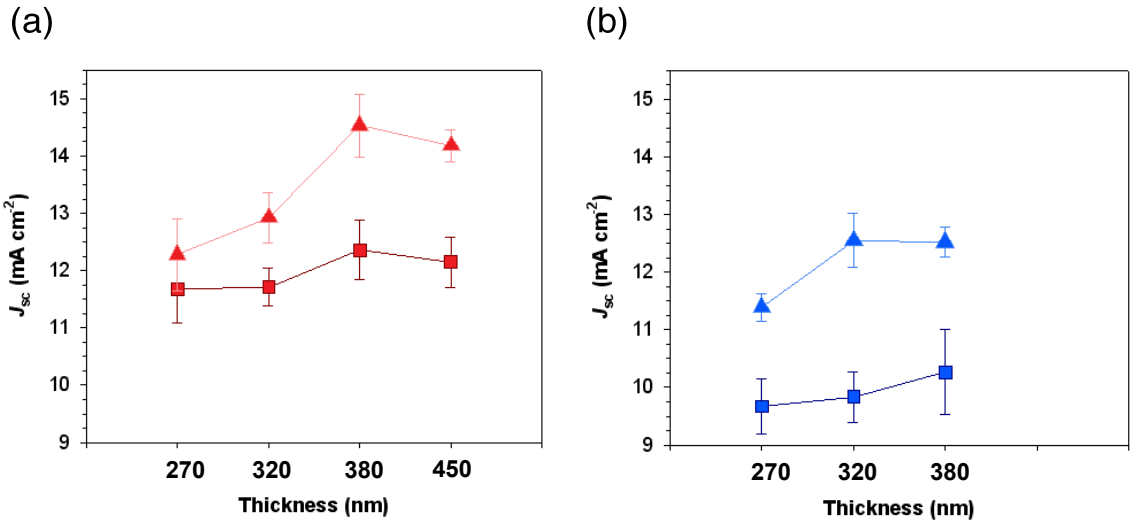

(c)

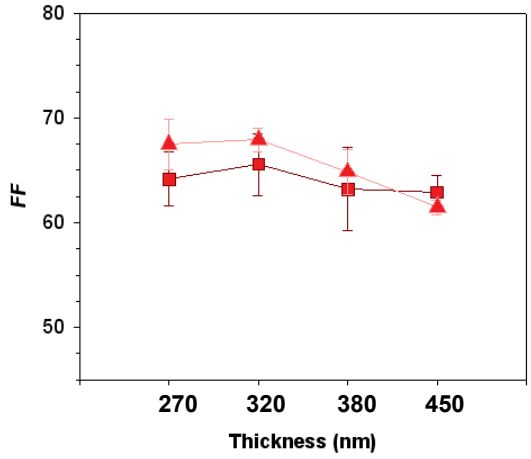
80
70
60
50
FF
270
320
380
450
Thickness (nm)

(d)

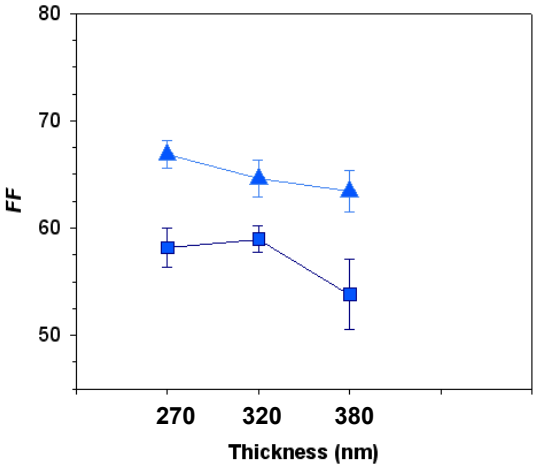
80
70
60
50
FF
270
320
380
Thickness (nm)

(e)

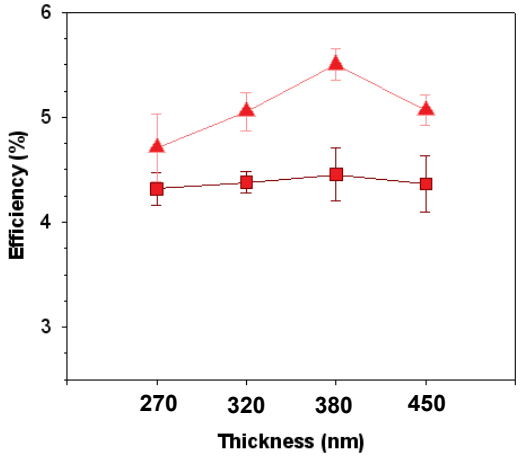
6
5
4
3
Efficiency (%)
270
320
380
450
Thickness (nm)

(f)

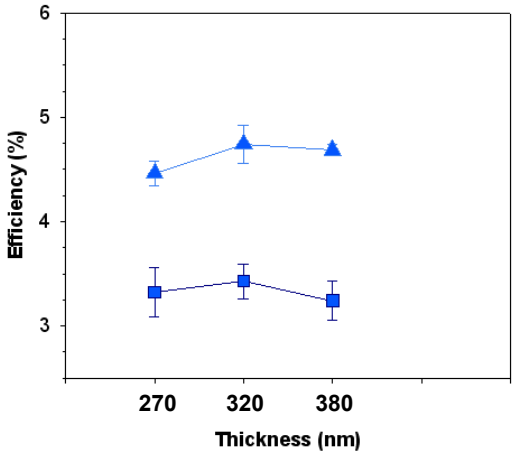
6
5
4
3
Efficiency (%)
270
320
380
Thickness (nm)

(g)

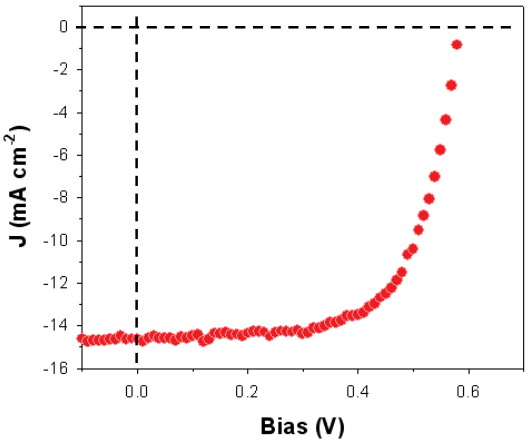
0
-2
-4
-6
-8
-10
-12
-14
-16
J (mA cm-2)
0.0
0.2
0.4
0.6
Bias (V)

(h)

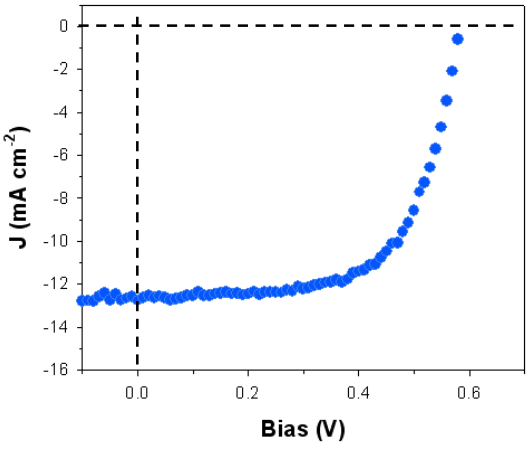
0
-2
-4
-6
-8
-10
-12
-14
-16
J (mA cm-2)
0.0
0.2
0.4
0.6
Bias (V)

Figure 3.5 The performance of P3HT:PCBM BHJ solar cells according to the photoactive layer thickness without C_{60} (square) and with C_{60} (triangle): Short circuit current of (a) ESSENCIAL and (b) thermal annealed devices, fill factor of (c) ESSENCIAL and (d) thermal annealed devices, and power conversion efficiency of (e) ESSENCIAL and (f) thermal annealed devices; *J-V* curves of solar cells showing the best performances in (g) ESSENCIAL (J_{sc} = 14.53 mA cm^{-2}, V_{oc} = 0.58 V, FF = 64.8 %, PCE = 5.50 %) and (h) thermal annealed device (J_{sc} = 12.55 mA cm^{-2}, V_{oc} = 0.58 V, FF = 64.6 %, PCE = 4.74 %).

3.4 Conclusion

In this work, we have shown that the additional C_{60} layer can balance the electron and hole mobility in thick photoactive layer over 300 nm, which showed imbalanced mobility values without C_{60} layer. Furthermore, C_{60} layer reduced the contact resistances between the photoactive layer and top Al cathode giving better transportation of electrons, ultimately improving PCE of polymer solar cells. The optimized solar cells having about 5.50 % PCE were demonstrated based on P3HT:PCBM system.

3.5 References

1. Sariciftci, N. S., Smilowitz, L., Heeger, A. J. & Wudl, F. Photoinduced electron transfer from a conducting polymer to buckminsterfullerene. *Science* **258,** 1474–1476 (1992).
2. Yu, G., Gao, J., Hummelen, J. C., Wudl, F. & Heeger, A. J. Polymer photovoltaic cells: enhanced efficiencies via a network of internal donor-acceptor heterojunctions. *Science* **270**, 1789–1791 (1995).
3. Halls, J. J. M., Walsh, C. A., Greenham, N. C., Marseglia, E. A., Friend, R. H., Moratti, S. C. & Holmes, A. B. Efficient photodiodes from interpenetrating polymer networks. *Nature* **376**, 498–500 (1995).

4. Ma, W., Yang, C., Gong, X., Lee, K. & Heeger, A. J. Thermally stable, efficient polymer solar cells with nanoscale control of the interpenetrating network morphology. *Adv. Funct. Mater.* **16**, 1617–1622 (2005).

5. Li, G., Shrotriya, V., Huang, J., Yao, Y., Moriarty, T., Emery, K. & Yang, Y. High-efficiency solution processable polymer photovoltaic cells by self-organization of polymer blends. *Nature Mater.* **4**, 864–868 (2005).

6. Chen, H.-Y., Hou, J., Zhang, S., Liang, Y., Yang, G., Yang, Y., Yu, L., Wu, Y. & Li, G. Polymer solar cells with enhanced open-circuit voltage and efficiency. *Nature Photon.* **3**, 649–653 (2009).

7. Campoy-Quiles, M. Ferenczi, T., Agostinelli, T., Etchegoin, P. G., Kim, Y., Anthopoulos, T. D., Stavrinou, P. N., Bradley, D. D. C. & Nelson, J. Morphology evolution via self-organization and lateral and vertical diffusion in polymer:fullerene solar cell blends. *Nature. Mater.* **7**, 158–164 (2008).

8. Yao, Y., Hou, J., Xu, Z., Li, G. & Yang, Y. Effects of solvent mixtures on the nanoscale phase separation in polymer solar cells. *Adv. Funct. Mater.* **18**, 1783–1789 (2008).

9. Xu, Z., Chen, L.-M., Yang, G., Huang, C.-H., Hou, J., Wu, Y., Li, G., Hsu, C.-S. & Yang, Y. Vertical phase separation in poly(3-hexylthiophene): fullerene derivative blends and its advantage for inverted structure solar cells. *Adv. Funct. Mater.* **19**, 1227–1234 (2009).

10. Germack, D. S., Chan, C. K., Hamadani, B. H., Richter, L. J., Fischer, D. A., Gundlach, D. J. & DeLongchamp, D. M. Substrate-dependent interface composition

and charge transport in films for organic photovoltaics. *Appl. Phys. Lett.* **94**, 233303 (2009).

11. Park, H. J., Kang, M.-G., Ahn, S. H. & Guo, L. J. Facile route to polymer solar cells with optimum morphology readily applicable to roll-to-roll process without sacrificing high device performances. *Adv. Mater.* **22**, E247–E253 (2010).
12. Lampert, M. A. & Mark, P. *Current Injection in Solids* (Academic, New York, 1970).
13. Juška, G., Arlauskas, K., Viliunas, M. Extraction Current Transients: New method of study of charge transport on microcrystalline silicon. *Phys. Rev. Lett.* **84**, 4946-4949 (2000).
14. Mozer, A. J., Dennler, G., Sariciftci, N. S., Westerling, M., Pivrikas, A., Österbacka, R. & Juška, G. Time-dependent mobility and recombination of the photoinduced charge carriers in conjugated polymer/fullerene bulk heterojunction solar cells. *Phys. Rev. B* **72**, 035217 (2005).
15. Shrotriya, V., Yao, Y., Li, G. & Yang, Y. Effect of self-organization in polymer/fullerene bulk heterojunctions on solar cell performance. *Appl. Phys. Lett.* **89**, 063505 (2006).

CHAPTER 4

Ultrahigh Current Generation in Optimized Photoactive Layer of Polymer Solar Cells Having Internal Quantum Efficiency Approaching 100 %

4.1 Introduction

Polymer solar cell is a promising solar cell technology due to the strong potential for the production of low-cost, easily processible, and flexible solar cells over a large area with acceptable efficiencies.[1-9] Among various photoactive layer structures, bulk heterojunction (BHJ) structure has been exploited as one of the most successful structures giving the highest efficiencies for polymer solar cells, because interpenetrating nanoscale networks of electron-donor and electron-acceptor give domain sizes on the order of exciton diffusion length.[2-6] Therefore, significant efforts have been focused on the ways to optimize and understand the BHJ structures. However, the random nature of such interpenetrating network, which is based on the simple blending of two components, make it difficult to further optimize the structures and limit thorough understandings of their compositions and fundamental physical properties.

To construct an efficient photoactive layer of organic solar cells (OSCs), the absorption of light should be high enough to maximize the photo-generated excitons and the dissociation of those excitons should be efficient simultaneously. Furthermore, those dissociated charge carriers have to be efficiently transported to each electrode without recombination. Even though most of organic semiconductor materials have relatively

high absorption coefficients (> 10^5 cm^{-1}), hundreds of nanometers scale film thickness is still needed to fully absorb the light and minimize the optical interference effect.[10-12] However, as the thickness of photoactive layer in BHJ structures is increased, low carrier mobility in organic semiconductor and inefficient intermixing between donor and acceptor phases inevitably induce poor charge transportation with high recombination, which result in low internal quantum efficiency (IQE) and low fill factor giving low power conversion efficiency (PCE). Therefore another type of architecture is needed to construct better photoactive layer compared with BHJ based on simple mixing of the components.

In this work, we introduce a superior bilayer-based heterojunction structures compared with conventional BHJ structures, which can be fabricated by a novel processing techniques. The bilayer structure of electron-donor and electron-acceptor is a simple structure that can help easy optimization of devices and better understanding about their properties. However, it has been well known as inefficient architecture for OSC, because it cannot efficiently produce photo-carriers due to the limited interfacial areas between domains responsible for charge separation. Therefore their device performances were not compatible to BHJ-based solar cells. Even though several works have been recently reported that this type of structure can mimic the BHJ structure by increasing the intermixing of donor and acceptor layer using solution casting, they just could utilize tens of nanometers scale thin donor layer to fully diffuse the acceptor, giving inefficient absorption of light. So, their OSC performances are limited to those of conventional BHJ-based devices.[13-14]

In contrast, here, we could demonstrate the optimized morphology between donor and

acceptor having IQE approaching almost 100 % even over 300 nm thick photoactive layer, advantageous to enough light absorption, by using bilayer-based structure, which cannot be achieved in conventional BHJ structure. The key concept of this structure is that thick enough donor layer over 300 nm having well-organized nanostructure forms the efficient bicontinuous phase with acceptor inducing the maximized charge transportation and the minimized bimolecular recombination which is limiting factors of conventional BHJ structures in thick photoactive layer. For the practical application, we have demonstrated this type of structure using poly(3-hexylthiophene) (P3HT) and [6,6]-phenyl-C_{61}-butyric acid methylester (PCBM), which are most widely used commercially available materials as a model system.

Our process significantly facilitates interdiffusion between the donor and acceptor layers inducing optimized morphology favorable for charge generation and transportation that cannot be achieved by the conventional BHJ structure. The P3HT/PCBM bilayer system OSCs produced by our new process showed longer bimolecular life-time of photo-charges and higher internal quantum efficiency (IQE), approaching almost 100%, which indicate that nanostructures in photoactive layer are well-optimized. Therefore resultant short circuit current of these devices was over 50 % higher than those of the thermally annealed BHJ polymer solar cells. Structures fabricated by different methods were further compared by the measurements of external quantum efficiency (EQE), absorbance spectra, dynamic secondary ion mass spectroscopy (DSIMS), and carrier extraction by linearly increasing voltage (CELIV) method. Their morphologies were also studied using grazing incidence wide angle x-ray scattering (GIWAXS) and atomic force microscopy (AFM). This structure and the new process not only suggest an alternative

and practical way toward high efficiency polymer solar cells, we believe it also help us understand the underlying fundamentals of the OSC operations.

4.2 Experimental Details

Polymer solar cells were fabricated by spin-casting method followed by thermal annealing and ESSENCIAL process, as explained in section 2.2.1. The device performances were measured with Keithley 2400 system by illuminating the polymer solar cells with AM 1.5 G simulated sun light using Oriel Solar Simulator at the irradiation intensity of 100 mW cm^{-2}, as explained in section 2.2.2. The photo-CELIV measurement set-up and experimental parameters are explained in 3.2.2.

4.3 Results and discussion

Overall processing is composed of two steps, as depicted in Figure 4.1. Recently, we have demonstrated that BHJ blends can be optimized to have uniform distribution when it is casted using gas-permeable cover layer, so called ESSENCIAL process, which means evaporation of solvent through surface encapsulation and induced alignment of polymer chains by applied pressure. In this work, P3HT layer as electron-donor was firstly formed using the ESSENCIAL process. The solution was placed on a transparent anode substrate, coated by hole transporting layer poly(3,4-ethylenedioxythiophene): poly(styrenesulfonate) (PEDOT:PSS), and capped with a gas-permeable silicone film, to which pressure was applied. The induced shear flow help the alignment of the polymer chains while the solvent evaporated through the silicone film. The solidified P3HT layer remained on the substrate after removal of the silicone film. A shear stress applied to the

polymer solution—which help the organization of the polymer—across the entire depth between two plates is much more effective than that between a plate and an air surface (as, for example, in spin-casting), which decreases continuously from the plate to be zero at the air interface.[15] Therefore, the organization of P3HT nanodomains formed by ESSENCIAL process is much more efficient than that formed by spin-casting, and even better than thermally annealed film. Even though the spin-casted P3HT film also have high enough crystallinity compared with that in BHJ structures blended with PCBM, which prevents the P3HT polymer chains from being crystallized, the organization of P3HT polymer chains formed by ESSENCIAL process is much more efficient than that formed by spin-casting.

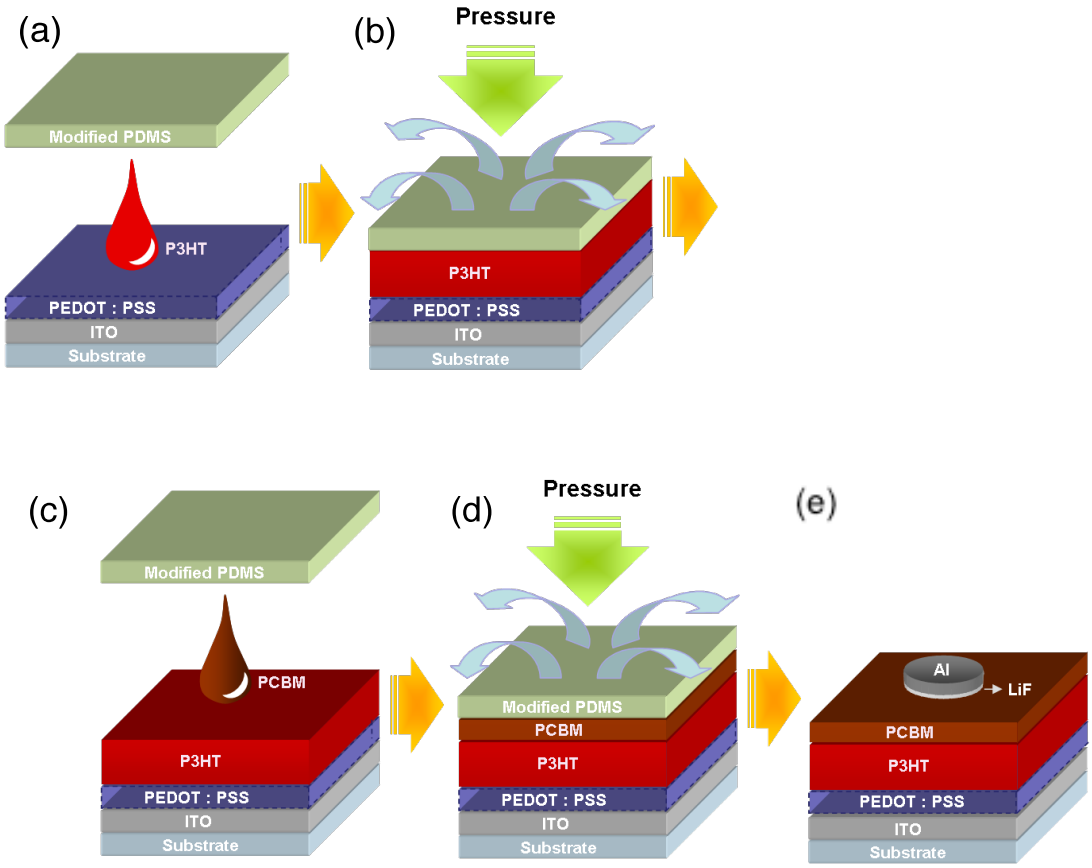

Figure 4.1 Schematic of the 2-step ESSENCIAL process for bilayer-based polymer solar cells: (a) Applying P3HT solution in chlorobenzene; (b) P3HT layer formation during solvent evaporation under pressure; (c) Applying PCBM solution in dichloromethane; (d) Active layer formation during solvent evaporation under pressure; (e) Isolated island-type electrode deposition on top of photoactive layer after removing the PDMS stamp.

The well-organized P3HT nanodomains were analyzed by various experimental methods, shown in Figure 4.2. SEM images in Figure 4.2a and 2b clearly show that tens of nanometer scale continuous nanowires, which is advantageous to charge transportation, are formed in ESSENCIAL sample. These features are also shown in AFM topological and phase images (Figure 4.2c, 2d, 2e and 2f). The ordering of P3HT polymer chains was further investigated by GIWAXS. In this experiment, the samples were measured at 0.3^{o} over the critical angle to analyze the organization of polymer chains in the bulk. As shown in two-dimensional GIWAXS patterns (Figure 4.2g and 2h), the strong (h00) signals, which are designated by first order (100), second order (200) and third order (300) reflections, are detected in the out-of-plane scattering and (010) signal are shown in in-plane scattering, which means that most of P3HT polymer chains have the edge-on morphology. P3HT casted by ESSENCIAL process shows stronger intensity of both (h00) and (010) signals, which means better organization of P3HT crystal nanodomains.

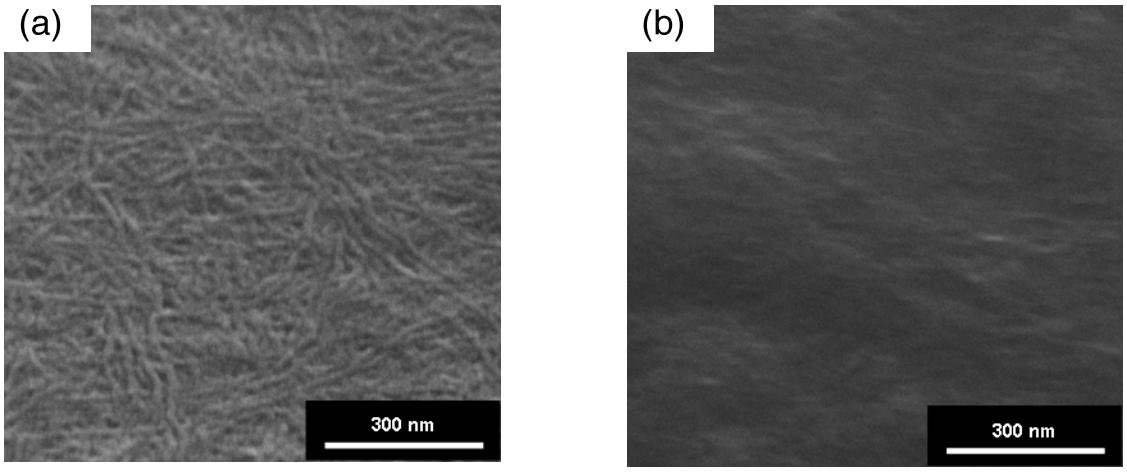

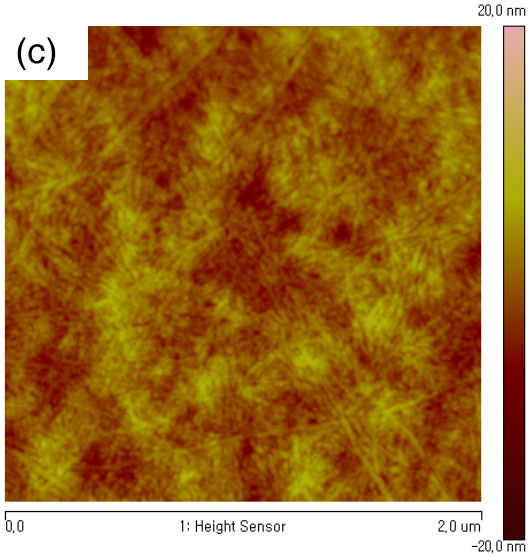
(c)
20,0 nm
0,0
1: Height Sensor
2,0 um
-20,0 nm

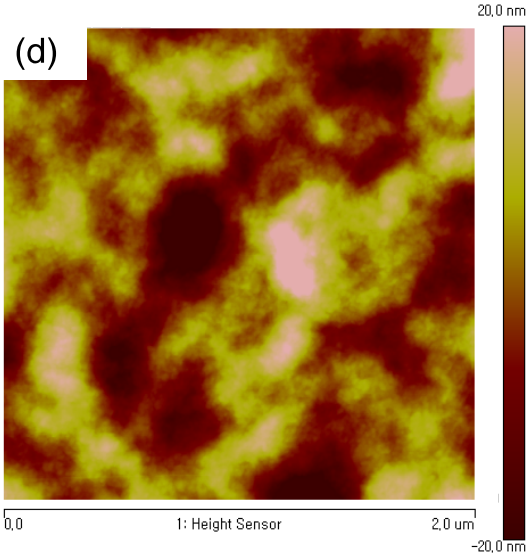
(d)
20,0 nm
0,0
1: Height Sensor
2,0 um
-20,0 nm

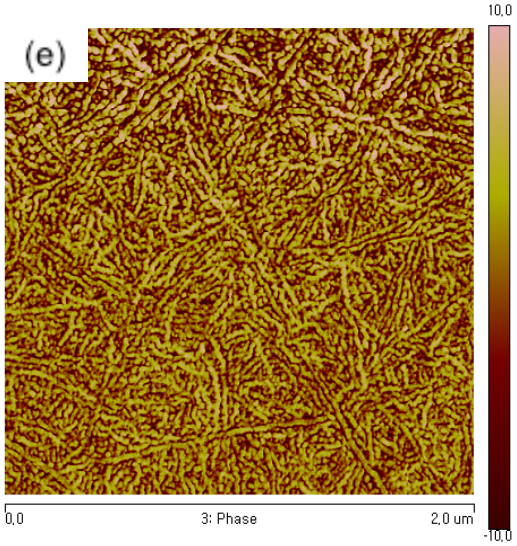
(e)
10,0
0,0
3: Phase
2,0 um
-10,0

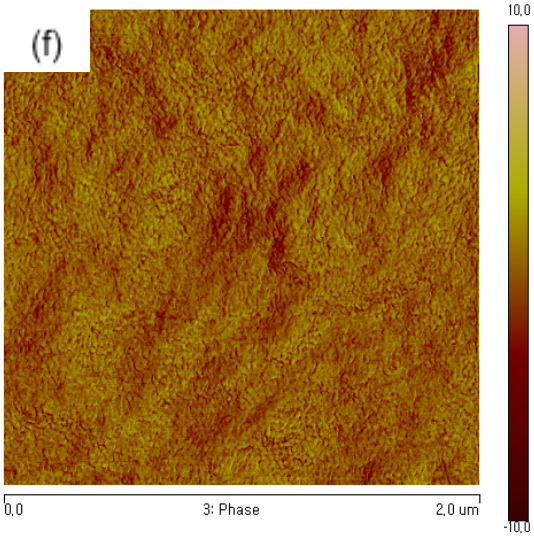
(f)
10,0
0,0
3: Phase
2,0 um
-10,0

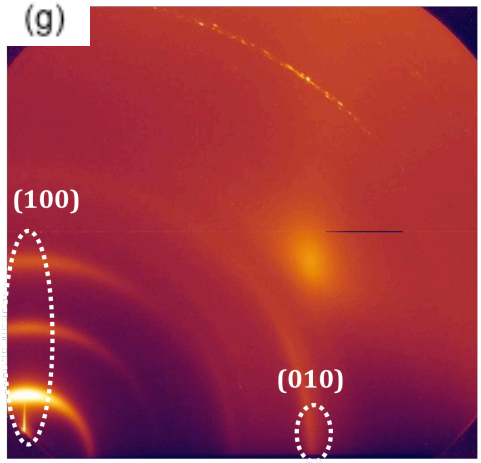
(g)
(100)
(010)

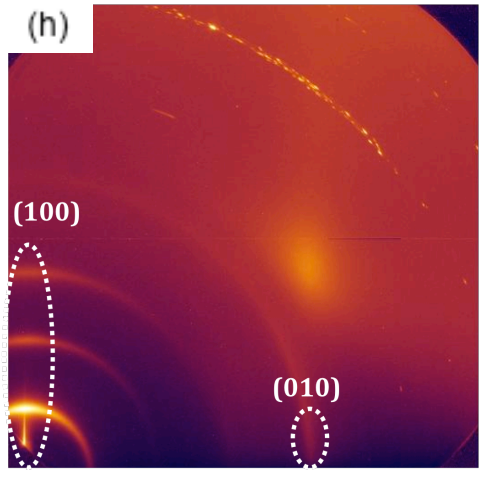
(h)
(100)
(010)

Figure 4.2 Characterization of P3HT nanodomains fabricated by ESSENCIAL (a, c, e, g) and spin-casting followed by thermal annealing (b, d, f, h): (a), (b) SEM images; (c), (d) AFM height images; (e), (f) AFM phase image; (g), (h) 2-D GIWAXS signals.

On top of P3HT nanodomains, PCBM acceptor was casted using another ESSENCIAL process to maximize the interdiffusion of PCBM into P3HT donor layer. The sequential casting of bilayer-type of structure was possible using the solvent having the orthogonality between donor and acceptor such as dichloromethane. In order to characterize the amount of PCBM penetrated into P3HT domains through the photoactive layer, dynamic secondary ion mass spectroscopy (DSIMS) was utilized (Figure 4.3). For this measurement, the deuterated PCBM having ^{2}H atoms that have the strong signal to DSIMS measurement was used to form the bilayer-based photoactive layer. The composition of P3HT in the photoactive layer was monitored by ^{32}S signal. Similar with the literature, PCBM could be diffused into P3HT layer through the whole depth during spin-casting (inverse triangle). Interestingly, the diffusion of PCBM molecules was efficient even in 350 nm scale thick P3HT layer. Even though further thermal annealing after spin-casting of PCBM (triangle) was beneficial to the migration of PCBM into P3HT layer, it was not so helpful to make more amount of PCBM penetrate into the P3HT layer. In contrast, ESSENCIAL process that can give longer solvent dwelling time during the process significantly increased the amount of PCBM (about three times) penetrated into P3HT layer even without any post annealing process. Recently, it has been reported that PCBM molecules diffuse through the amorphous phase of P3HT polymers during annealing process without disturbing any crystal domains of P3HT.[14,16] Therefore, it is expected that the large amount of PCBM molecules were diffused through the amorphous region between tens of nanometer scale crystallized P3HT nanowire

domains during ESSENCIAL process, which is helpful to form tens of nanometer scale heterojunction between donor and acceptor for efficient exciton dissociation. Furthermore, because PCBM molecules spontaneously form continuous pathways during diffusion into P3HT domains, bicontinuous phase photoactive layer without any isolated island nanodomains is expected. In BHJ structures, those isolated nanodomains are easily generated due to the random nature of the blend, as the thickness of photoactive layer is increased. Therefore the thermally annealed BHJ OSCs show the tendency that the fill factor is decreased as the thickness. However, during our process, because the donor phase is firstly formed and the acceptor forms continuous pathways during diffusion into donor phase, our bilayer-based devices can form efficient bicontinuous heterojunction. Therefore, the maximized crystallinity of donor phase, which come from the first ESSENCIAL process, and the bicontinuous nanodomains, which come from the second ESSENCIAL process inevitably give high carrier mobility.

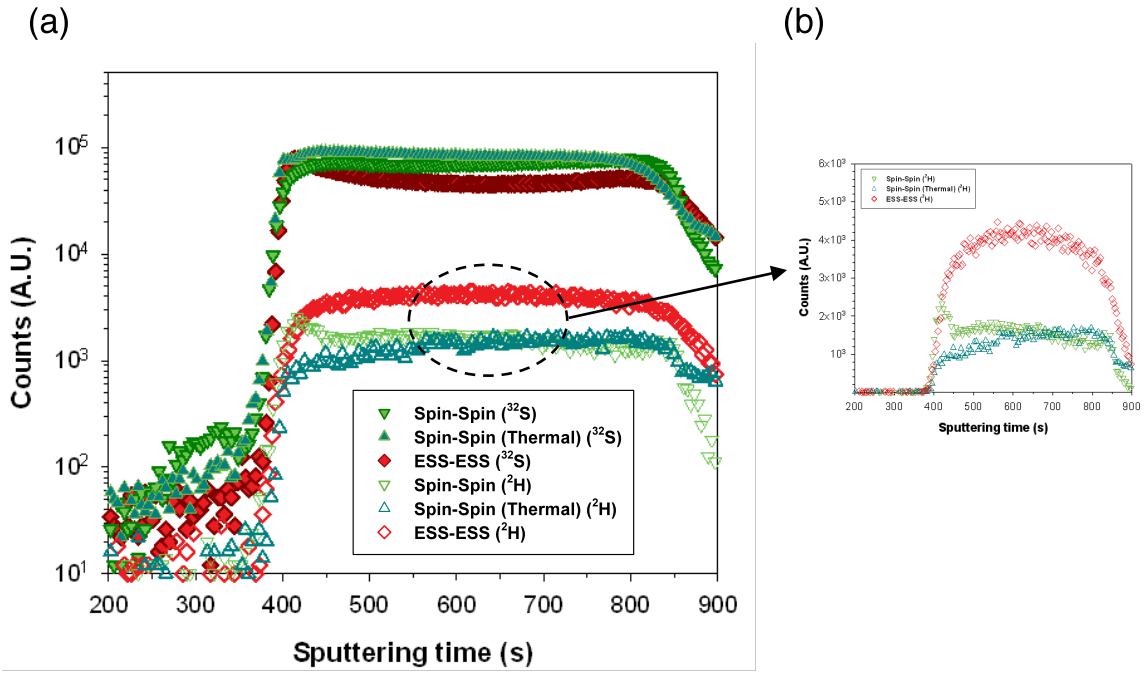

Figure 4.3 DSIMS results of photoactive layers composed of P3HT and deuterated PCBM. Inversed triangle, triangle, diamond represent the blend films made by spin-spin, spin-spin followed by thermal annealing, and ESSENCIAL-ESSEICIAL. Filled symbols and open symbols represent ^{32}S for P3HT and ^{2}H for PCBM, respectively: (a) log scale; (b) normal scale.

The carrier mobilities were characterized by photo-CELIV method. The photo-CELIV is an efficient method permitting us to calculate the mobility of carrier and recombination in low conductivity materials at the same time.[17-18] The detailed information about this method is explained in Chapter 3. As shown in Table 1, the devices which were fabricated by 2 step consecutive ESSENCIAL process (denoted as ESS-ESS) show the highest mobility value, and even the devices composed of spin-casted P3HT, having slight lower crystalline P3HT polymers than those by ESSENCIAL process, and PCBM layer formed by followed ESSENCIAL process show about 2 times higher mobility than thermally annealed BHJ devices. The BHJ devices used in this comparison have 320 nm thickness photoactive layer showing the best performances. This will be discussed more in device performances part.

Table 4.1 The calculated carrier mobilities by photo-CELIV depending on the different processing methods.

Method	Carrier mobility [10^{-4} cm^2 V^{-1} S^{-1}]
BHJ (Thermal annealed)	0.35
Spin-ESS	0.61
ESS-ESS	1.58

Using photo-CELIV method, we have studied the bimolecular recombination of charge carrier in photoactive layer. The recombination of photogenerated charges in OSC

devices is one of the most critical factors limiting the PCE. The recombination events in organic solar cells are classified into three categories. The exciton recombination, which happens when exciton are recombined before reaching interface between donor-acceptor, is negligible in efficient BHJ system having high device performance, because domain size is on the order of exciton diffusion length. The charge transfer state recombination, which happens when the excitons are recombined from the CT state at the interface, is also negligible in high performance donor and acceptor pairs. Therefore, the most crucial recombination is mobile charge carrier recombination, which happens when the dissociated charge is recombined during transportation as bimolecular recombination type. The bimolecular recombination rate has following equation (Equation 4.1).

$$\frac{dn}{dt} = \frac{dp}{dt} = -\beta(t)np \qquad \textbf{(Equation 4.1)}$$

where n, p are the concentration of electron and holes, respectively, and β is the bimolecular recombination coefficient. By integrating the photo-CELIV transients, the concentration of extracted charge carriers can be calculated at specific delay time between light pulse and extraction.[18] Figure 4.4a shows that the number of generated photo-charge in ESS-ESS device is the largest, and Spin-ESS device also showed larger amount of generated charges than thermally annealed BHJ devices. Furthermore, the bimolecular recombination constants of ESS-ESS devices, which were calculated by Equation 4.1 using experimental results in Figure 4.4a shows the lowest value, which means that the bimolecular recombination is significantly suppressed in ESS-ESS devices compared with conventional BHJ structures.

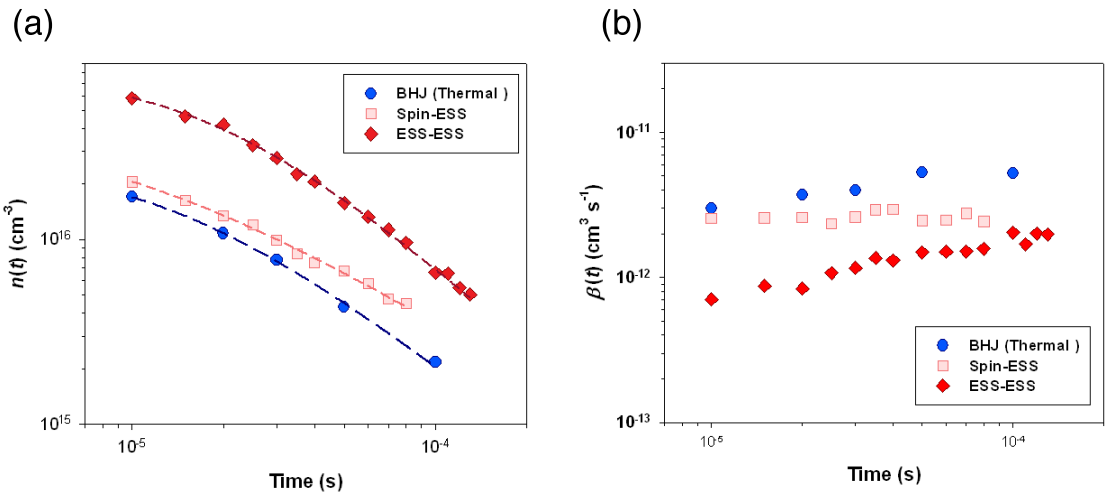

Figure 4.4 (a) The concentration of extracted charge carrier versus delay time between light pulse and extraction according to the different processing methods. (b) The calculated bimolecular recombination coefficient versus delay time according to the different processing methods.

The optimized heterojunction morphology in ESS-ESS devices was verified by calculating internal quantum efficiency (IQE). Recently, Mcgehee *et al.* reported the method to precisely calculate the IQE by considering parasitic absorption from the reflection spectrum of the solar cell devices.[19] The parasitic absorption in OSC structure was calculated by transfer matrix method and those signal was eliminated from the experimentally measured reflection spectrum of OSC device. Figure 4.5a shows the calculated absorption in photoactive layer, and the measured external quantum efficiency (EQE) is shown in Figure 4.5b. Following the relation (EQE = Absorption in active layer x IQE), IQE signals were calculated in Figure 4.5c. As expected, ESS-ESS devices having optimized morphology show the highest IQE value and this value is approaching 100 %, which means the most of the generated exciton are fully dissociated and transported to electrode without recombination.

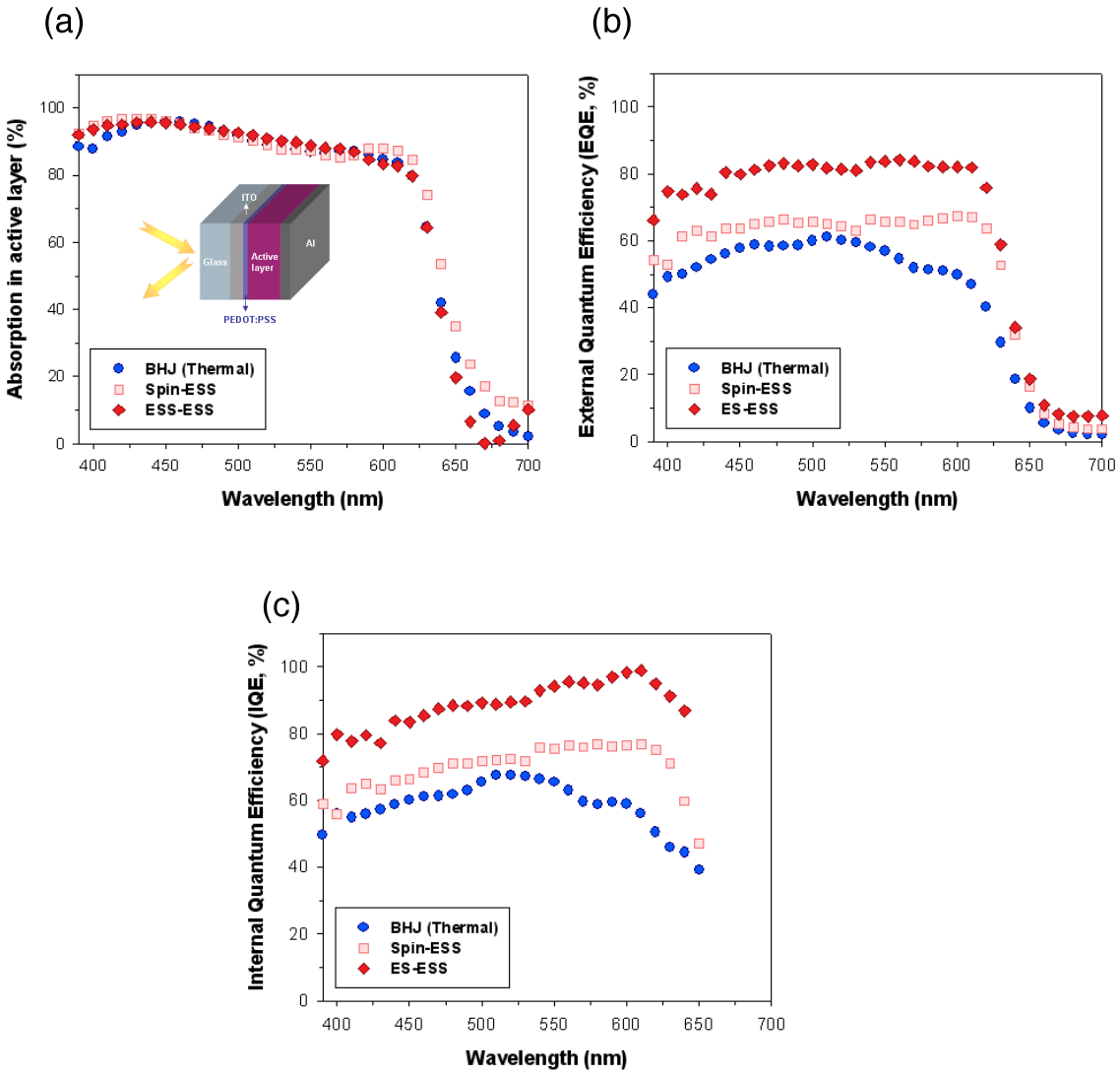

Figure 4.5 (a) The absorption efficiency in active layer. The parasitic absorption effect calculated by transfer matrix method was eliminated from the reflection spectrum of the real device. (b) External quantum efficiency measured by IPCE. (c) Calculated internal quantum efficiency.

The device performances are summarized in Table 4.2 and their *J-V* curves are displayed in Figure 4.6. As a thermally annealed BHJ condition, the devices with 320 nm thickness photoactive layer showing the highest performances were selected (Figure 4.7). Their PCEs were around 3.4 % with 9.84 ± 0.44 mA cm^{-2} short circuit current (J_{sc}) and 58.96 ± 1.20 % fill factor (FF). Compared with these solar cells, ESS-ESS devices having

optimized morphology as explained until now showed extremely high J_{sc} (15.10 ± 0.44 mA cm^{-2}) and FF (67.70 ± 5.00 %), and even spin-ESS device also showed high J_{sc} (12.41 ± 0.70 mA cm^{-2}). As shown in Figure 4.6b, the spin-casting of the second layer on hundreds of nanometer thick first layer using orthogonal solvent, even followed by thermal annealing, cannot efficiently make the layer be intermixed, and the device performances are not even compatible to BHJ structures. However, the increased solvent dwelling time during ESSENCIAL process significantly improved the performances of devices. In order to check if the solvent evaporation time is doing a crucial role in this processing, we fabricated solar cells by casting PCBM layer using gas-permeable stamp having faster solvent evaporation speed. Figure 4.6c represents that the solvent evaporation time is truly effective on the device performances, namely on the interdiffusion between layers.

The diffusion behavior of PCBM in P3HT crystalline domains has been also investigated by changing the regioregularity of P3HT. For this purpose, we have prepared devices composed of higher regioregularity (rr), > 98 %, instead of 91% rr-P3HT, which was used during all the other works. Figure 4.6c shows that the device performances are significantly decreased after changing the rr of P3HT. As depicted in Figure 4.6d, 98 % rr-P3HT may have smaller amorphous region, which PCBM molecules need to migrate, inducing poor heterojunction between P3HT and PCBM. Our results also support the recent findings from other research group that PCBM diffuse through the amorphous region of P3HT during annealing process.[14,16]

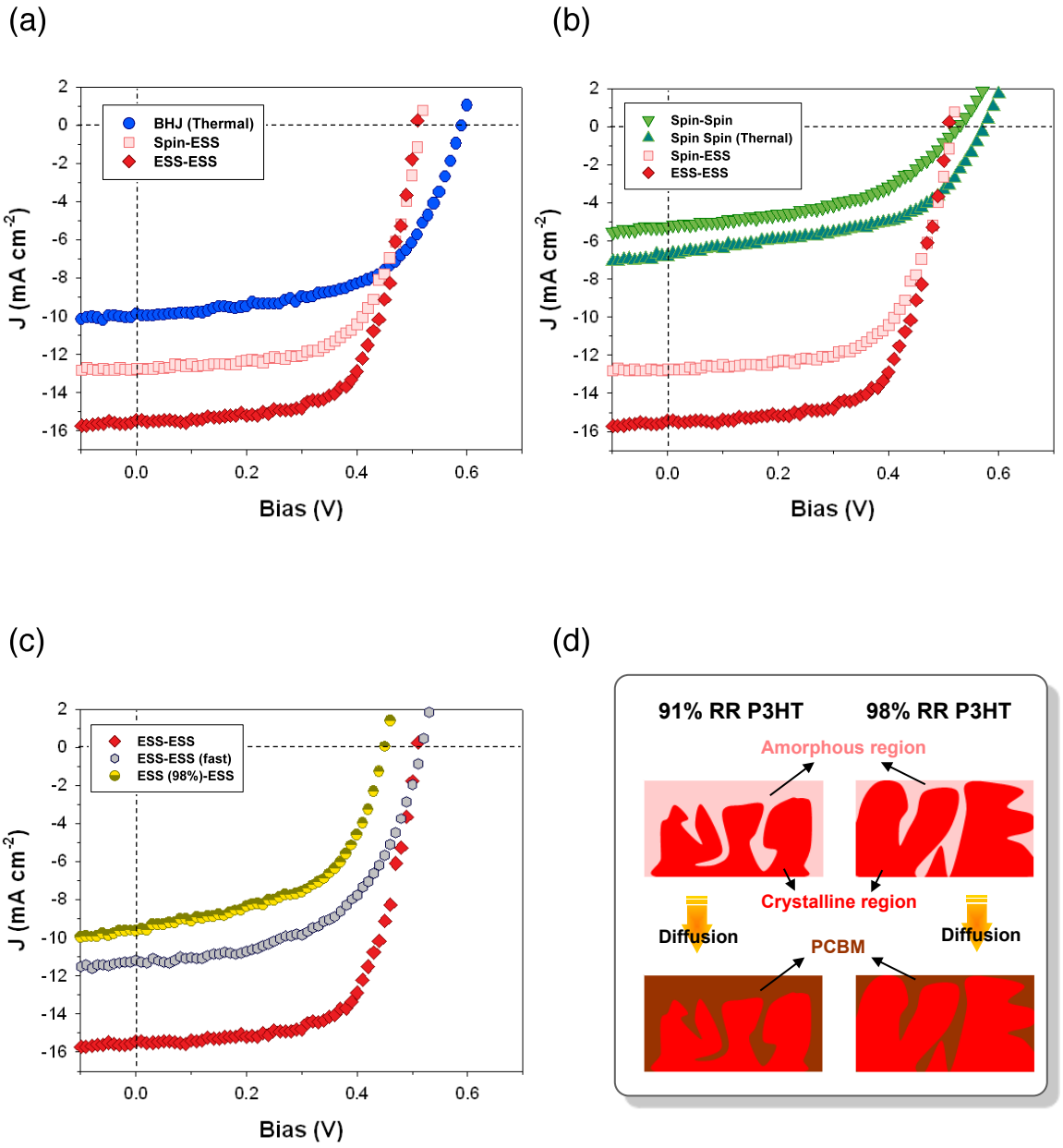

Figure 4.6 (a)-(c) *J-V* plots of solar cell devices according to the different fabrication process. Blue color circle, square, diamond, inverse triangle, triangle, grey color circle, and half yellow color circle represent BHJ (thermally annealed), spin-ESS, ESS-ESS, spin-spin, spin-spin (thermally annealed), ESS-ESS (fast evaporation of solvent) and ESS-ESS (98 % rr P3HT). (d) Schematic of diffusion process of PCBM into P3HT layers having different regioregularity during second ESSENCIAL process.

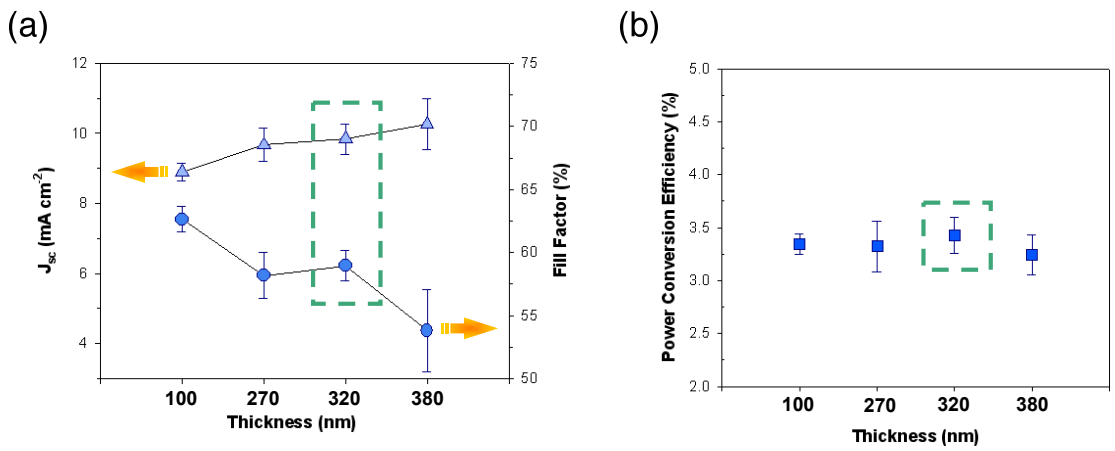

Figure 4.7 The device performances of thermally annealed P3HT:PCBM BHJ solar cells according to the photoactive layer thickness: (a) Short circuit current and fill factor; (b) Power conversion efficiency.

Table 4.2 Summary of device performances according to the different processing.

Method	J_{sc} [mA cm^{-2}]	V_{oc} (V)	FF (%)	PCE (%)
BHJ (Thermal annealed)	9.84 ± 0.44	0.59 ± 0.00	58.96 ± 1.20	3.43 ± 0.17
Spin-Spin	5.57 ± 0.54	0.52 ± 0.02	47.87 ± 2.06	1.40 ± 0.17
Spin-Spin (Thermal annealed)	6.88 ± 0.87	0.58 ± 0.00	47.28 ± 3.62	1.88 ± 0.31
Spin-ESS	12.41 ± 0.70	0.54 ± 0.03	60.98 ± 3.89	4.09 ± 0.30
ESS-ESS	15.10 ± 0.44	0.51 ± 0.01	67.70 ± 5.00	5.12 ± 0.32
ESS-ESS (fast evaporation)	11.43 ± 1.02	0.53 ± 0.01	53.67 ± 7.45	3.22 ± 0.42
ESS (98% rr)-ESS	9.12 ± 0.74	0.46 ± 0.01	44.06 ± 0.31	2.06 ± 0.41

4.4 Conclusion

We could develop the efficient photoactive heterojunction nanostructures by maximizing interdiffusion of donor and acceptor materials. The optimized morphology has maximized crystallinity, high carrier transportation, and low recombination coefficient, resulting in high IQE approaching almost 100 %. Consequently, the devices based on this type of structures showed significantly high photocurrent (over 50 % higher than that in thermally annealed BHJ devices). We expect that this new type of structure introduced in this work can help us further improve the performance of OSCs and understand underlying principles of OSCs.

4.5 References

1. Sariciftci, N. S., Smilowitz, L., Heeger, A. J. & Wudl, F. Photoinduced electron transfer from a conducting polymer to buckminsterfullerene. *Science* **258,** 1474–1476 (1992).
2. Yu, G., Gao, J., Hummelen, J. C., Wudl, F. & Heeger, A. J. Polymer photovoltaic cells: enhanced efficiencies via a network of internal donor-acceptor heterojunctions. *Science* **270**, 1789–1791 (1995).
3. Halls, J. J. M., Walsh, C. A., Greenham, N. C., Marseglia, E. A., Friend, R. H., Moratti, S. C. & Holmes, A. B. Efficient photodiodes from interpenetrating polymer networks. *Nature* **376**, 498–500 (1995).
4. Ma, W., Yang, C., Gong, X., Lee, K. & Heeger, A. J. Thermally stable, efficient polymer solar cells with nanoscale control of the interpenetrating network morphology. *Adv. Funct. Mater.* **16**, 1617–1622 (2005).

5. Li, G., Shrotriya, V., Huang, J., Yao, Y., Moriarty, T., Emery, K. & Yang, Y. High-efficiency solution processable polymer photovoltaic cells by self-organization of polymer blends. *Nature Mater.* **4**, 864–868 (2005).

6. Chen, H.-Y., Hou, J., Zhang, S., Liang, Y., Yang, G., Yang, Y., Yu, L., Wu, Y. & Li, G. Polymer solar cells with enhanced open-circuit voltage and efficiency. *Nature Photon.* **3**, 649–653 (2009).

7. Park, H. J., Kang, M.-G., Ahn, S. H. & Guo, L. J. Facile route to polymer solar cells with optimum morphology readily applicable to roll-to-roll process without sacrificing high device performances. *Adv. Mater.* **22**, E247–E253 (2010).

8. Krebs, F. C., Gevorgyan, S. A. & Alstrup, J. A roll-to-roll process to flexible polymer solar cells: model studies, manufacture and operational stability studies. *J. Mater. Chem.* **19**, 5442–5451 (2009).

9. Blankenburg, L., Schultheis, K., Schache, H., Sensfuss, S. & Schrödner, M. Reel-to-reel wet coating as an efficient up-scaling technique for the production of bulk-heterojunction polymer solar cells. *Sol. Energy Mater. Sol. Cells* **93**, 476–483 (2009).

10. Pivrikas, A., Neugebauer, H. & Sariciftci, N. S. Charge carrier lifetime and recombination in bulk heterojunction solar cells. *IEEE J. Sel. Top. Quantum Electron*., **16**, 1746–1758 (2010).

11. H. Hoppe, N. Arnold, N. S. Sariciftci, and D. Meissner, Modeling the optical absorption within conjugated polymer/fullerene-based bulkheterojunction organic solar cells. *Solar Energy Mater. Solar Cells*, **80**, 105–113 (2003).

12. Rand, B. P., Genoe, J., Heremans, P. & Poortmans, J. Solar cells utilizing small molecular weight organic semiconductors. Prog. Photovolt: Res. Appl., 15, 659–676

(2007).

13. Lee, K. H, Schwenn, P. E., Smith, A. R. G., Cavaye, H., Shaw, P. E., James, M., Krueger, K. B., Gentle, I. R., Meredith, P. & Burn, P. L. Morphology of all-solution-processed "bilayer" organic solar cells. *Adv. Mater.* 23, 766–770 (2011).
14. Chen, D., Liu, F., Wang, C., Nakahara, A. & Russell, T. P. Bulk heterojunction photovoltaic active layers via bilayer interdiffusion. *Nano Lett.* **11**, 2071–2078 (2011).
15. Kim, S.-S., Na, S.-I., Jo, J., Tae, G. & Kim, D.-Y. Efficient polymer solar cells fabricated by simple brush painting. Adv. Mater. 19, 4410–4415 (2007).
16. Treat, N. D., Brady, M. A., Smith, G., Toney, M. F., Kramer, E. J., Hawker, C. J. & Chabinyc, M. L. Interdiffusion of PCBM and P3HT Reveals Miscibility in a Photovoltaically Active Blend. *Adv. Energy Mater.* 2011, ***1***, 82–89 (2011).
17. Juška, G., Arlauskas, K., Viliunas, M. Extraction Current Transients: New method of study of charge transport on microcrystalline silicon. *Phys. Rev. Lett.* **84**, 4946-4949 (2000).
18. Mozer, A. J., Dennler, G., Sariciftci, N. S., Westerling, M., Pivrikas, A., Österbacka, R. & Juška, G. Time-dependent mobility and recombination of the photoinduced charge carriers in conjugated polymer/fullerene bulk heterojunction solar cells. Phys. Rev. B 72, 035217 (2005).
19. Burkhard, G. F., Hoke, E. T. & McGehee, M. D. Accounting for interference, scattering, and electrode absorption to make accurate internal quantum efficiency measurements in organic and other thin solar cells *Adv. Mater.* **22**, 3293–3297 (2010).

CHAPTER 5

Sub-20 nm Nanostructures Fabricated by Block Copolymer Template for Nanoimprint Lithography and Their Application to Organic Solar Cells

5.1 Introduction

BHJ structure has advantages to access the domain size of donor-acceptor component within the exciton diffusion length scale and to give the large interfacial area facilitating the exciton dissociation at the interface, however, the randomly interspersed electron-donor and -acceptor phases can lead to charge trapping in the isolated region inducing poor charge transport pathway. Therefore, vertically interdigitated donor-acceptor structures within exciton diffusion length scale have been known to the ideal solar cell structures to maximize the dissociation of photogenerated excitons and the transportation of free charge carriers. There have been previous attempts to realize the idealized OSC structures, however, no one has successfully demonstrated these types of structures within 20 nm domain scale using the conjugate polymer and fullerene derivate as a donor and acceptor pair, which have shown the state-of-the-art PCE in the OSC research.[1-4] One of the major challenges to realize this type of structure is the difficulty to access those periodic pillar and hole structures of tens of nanometer pitch. Electron beam lithography and focused ion beam (FIB) lithography are widely used methods to fabricate these types of patterns for which conventional photolithography faces resolution limit. However, the time consuming process and the high cost associated with such techniques seriously

restrict the large-scale production of high density nanopatterns. As alternatives, nanotemplate approaches using track-etched membrane[5] and anodized aluminum oxide (AAO)[6] have been extensively used to produce tens of nanometer scale patterns. However the poor adhesion of template to a substrate, the harsh processing conditions to remove the template or the resolution of the patterns often limit these pattern transferring techniques.

Recently, the self-assembly behavior of diblock copolymers has drawn significant attentions for nanotemplate fabrication.[7] It is well known that the self-organization of block copolymer can access complex nanostructures. The density and the dimension of such self-organized nanostructures are usually beyond the reach of typical conventional top-down nanofabrication techniques.[8] Furthermore, various techniques that have been developed to control the orientation of the nanoscale morphology in the thin film make it possible for these self-organized nanostructures to be used as templates for various applications.[7,9-10] Despite the numerous advantages of these nanotemplates fabricated by block copolymer self-assembly, the long processing time needed to develop the self-assembled structures has drastically reduced the potential impact of this versatile nanopatterning technique. To overcome this limitation, I report in this chapter reliable and practical methods of fabricating SiO_2 molds for nanoimprint lithography (NIL) using the block copolymer template, which were then used in NIL for high speed nanopatterning.[11-12] Such an approach represents a big step forward to mass production of nanostructures with dimension, density and areal coverage only accessible by the block copolymer self-assembly process.

NIL is a promising lithographic technique capable of replicating large area nanostructures with resolution down to a few nm. Though there have been previous reports to fabricate SiO_2 or Si nanostructures using self-assembled block copolymer template, the processing methods were not straightforward for both pillar and hole polarity patterns and none has succeeded in applying those nanostructures to NIL.[13-16] In this chapter, polymer nanotemplate originated from PS-PMMA diblock copolymer was successfully transferred to high density, high aspect ratio sub-20 nm SiO_2 nanopillar and nanohole structures over a large area using the novel processing techniques. Not only can NIL create resist patterns, as in a lithographic process, but can also imprint functional device structures in various polymers, which can lead to a wide range of applications.[17] Imprinting results show that densely packed sub-20 nm nanopillar and nanohole polymer patterns can be easily fabricated on arbitrary substrate. Ultimately, it is possible to develop sub-20 nm conjugated polymer patterns on ITO transparent electrode, which are promising structures for interdigitated OSC structure.

5.2 Experimental details

5.2.1 Block copolymer nanotemplate

Si wafers with 500 nm thick thermal oxide were as substrate for the block copolymer self-assembly and subsequently for NIL mold fabrication. These substrates were cleaned in a hot piranha solution (1:1 mixture of H_2SO_4 and H_2O_2) for 1 h, and were subsequently washed with deionized water for 30 min. After the cleaning process, the substrate surface was modified by using the polystyrene-*r*-poly(methyl methacrylate) (PS-*r*-PMMA) random copolymer. The PS-*r*-PMMA layer was spin-coated on the substrate and

subsequently thermally annealed at 165 °C for 48 h in a vacuum. After the annealing, the substrate was washed by toluene to remove unreacted random copolymer. After the surface treatment, a thin film of PS-*b*-PMMA diblock copolymer (70 vol.% PS) was spin-coated and annealed at 185 °C for 24 h to develop cylindrical nanodomains oriented normal to the surface. The PMMA domains in the nanostructure were selectively removed by O_2 plasma (20 sccm O_2, 12 mTorr chamber pressure, and 30 W bias power). The resultant PS nanostructure was used as a starting template for the subsequent pattern transferring to the SiO_2 layer.

5.2.2 Pattern transfer into SiO_2 layer for NIL

To fabricate nanohole arrays in SiO_2, a 5 nm thick Cr was deposited with an incident angle of 45° to the PS template at a rate of 2Å/s using an electron-beam evaporator. After the Cr deposition, reactive ion etching (RIE) (50 sccm C_2F_6 / 50 sccm He / 60 sccm Ar / 10 sccm O_2, 60 mTorr chamber pressure, and 50 W bias power) was performed to etch the SiO_2 layer using the Cr pattern as a etch mask.

In order to fabricate SiO_2 pillar structure, a 5 nm Cr was deposited normal to the PS template at a rate of 2Å/s using the electron-beam evaporator. Subsequently, RIE (25 sccm Cl_2 / 5 sccm O_2, 10 mTorr chamber pressure, and 30 W bias power) was used to etch the Cr layer that was deposited on the top and the sidewalls of PS template. Cr dots remained at the bottom of the PS nanoholes as discussed in the results & discussion section. Then a lift-off step was performed by immersing the sample in toluene for 1 min at room temperature. It was easily observed that all PS templates were quickly dissolved in toluene. Using the remaining Cr dots as a etch mask, SiO_2 layer was etched by RIE to

produce dense nanopillars by using the same etch condition as that used to fabricate the SiO_2 hole structures.

5.2.3 NIL using molds of both pattern polarities made in SiO_2

In order to fabricate nanoimprinted polymer nanotemplate, PMMA solution in toluene was spincoated on a substrate to an appropriate thickness (as determined by the feature depth on the mold) and imprinted in a Nanonex NX2000 nanoimprinter (Princeton, NJ) at a pressure of 600 psi and a temperature of 180 °C for 5 min by using SiO_2 nanopillar mold. Every SiO_2 mold used in the NIL experiment was treated with surfactant, (tridecafluoro-1,1,2,2-tetrahydrooctyl) trichlorosilane (GELEST). After depositing a 5 nm thick Cr at a rate of 2Å/s in an electron-beam evaporator with an incident angle of 45° to the substrate, the residual layer of the imprinted polymer template was removed by an anisotropic O_2 plasma etch (20 sccm O_2, 12 mTorr chamber pressure, and 30 W bias power) .

Both nanohole PDMS stamps were fabricated using the nanopillar SiO_2 molds. After treating the substrate by methoxysilane having vinyl groups, a high modulus PDMS solution[18] was dropped on the substrate and subsequently covered by the SiO_2 mold. The PDMS was cured at 120 °C for 5 min under a pressure of 5 psi.

Poly(3-hexylthiophene) (P3HT) was purchased from Rieke metal (4002E grade) and spin-coated on a PEDOT:PSS layer (Clevios PH 500) that was also spin-coated on the ITO coated PET. P3HT layer was imprinted in a custom built nanoimprinter (750 psi, 185 °C, 15 min).

5.3. Results and discussion

5.3.1 NIL molds fabrication

NIL molds fabrication. The overall processes for fabricating the NIL molds are described in Figure 5.1. A SiO_2 layer, which was thermally grown on Si wafer surface, was firstly treated by polystyrene-r-poly(methyl methacrylate) (PS-r-PMMA) random copolymer to produce the neutral surface to polystyrene (PS) and poly(methyl methacylate) (PMMA). Subsequently, PS-b-PMMA diblock copolymer that has 0.7 volume fraction of PS was spincoated and annealed above the glass transition temperature of the copolymer for the self-assembly process to proceed. This process results in the equilibrated morphology of hexagonally packed cylinders. The identical interfacial tension provided by the neutral PS-r-PMMA layer to each block of the PS-b-PMMA copolymer on the surface eventually lead to vertically oriented cylindrical PMMA nanodomains surrounded by PS. This morphological structure could be used to fabricate PS nanotemplate with hole arrays by removing the PMMA cylindrical nanodomain utilizing the etching selectivity between PS and PMMA to O_2 plasma etching. The resultant PS template with nanohole array patterns is shown in Figure 5.2a.

There have been previous attempts to directly use the PS template as an etching mask to transfer the block copolymer patterns to other materials,[13-14] however, the soft PS mask is not strong enough as an etch mask to produce structures with high aspect ratios. Here by using a few nm Cr deposited at an angle to the substrate (i.e. shadow evaporation), we could successfully transfer the block copolymer patterns into SiO_2 layer having almost 1:10 aspect ratio. Cr was chosen because it is extremely resistant to the RIE gases used to etch oxide materials. Cr was selectively deposited on the top surface of PS template by

angled deposition and this Cr layer acted as the actual mask to etch SiO_2 layer rather than PS. The resultant SiO_2 hole arrays with 20 nm diameter and 150 nm depth are shown in Figure 5.2b.

The PS nanotemplate from PS-b-PMMA block copolymer patterns was also used to fabricate SiO_2 nanopillars. Again Cr was selected as an etch mask. Initially we tested the conventional lift-off process by depositing Cr on the PS template and subsequently dipping the sample into toluene in order to lift-off the Cr film on top of the PS template while leave the Cr pattern at the bottom of the nanoholes. However even by harsh processing condition, such as 3 h sonication at 60 °C, only small areas of PS template were dissolved and most areas of PS template remained on the substrate. This is due to the Cr metal deposited on the sidewall of porous PS template that is not perfectly vertical to the substrate. These problems are usually solved by making undercut structure to prevent metal from being deposited on the sidewall; however, the weak etching property of the PS template does not allow such process. Our solution to this problem is based on an observation that the ions in RIE plasma etch are difficult to reach to the bottom of the nanoholes in the PS template under the moderate condition, which is due to the high aspect ratio of the nanoholes and the small hole openings. Therefore by inserting a Cr RIE etching step before lift-off in organic solvent, as shown in processing flows in Figure 5.1, we confirmed that the lift-off was thoroughly completed in only 1 min while leaving the Cr dots at the bottom of the nanoholes. Well-defined and uniform SiO_2 nanopillars, shown in Figure 5.2c, fabricated by further etching of SiO_2 layer after the lift-off are clear evidence of this successful process, and we were able to fabricate densely packed SiO_2 nanopillar structures with 1:10 aspect ratio. Because of the freedom to insert a hard etch

mask for the fabrication of both polarity of patterns, the aspect ratio and the shape of the SiO_2 nanostructure are easily controllable, and the pattern transfers to the substrate materials other than SiO_2 are also possible, simply by choosing the appropriate metal masks that are resistant to the RIE chemistry for etching the target layer.

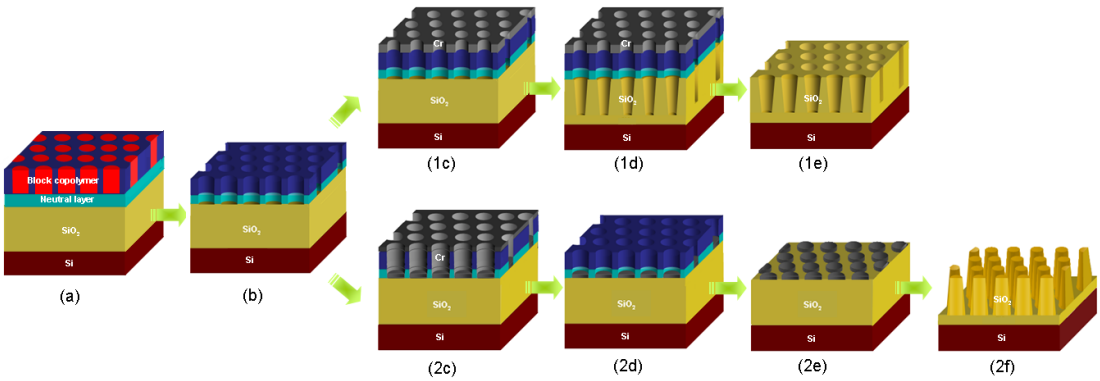

Figure 5.1 Schematic of the process for fabricating both nanohole and nanopillar array patterns in SiO_2 (a) cylindrical PS-b-PMMA morphology is developed on the substrate surface modified by the neutral PS-r-PMMA layer. (b) PMMA nanodomains are selectively removed by O_2 plasma etching. (1c-e) nanohole arrays fabrication process [(1c) Cr is selectively deposited on polymer template using shadow evaporation. (1d) SiO_2 layer is etched using Cr mask by RIE. (1e) Cr mask and polymer template are removed for SiO_2 and form nanohole arrays.], (2c-f) nanopillar arrays fabrication process [(2c) Cr is deposited over the polymer template. (2d) top Cr layer is removed by Cr etching RIE. (2e) Cr nanodots remained after lift-off. (2f) SiO_2 layer is etched using Cr mask by RIE and Cr masks are subsequently removed.]

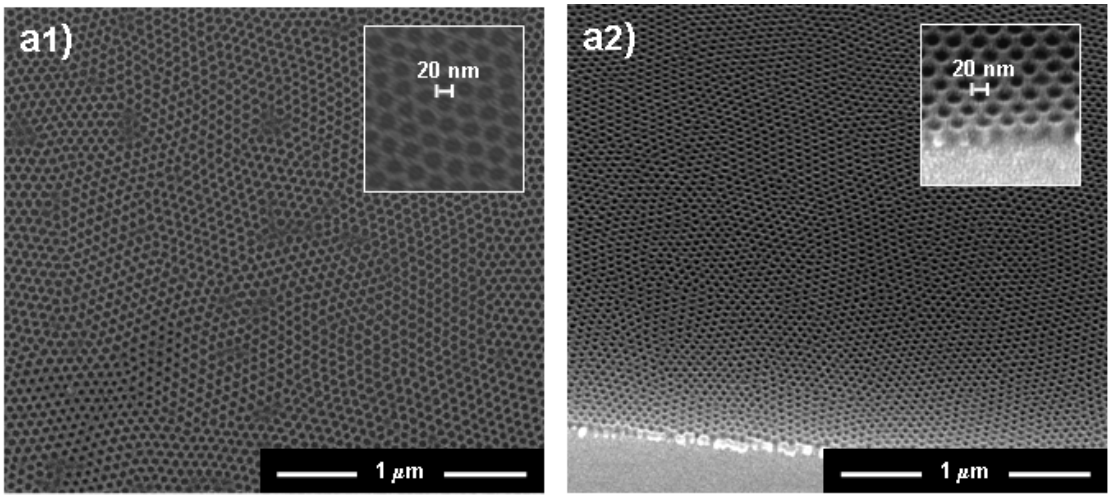

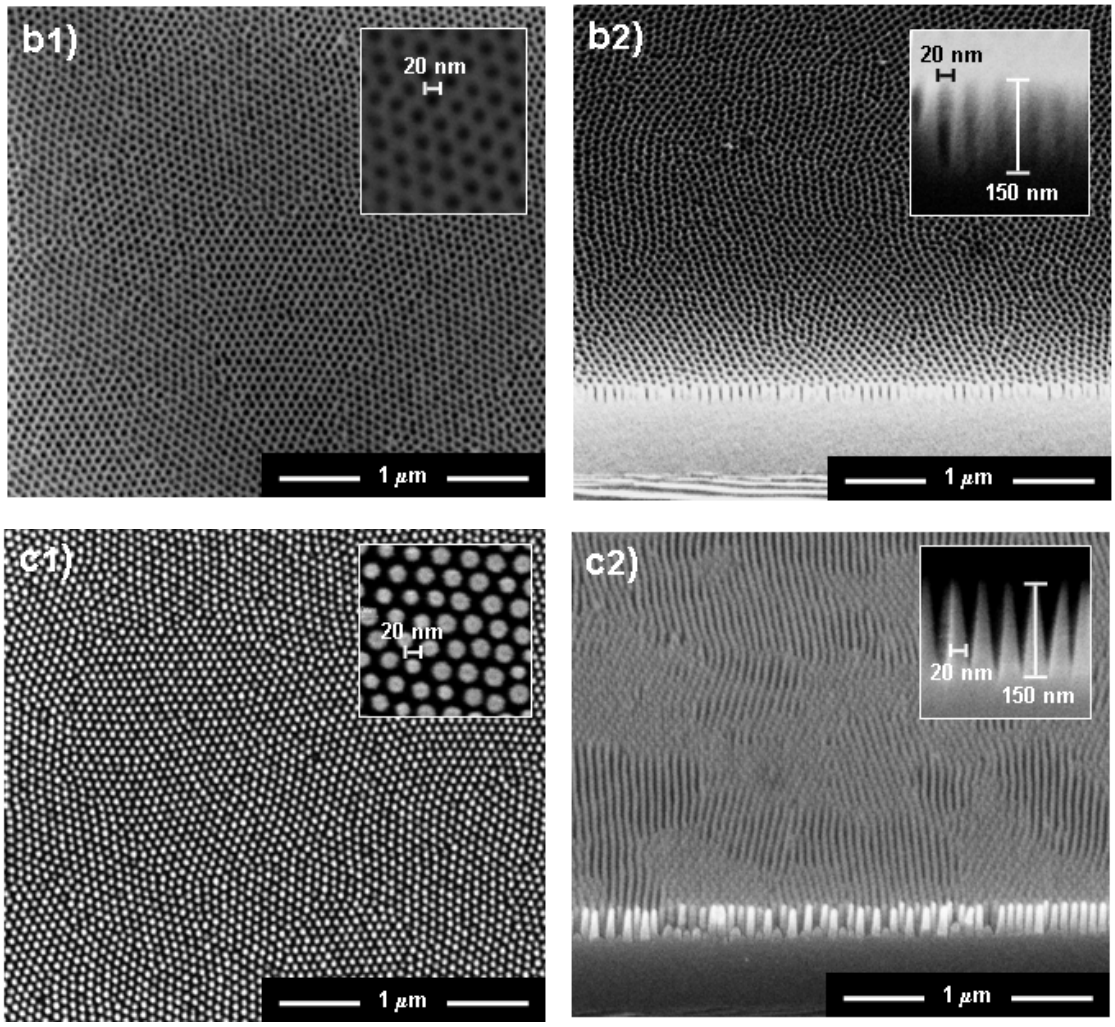

Figure 5.2 SEM micrographs of various nanostructures (left column: top view; right column: perspective view at 45° tilt angle). a) PS template fabricated by etching away the PMMA nanodomains of the self-assembled PS-b-PMMA hexagonal patterns. b) SiO_2 nanohole structure. c) SiO_2 nanopillar structure. All the inset images are high magnification SEM images; and the inset images in b2 and c2 show the cross-section view of the nanostructure in the fabricated SiO_2 mold.

5.3.2 Nanoimprinting polymer resist on arbitrary substrates

The nanoimprint molds of both pattern polarities made in SiO_2 described above can be used to fabricate various functional nanostructures. For example, using the nanopillar mold fabricated here, it is straightforward to reproduce the nanohole template similar to that produced by the block copolymer self-assembly process in essentially any polymers in a short time by using the NIL technique. As shown in Figure 5.3a, a PMMA template

with densely packed nanoholes was generated by a simple thermal nanoimprinting step using nanopillar mold at a temperature of 180 °C and a pressure of 600 psi within a few min. To use them as masks for further pattern transferring into a substrate or to produce a porous PMMA membranes, the residual layer of the imprinted PMMA pattern could be easily removed by a subsequent O_2 plasma after an angled-deposition of a metal mask such as Cr on top of the imprinted PMMA to reinforce the etching resistance, as shown in Figure 5.3b.

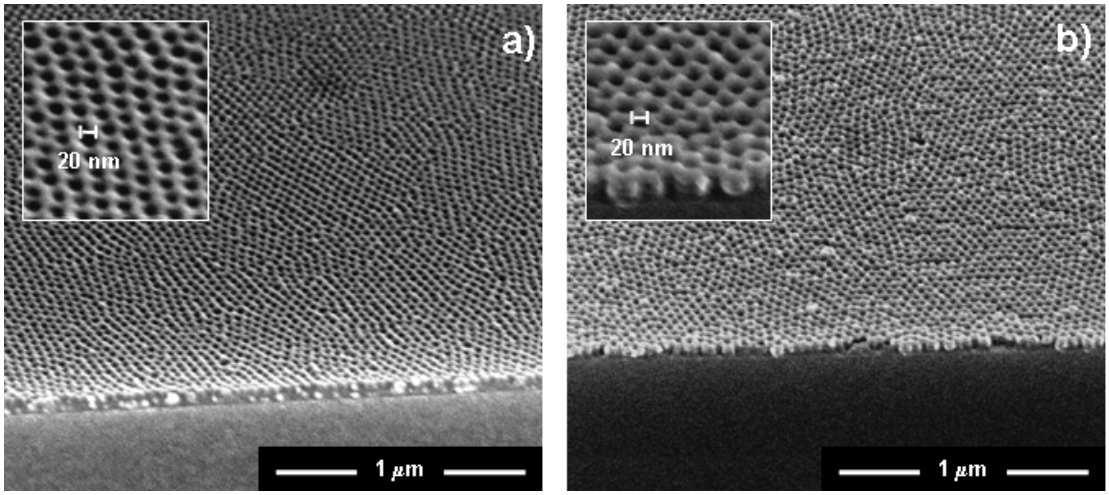

Figure 5.3 SEM micrographs of a) PMMA nanotemplate imprinted by SiO_2 nanopillar mold. b) PMMA nanotemplate of which the residual layer was removed by O_2 plasma using Cr mask deposited by angled evaporation. Both of inset images are the high magnification SEM images. All the images are 45° tilted views.

5.3.3 Conjugated polymer patterns fabrication for OSC

Vertically oriented sub-20 nm nanohole and nanopillar structures made in conjugated polymers are highly desirable structures for organic solar cells (OSCs). To achieve high efficiency OSCs, it is most essential to produce interpenetrating networks of an electron-donor and an electron-acceptor material. It is desirable to limit the size of each domain within the exciton diffusion length, which has been measured to be 4-20 nm.[19-23] By

making such controlled nanoscale morphology between the donor and the acceptor, and having the donor-acceptor interface vertically oriented to the cathode and the anode,[1] the excitons can be fully dissociated to electrons and holes, and can be efficiently transported to the electrodes before recombination. Here, as an initial effort to produce the ideal interdigited interface structure, we attempted to imprint directly a regioregular poly(3-hexylthiophene) (rr-P3HT) having high crystallinity. This material is one of the most widely used donor materials in making the OSCs. Figure 5.4 shows that the fabrication of sub-20 nm hole- and pillar-type nanostructures in conjugated polymer is possible using the SiO_2 molds of both polarity patterns. The nanoimprint process, carried out at 185 °C and 750 psi, is successful despite that the high crystallinity of the rr-P3HT may prevent the polymer chains from flowing easily. The aspect ratio of the imprinted P3HT nanostructures can be controlled by adjusting the imprint temperature, time and pressure.

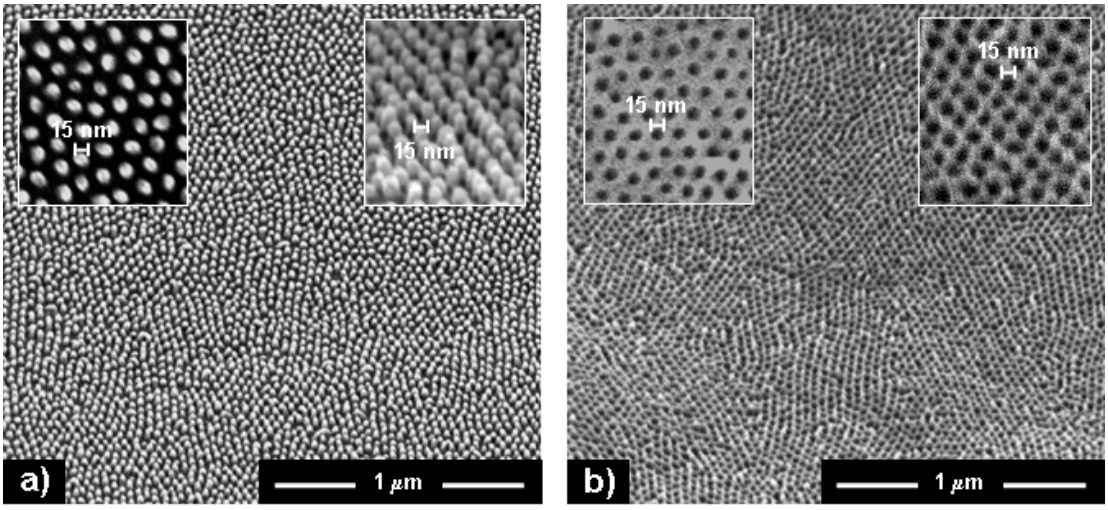

Figure 5.4 SEM micrographs of a) imprinted P3HT nanopillars taken at 45° tilted view. The inset images on the left and right provide high magnification top view and 75° tilted view respectively. b) The 45° tilted view of imprinted P3HT nanoholes. The left and right inset images are high magnification top view and 45° tilted view of the structure, respectively.

One of the major requirements for the active layer in OSC is that it should absorb a significant fraction of the sunlight. It has been known that, at a P3HT film with thickness of 240 nm, over 95% of the incident light (neglecting reflective losses) is absorbed within the wavelength range 450-600 nm and at least 120 nm film thickness is needed to absorb about 90 % of the incident light.[24] The simple thermal nanoimprinting step can give P3HT nanoholes structures having appropriate thickness to efficiently absorb the incident light, however, the height of P3HT nanopillar structures fabricated by this method (15 nm diameters, ~ 2.5 aspect ratio), which are expected to give 55 ~ 70 nm thickness donor layer (20 ~ 30 nm residual layer and 35 ~ 40 nm pillar height), is not enough to give efficient film thickness. The ESSENCIAL method, suggested in chapter 2, can be modified to give a solution to this problem (Figure 5.5). Because the crystallinity of P3HT film even just after spin-casting is high enough to prevent polymer chains from easily flowing into the SiO_2 hole type mold, imprinting was performed using gas-permeable hole type mold, shown in Figure 5.6a, and the blend solution. The fabrication of the gas-permeable hole type mold having dense sub-20 nm features was possible due to the use of a hard PDMS layer possessing a higher modulus. Higher modulus is necessary to effectively prevent the collapsing of the replicated nanopatterns.[18] The high aspect ratio (~ 4.5) P3HT pillar having 15 nm diameters, shown in Figure 5.6b, can be used as efficient donor layer for ideal interdigitated OSC structures.

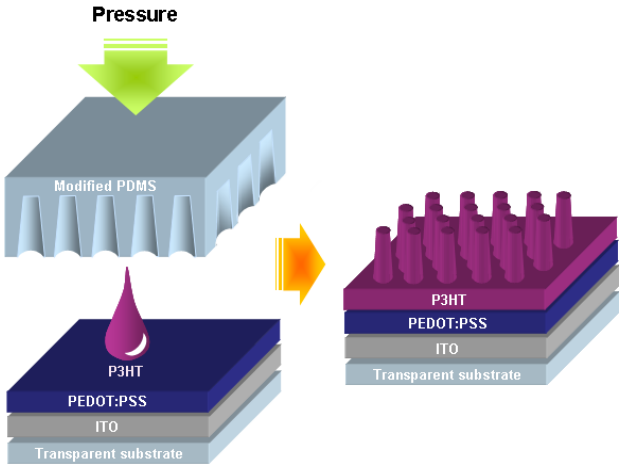

Figure 5.5 ESSENCIAL process for high aspect ratio nanopillar type structure fabrication.

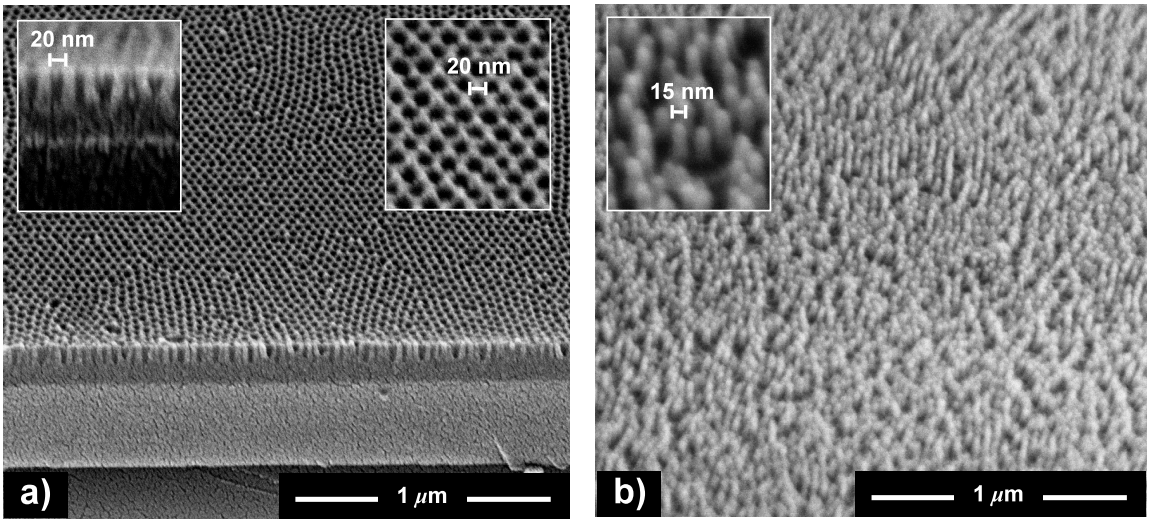

Figure 5.6. SEM micrographs showing (a) nanohole-type PDMS soft stamp imprinted by SiO2 nanopillar mold and (b) high aspect ratio sub-20nm P3HT nanopillar structure fabricated by ESSENCIAL process using nanohole-type PDMS stamp.

5.4 Future work for device fabrication

Because the spin-casting is not proper to the uniform layer deposition on tens of nanometer scale structures without voids, another ESSENCIAL process to form uniform acceptor layer can be used. As a solvent, the orthogonal solvent between donor and

acceptor such as methylene chloride can be used. During this step, the hard PDMS with hundreds of nanometer scale patterns, designed to maximize the diffraction of light near the absorbance range of donor materials, can be used instead of flat PDMS. These types of patterns are expected to form the electrode to enhance the intensity of the reflected light as shown in Figure 5.7.

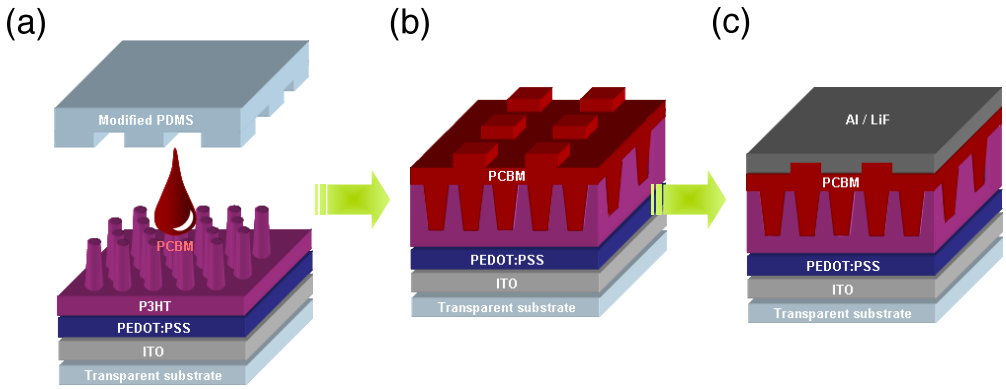

Figure 5.7 (a)-(b) ESSENCIAL process to uniformly deposit the acceptor layer, which has hundreds of nanometer patterns, on the nanopatterns of donor layer. (c) The light diffraction enhanced cathode is fabricated by further metal deposition.

5.5 Conclusion

In summary, densely packed, high aspect ratio nanopillar and nanohole SiO_2 structures were successfully fabricated using block copolymer template, and their versatile utilities for nanoimprint lithography were demonstrated. Because it is well known that the block copolymer patterns formation and the NIL are scalable, our process can be extended to large area applications. Block copolymer nanotemplate was used to produce nanohole-type SiO_2 mold by using the angle-deposited Cr mask that reinforced self-assembled patterns formed in block copolymer; and to produce nanopillar-type SiO_2 mold using a novel lift-off method to utilize the Cr islands masks left at the bottom of the

template. Additionally, these successful applications of the Cr mask in these processes made it possible to freely control the aspect ratio of those etched structures by changing the RIE conditions. Nanoimprint lithography using those SiO_2 nanostructures provided an effective way to replicate block copolymer like high density and large area nanopatterns on arbitrary substrates using various polymers (*e.g.* conjugated polymers) in short processing time. In addition, the nanostructured PDMS stamps fabricated by using the SiO_2 molds are promising tools for soft lithography and can be applied to fabricate sub-20 nm high aspect ratio nanopillars for ideal interdigitated heterojunction photoactive layer in OSC.

5.6 References

1. Kim, M.-S., Kim, J.-S., Cho, J., Stein, M., Guo & L. J., Kim, J. Flexible conjugated polymer photovoltaic cells with controlled heterojunctions fabricated using nanoimprint lithography. *Appl. Phys. Lett.* **2007**, 90, 123113.
2. Cheyns, D., Vasseur, K., Rolin, C., Genoe, J., Poortmans, J. & Heremans, P. Nanoimprinted semiconducting polymer films with 50 nm features and their application to organic heterojunction solar cells. *Nanotechnology* **2008**, 19, 424016.
3. Aryal, M., Buyukserin, F., Mielczarek, K., Zhao, X.-M., Gao, J., Zakhidov, A. & Hu, W. Imprinted large-scale high density polymer nanopillars for organic solar cells. *J. Vac. Sci. Technol. B* **2008**, 26, 2562-2566.
4. Yang, F., Shtein & M., Forrest, S. R. Controlled growth of a molecular bulk heterojunction photovoltaic cell. *Nature Mater.* **2005**, 4, 37-41.

5. Martin, C. R. Nanomaterials: A membrane-based synthetic approach. *Science* **1994**, 266, 1961-1966.

6. Shimizu, T., Xie, T., Nishikawa, J., Shingubara, S., Senz, S. & Gösele, U. Synthesis of vertical high-density epitaxial Si(100) nanowire arrays on a Si(100) substrate using an anodic aluminum oxide template. *Adv. Mater.* **2007**, 19, 917-920.

7. Hawker, C. J. & Russell, T. P. Block Copolymer Lithography: Merging "Bottom-Up" with "Top-Down" Processes. *MRS Bull.* **2005**, 30, 952-966.

8. Bates, F. S. & Fredrickson, G. H. Block Copolymer Thermodynamics: Theory and Experiment. *Annual Rev. Phys. Chem.* **1990**, 41, 525-557.

9. Huang, E., Rockford, L. & Russell, T. P., Hawker, C. J. Nanodomain Control in Copolymer Thin Films. *Nature* **1998**, 395, 757-758.

10. Ryu, D. Y., Shin, K., Drockenmuller, E., Hawker, C. J. & Russell, T. P. A Generalized Approach to the Modification of Solid Surfaces. *Science* **2005**, 308, 236-239.

11. Chou, S. Y., Krauss, P. R. & Renstrom, P. J. Imprint Lithography with 25-Nanometer Resolution. *Science* **1996**, 272, 85-87.

12. Guo, L. J. Nanoimprint Lithography: Methods and Material Requirements. *Adv. Mater.* **2007**, 19 495-513.

13. Jeong, S.-J., Xia, G., Kim, B. H., Shin, D. O., Kwon, S.-H., Kang, S.-W. & Kim, S. O. Universal Block Copolymer Lithography for Metals, Semiconductors, Ceramics, and Polymers. *Adv. Mater.* **2008**, 20, 1898-1904.

14. Black, C. T., Guarini, K. W., Breyta, G., Colburn, M. C., Ruiz, R., Sandstrom, R. L., Sikorski, E. M. & Zhang, Y. Highly Porous Silicon Membrane Fabrication Using Polymer Self-Assembly. *J. Vac. Sci. Technol. B* **2006**, 24, 3188-3191.

15. Gowrishankar, V., Miller, N., McGehee, M. D., Misner, M. J., Ryu, D. Y., Russell, T. P., Drockenmuller, E. & Hawker, C. J. Fabrication of Densely Packed, Well-ordered, High-aspect-ratio Silicon Nanopillars over Large Areas Using Block Copolymer Lithography. *Thin Solid Films* **2006**, 513, 289-294.

16. Black, C. T., Ruiz, R., Breyta, G., Cheng, J. Y., Colburn, M. C., Guarini, K. W., Kim, H. -C. & Zhang, Y. Polymer Self Assembly in Semiconductor Microelectronics. *IBM J. Res. Dev.* **2007**, 51, 605-633.

17. Guo, L. J. Topical Review: Recent Progress in Nanoimprint Technology and Its Applications *J. Phys. D: Appl. Phys.* **2004**, 37, R123-R141.

18. Pina-Hernandez, C., Kim, J.-S., Guo, L. J. & Fu, P.-F. High-Throughput and Etch-Selective Nanoimprinting and Stamping Based on Fast-Thermal-Curing Poly(dimethylsiloxane)s. *Adv. Mater.* **2007**, 19, 1222-1227.

19. Halls, J. M., Pichler, K., Friend, R. H., Moratti, S. C. & Holmes, A. B. Exciton Diffusion and Dissociation in a Poly(p-phenylenevinylene)/C_{60} Heterojunction Photovoltaic Cell. *Appl. Phys. Lett.* **1996**, 68, 3120.

20. Pettersson, L. A. A., Roman, L. S. & Inganäs, O. Modeling Photocurrent Action Spectra of Photovoltaic Devices Based on Organic Thin Films. *J. Appl. Phys.* **1999**, 86, 487-496.

21. Theander, M., Yartsev, A., Zigmantas, D., Sundström, V., Mammo, W., Anderson, M. R. & Inganäs, O. Photoluminescence Quenching at a Polythiophene/C_{60} Heterojunction. *Phys. Rev. B* **2000**, 61, 12957-12963.

22. Savenije, T. J., Warman, J. M. & Goossens, A. Visible Light Sensitisation of Titanium Dioxide Using a Phenylene Vinylene Polymer. *Chem. Phys. Lett.* **1998**, 287, 148-153.

23. Haugeneder, A., Neges, M., Kallinger, C., Spirkl, W., Lemmer, U., Feldman, J., Scherf, U., Harth, E., Gugel, A. & Mullen, K. Exciton Diffusion and Dissociation in Conjugated Polymer/fullerene Blends and Heterostructures. *Phys. Rev. B* **1999**, 59, 15346-15351.

24. Coakley, K. M. & McGehee, M. D. Conjugated polymer photovoltaic Cells. *Chem. Mater.* **2004**, 16, 4533-4542.

CHAPTER 6

Light Management in Organic Solar Cells Using Plasmonic Nanostructures and Light Trapping Structures

6.1 Introduction

Surface plasmon resonance (SPR) has been exploited in many photonic applications due to their unique capabilities of localizing light at nanoscale dimensions. They are surface waves whose electromagnetic field is confined to the vicinity of the metal dielectric interface. When the condition of the resonance is fulfilled, this confinement leads to an enhancement of the electromagnetic field at the interface and this aspect has been utilized in many nearfield surface plasmon-based applications.[1-3] Among them, their effects on organic solar cells (OSCs) are recently highlighted,[4-6] because those nanostructures potentially provide an effective means to improve the efficiency of OSCs by enhancing the absorption of light even in a very thin organic material layer. Since the thickness of the organic semiconductors in OSCs is about several tens of nanometer, which coincides with the field decay length of SPR in typical dielectric layer, SPR enhancement is naturally suited to increase the optical absorption of the organic semiconductors. Therefore, this approach in principle can address the mismatch problems between the short exciton diffusion length in organic semiconductor materials and the large thickness required to fully absorb sunlight. Though there have been previous reports to demonstrated relative enhancement of the optical absorption by the SPR effect in

OSCs, only limited enhancement of PCE near the resonance wavelength due to the overall transmittance reduction, induced by the additional metal structure, was achieved[4] or non-regular nanoparticles having the difficulties in controlling the dimension and uniformity are introduced in OSCs.[5,6] To make this approach practical, an effective fabrication technique that can produce large-area and uniform metallic nanostructures are needed. In this work, we introduced a nanoimprint lithography (NIL)-based nanofabrication process and their application to OSC devices will be addressed. Furthermore, as another way to enhance the light in the OSC structure, we developed light trapping structures based on hundreds of nanometer scale gratings and their application to OSC devices was also investigated.

6.2 Experimental details

6.2.1 Nanostructured PDMS stamps fabrication

Nanodot and nanograting type PDMS stamps were fabricated using nanohole and nanograting type SiO_2 molds. After treating the substrate by methoxysilane having vinyl groups, a high modulus PDMS solution[32] was dropped on the substrate and subsequently covered by the SiO_2 mold treated by surfactant, (tridecafluoro-1,1,2,2-tetrahydrooctyl) trichlorosilane (GELEST). The PDMS was cured at 120 °C for 5 min under a pressure of 5 psi.

6.2.2 Plasmonic nanoparticles fabrication

Both Ag and Au nanoparticles were fabricated by depositing metals on PDMS nanodot and SiO_2 nanopillar structures with an angle using an electron-beam evaporator

at a rate of 1 Å/s. To transfer the metal nanoparticles to other substrates, the nanostructured SiO_2 stamp, covered by the deposited metal nanoparticles, was pressed onto a polymer layer under 100 °C and 20 psi for 5 min in Nanonex NX2000 nanoimprinter.

6.2.3. Light trapping structure fabrication

Overall process is the same with ESSENCIAL process explained in Chapter 2 except the stamps, which were used in this work. Different with the former ESSENCIAL process, in which flat PDMS was used, the patterned PDMS stamps were used as gas-permeable layer.

6.3 Results and Discussion

6.3.1 Plasmonic nanostructures

In order to fabricate plasmonic nanoparticles, elastomeric stamps based on a combination of hard and soft poly(dimethylsiloxane) (PDMS),[7] which can be used for soft lithography and transparent template applications, were firstly fabricated (Figure 6.1). As shown in Figure 6.1 and 6.2a, large-area soft stamps having dense 20 nm features of dot patterns that can act as transparent templates were successfully fabricated using SiO_2 hole type mold stated in chapter 5. By an angled deposition of metal onto the nanodot structures on the transparent PDMS, high-density sub-20 nm size Ag and Au plasmonic nanostructures were successfully fabricated. Moreover, the position and the peak extinction of the localized surface plasmon resonance (LSPR) of the metal nanoparticles were tunable by changing the thickness of the metal as shown in Figure 6.2d. With

increasing Au thickness, the peak of the localized surface plasmon resonance is red-shifted along with an increase in the magnitude of light extinction.

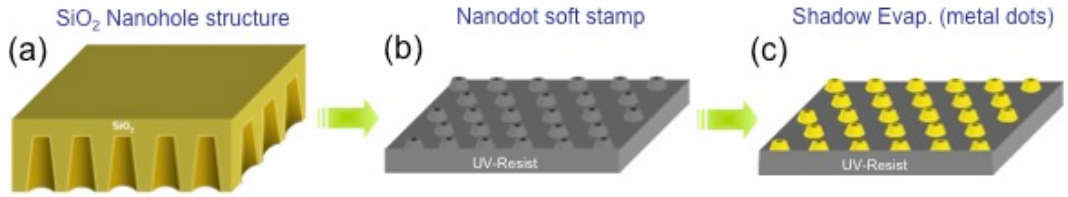

Figure 6.1 Schematic of the process for fabricating plasmonic nanostructures: (a) SiO_2 nanohole type structure; (b) Nanodot soft stamp; (c) Plasmonic metal nanodots.

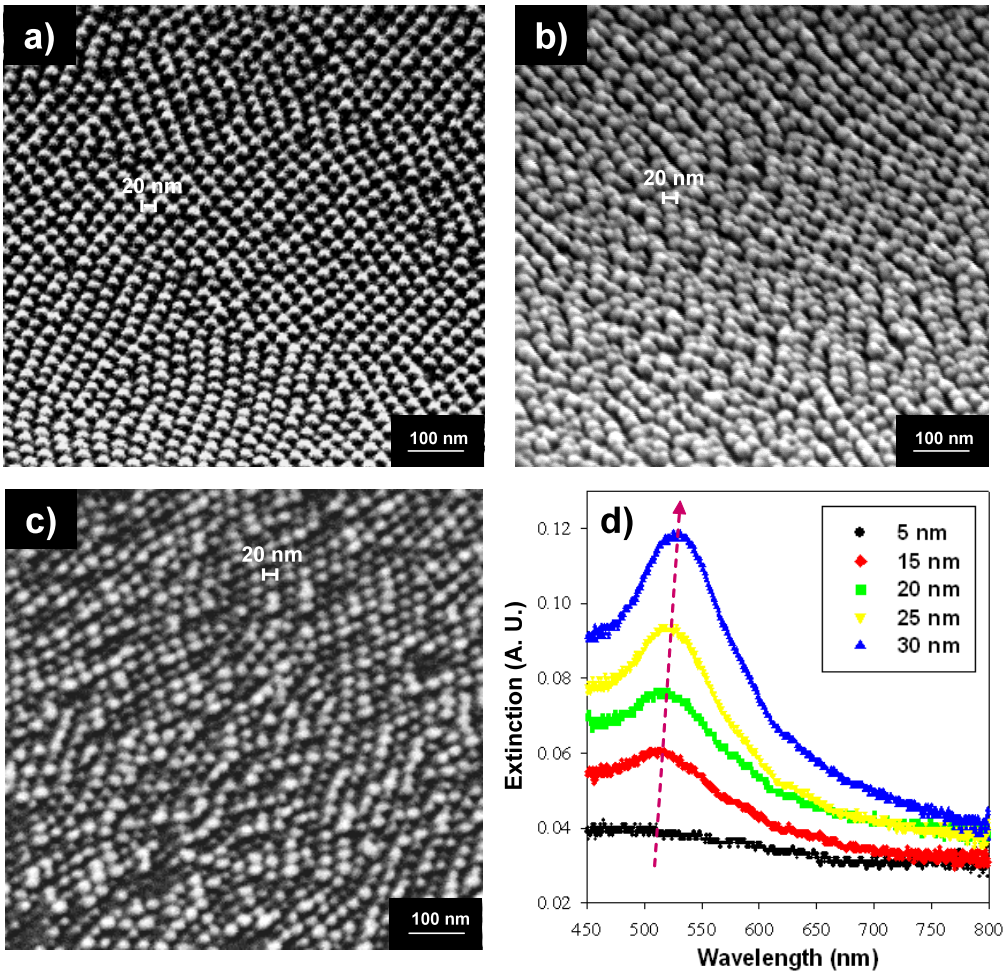

Figure 6.2 SEM micrographs of (a) PDMS nanodots and (b)-(c) plasmonic nanoparticles deposited on nanodot type PDMS stamp by shadow evaporation: (b) Ag; (c) Au; (d) The extinction spectra of the Au plasmonic nanoparticles for different Au thicknesses.

Because metal nanostructures, disconnected each other, showed significantly high sheet resistances (~ 10^5 Ω/sq) even after casting conductive polymer, PEDOT:PSS, on those structures, they can not be directly used as a semi-transparent electrode. Therefore, those nanostructures were introduced on ITO transparent electrode only to be used to enhance the incident light. Metal nanostructures fabricated on soft PDMS stamp or hard SiO_2 mold, treated by fluoro-surfactant, could be efficiently transferred to PEDOT:PSS layer on ITO electrode (Figure 6.3), and they show strong extinction as shown in Figure 6.4. Thin PEDOT:PSS was further casted to restrict direct contact between metal nanoparticles and an active layer, leading to quenching of generated excitions. Overall procedures of the application of the plasmonic nanoparticles to organic solar cells are depicted in Figure 6.5. Using Ag plasmonic particles fabricated on PEDOT:PSS and ITO, polymer bulk heterojunction solar cell was fabricated. P3HT and PBCM are used as donor and acceptor, giving ~ 100 nm active layer thickness, and Al with thin layer LiF was used as cathode. This light enhancement induced by plasmonic resonance gave the increase absorbance, as shown in Figure 6.6a. Consequently, increased power conversion efficiency (from 3.31 to 3.66), originated by improved short circuit current, was obtained (Figure 6.6b).

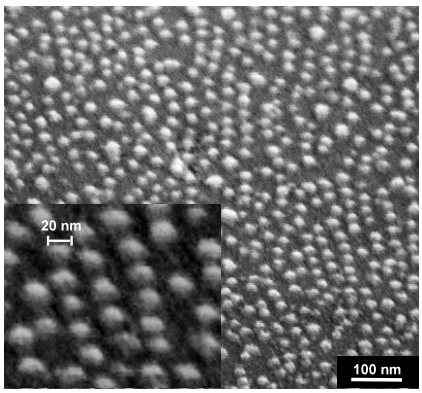

Figure 6.3 SEM micrographs of Au nanoparticles transferred to PEDOT:PSS layer.

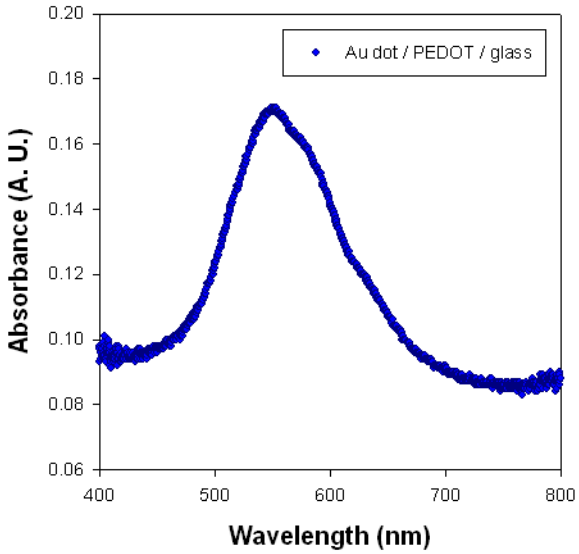

Figure 6.4 The extinction spectra of the Au plasmonic nanoparticles on PEDOT:PSS layer.

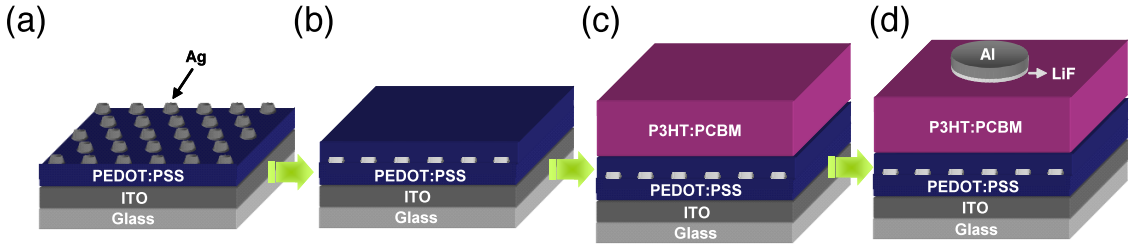

Figure 6.5 Fabrication of polymer solar cell with plasmonic nanoparticles: (a) Transfer of metal nanoparticle to PEDOT:PSS layer; (b) Further PEDOT:PSS layer casting; (c) Active layer formation; (d) Electrode deposition.

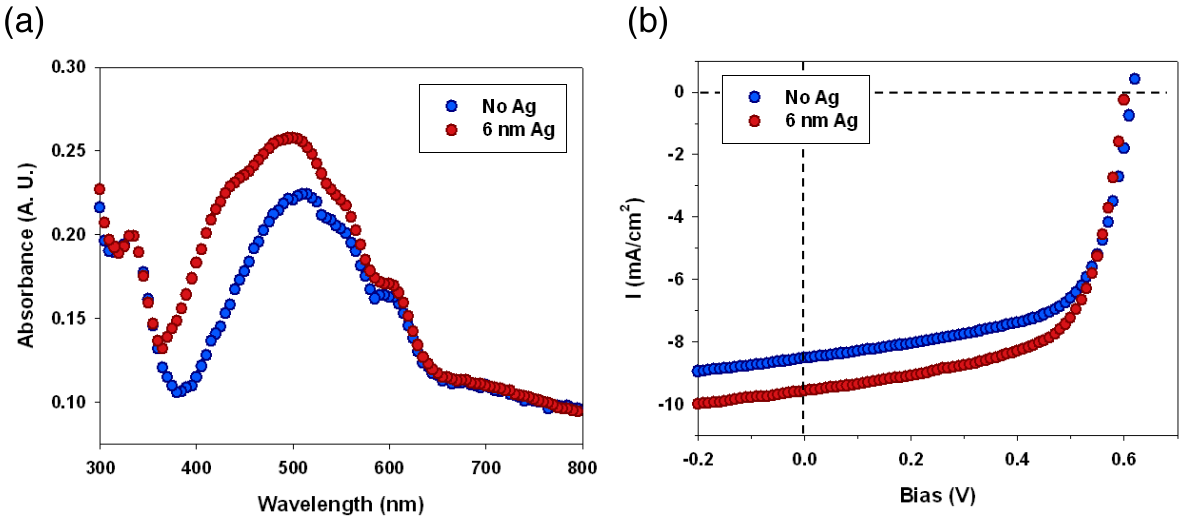

Figure 6.6 (a) Absorption spectra of photoactive layer with and without plasmonic Ag nanoparticles. (b) *J-V* plot of polymer solar cells with and without plasmonic Ag nanoparticles (with Ag: J_{sc} = 9.58 mA cm^{-2}, V_{oc} = 0.60 V, FF = 63.5 %, PCE = 3.66 %, without Ag: J_{sc} = 8.53 mA cm^{-2}, V_{oc} = 0.62 V, FF = 62.6 %, PCE = 3.31 %).

The amount of metal particles, which enhance the absorption of the light, is directly related with the overall transmittance of metal particles-added ITO electrode, and SPR is an evanescent wave that decays exponentially with distance from the metal surface. Therefore, optimizing the amount of metal and the thickness of the device are needed to further enhance the PCE of OSCs. In addition, because the extinction wavelength of plasmonic structure should be well-matched with absorption wavelength of organic active layer to maximize light enhancement effect, controlling the dimension of plasmonic nanostructures to shift extinction wavelength as well as selecting proper organic materials system are also important to high efficiency OSCs.

6.3.2 Light trapping structures

Another type of nanostructure that can be used to enhance the absorption of light is light trapping structures. If we can add periodic nanostructure at the metal electrode working as reflector in OSC, we can enhance the optical path length across a broad wavelength range of incident light. This type of periodic nanostructures can be easily introduced by changing the gas-permeable stamp used in ESSENCIAL process from the flat shape to patterned stamp. After releasing the stamp, nanostructures are easily introduced and further metal deposition for electrode complete the light trapping structure.

Figure 6.6 shows the calculated enhancement of absorption after introducing the light trapping structure and the experimental results are demonstrated in Figure 6.7. The designed structure is 700 nm period metal nanograting having 350 nm line width.

According to the calculation, the absorption enhancement in P3HT:PCBM system with those nanostructures is over 2.5 and this enhancement of light is expected to increase the short-circuit current (J_{sc}) without changing other factors. As expected, the real device fabricated using this structure showed the increased J_{sc} from 8.84 to 10.85 $mAcm^{-2}$. Consequently, the PCE was improved from 3.36 to 4.16. This type of nanograting structure also can be easily applicable to another high performance materials. Further optimization of structure and analysis are still under investigation.

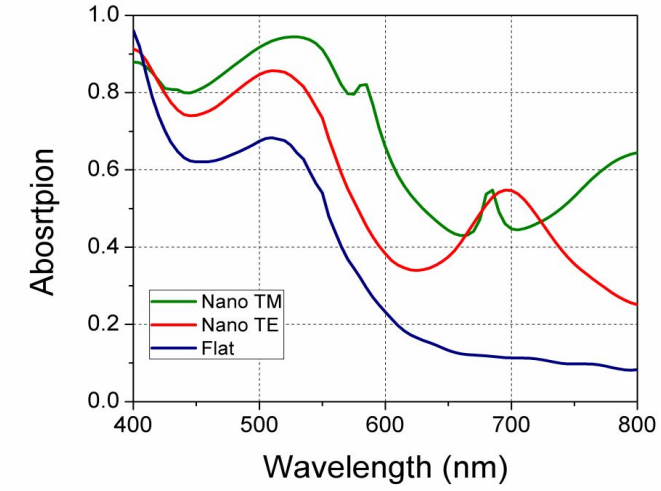

Figure 6.7 Calculated absorption of light with and without light trapping structure. TE and TM waves mean transverse electric and transverse magnetic waves, respectively. The polarized light having the E-field parallel to the nanograting direction is defined as TE and the polarized light having E-field perpendicular to the nanograting direction is defined as TM.

Table 6.1 Summarized absorption enhancement with light trapping structure (calculation results).

Period	TM	TE	Average
700 nm	3.08	2.34	2.71

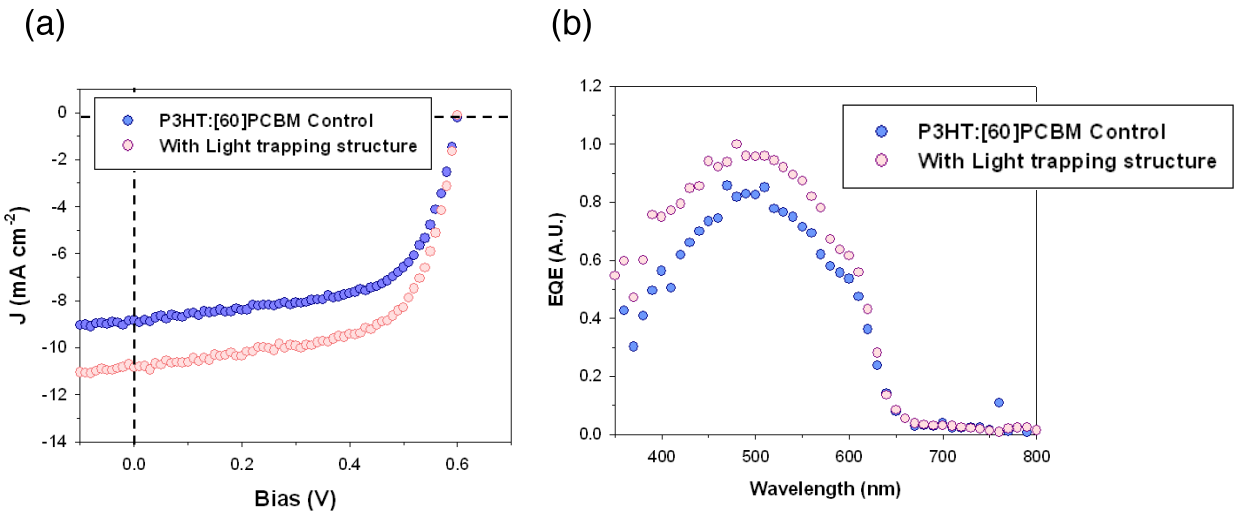

Figure 6.8 The device performance of P3HT:PCBM system OSC devices with (pink color circle) and without (violet color circle) light trapping structures: (a) *J-V* plots; (b) External quantum efficiency.

Table 6.2 Summarized device performances with and without light trapping structure.

Method	J_{sc} [mA cm^{-2}]	V_{oc} (V)	*FF* (%)	PCE (%)
BHJ (Thermal annealed)	8.84	0.60	63.24	3.36
BHJ with light trapping structures	10.85	0.60	63.75	4.16

6.4 Conclusion

By introducing nanostructure such as plasmonic nanostructure and light tapping structure into OSC devices, we could enhance the absorption of light even in thin active layer (~100 nm), ultimately giving higher PCE of solar cells.

6.5 References

1. Luo, X. & Ishihara, T. Surface plasmon resonant interference nanolithography technique. *Appl. Phys. Lett.* **2004**, 84, 4780.

2. Fang, N., Lee, H., Sun, C. & Zhang, X. Sub-diffraction-limited optical imaging with a silver superlens. *Science* **2005**, 308, 534.

3. Albrecht, M. G. & Creighton, J. A. Anomalously intense raman spectra of pyridine at a silver electrode. *J. Am. Chem. Soc.* **1977**, 99, 5215.

4. Reilly III, T. H., van de Lagemaat, J., Tenent, R. C., Morfa, A. J. & Rowlen, K. L. Surface plasmon enhanced transparent electrodes in organic photovoltaics. *Appl. Phys. Lett.* **2008**, 92, 243304.

5. Morfa, A. J., Rowlen, K. L., III, T. H. R., Romero, M. J. & van de Lagemaat, J. Plasmon enhanced solar energy conversion in organic bulk heterojunction photovoltaics. *Appl. Phys. Lett.* **2008**, 92, 013504.

6. Kim, S.-S., Na, S.-I., Jo, J., Kim, D.-Y. & Nah, Y.-C. Plasmon enhanced performance of organic solar cells using electrodeposited Ag nanoparticles. *Appl. Phys. Lett.* **2008**, 93, 073307.

7. Pina-Hernandez, C., Kim, J.-S., Guo, L. J. & Fu, P.-F. High-throughput and etch-selective nanoimprinting and stamping based on fast-thermal-curing poly(dimethylsiloxane)s. *Adv. Mater.* **2007**, 19, 1222-1227.

CHAPTER 7

Photonic Color Filters Integrated with Organic Solar Cells for Energy Harvesting

7.1 Introduction

Energy efficiency is becoming ever more important for a green and sustainable future. As global energy demand continues to grow to meet the needs and aspirations of people across the world, ways to improve energy efficiency and harvest energy are essential. Recently, a number of approaches have been explored to scavenge energy from environments, such as photovoltaic (PV),[1] thermoelectric,[2] and piezoelectric effects.[3] However, little attention has been paid to the significant light energy wasted in displays used in our everyday lives. For example, in the prevailing liquid crystal displays (LCD), only 3-8 % of the backlight can reaches our eyes, where most of light energy is absorbed by the colorant-based filters and polarizers.[4] Therefore, approaches that can recycle or harvest the absorbed energy to generate useful electrical power could lead to revolutionary energy-saving e-media. This aspect is especially promising when considering the widely used devices such as e-book that consumes little power, or mobile devices (such as cell phones) that are in standby mode 95 % of the time. In this paper, we exploit a dual-function photovoltaic-color filter device that can produce desirable reflection colors and simultaneously convert the absorbed light to electricity. Such dual-

functionality can also be exploited to make colored OPV panels for both decoration and light energy harvesting.

The control of light interaction with nanostructures and their unique applications in photonics have been highlighted in the past decade with the development of nanofabrication and characterization techniques for light management.[5-9] Optical resonance effects in nanoholes,[10,11] nanoslits[12-14] and related nanostructures[15-18] have been exploited for color filter applications. Here we will use organic semiconductors as an integral part of a specially designed photonic color filter for energy conversion. As a proof of principle, we will demonstrate a reflectance type color filtering device capable of power generation. Reflective colors are superior to transmissive filter technologies[10-14] for outdoor usage, and can work under direct sunlight for more energy absorption and energy conversion using the scheme discussed in this paper. Our conceptual devices are to recycle the wasted energy in most of display applications that require color filters to achieve desirable colors; and do not apply to colored displays using emissive devices such as organic light-emitting diode (OLED). Furthermore, we adopt organic photovoltaic (OPV) cell structure to our dual-function devices. Therefore, the approach also takes the advantages of the OPV, such as low cost, easy fabrication, and compatibility with flexible substrates over a large area.[19-24] In addition, this work points out alternative applications of OPVs, which complements the great efforts in improving its power conversion efficiency (PCE)[20-22] and practical fabrication methods.[21,24]

7.2 Experimental details

7.2.1 Au nanograting fabrication

Three types of Au nanogratings having 0.7 duty cycle with different periods (420 nm, 280 nm, and 220 nm) were fabricated by the same processes based on conventional nanoimprint lithography (NIL) and shadow evaporation technique. Using SiO_2 mold having 0.5 duty cycle, the narrow line-width SiO_2 mold having 0.3 duty cycle was firstly fabricated as shown in Figure 7.1.

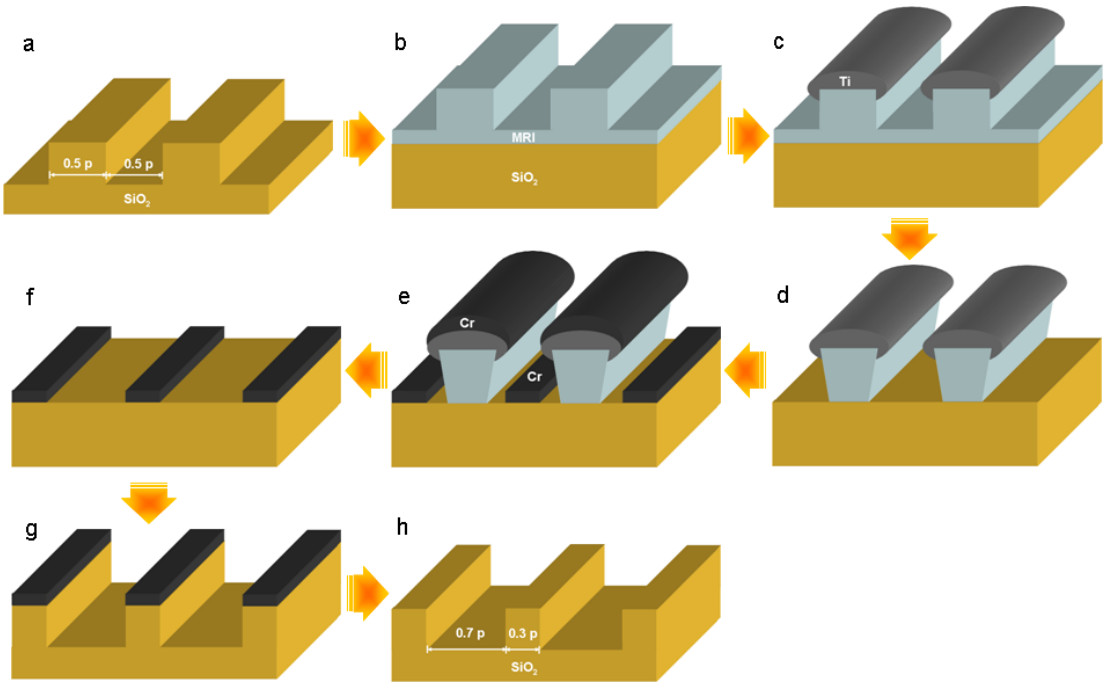

Figure 7.1. Schematic diagram of the fabrication of narrow line-width SiO_2 mold: (a) SiO_2 mold having 0.5 duty cycle; (b) NIL on resist; (c) Angled deposition of Ti to control the line-width; (d) O_2 RIE to etch the residual layer; (e) Cr deposition; (f) Lift-off; (g) SiO_2 etching by RIE; (h) Cr wet-etching.

NIL was performed in Nanonex NX2000 naonoimprinter (Princeton, NJ) using a SiO_2 mold with 0.5 duty cycle on a MRI-8030 resist (Microresist Technology GmbH) spin-

casted on SiO_2 substrates, at a pressure of 600 psi and a temperature of 180 °C for 5 min. After cooling and demolding, Ti was selectively deposited on each sidewall of the imprinted grating structures by angled deposition. The line-width of resultant SiO_2 mold is determined by the amount of Ti deposited on the sidewall. O_2 reactive ion etching (RIE) (20 sccm O_2, 12 mTorr chamber pressure, and 30 W bias power), deposition of 15 nm thick Cr using electron beam evaporation and lift-off give the narrow line-width Cr gratings. Finally Cr nanogratings were used as mask to etch the SiO_2 by RIE (50 sccm C_2F_6 / 50 sccm He / 60 sccm Ar / 10 sccm O_2, 60 mTorr chamber pressure, and 50 W bias power).

As a next step, the narrow line-width SiO_2 mold having 0.3 duty cycle was used to fabricated the wide line-width SiO_2 mold having 0.7 duty cycle, as shown in Figure 7.2.

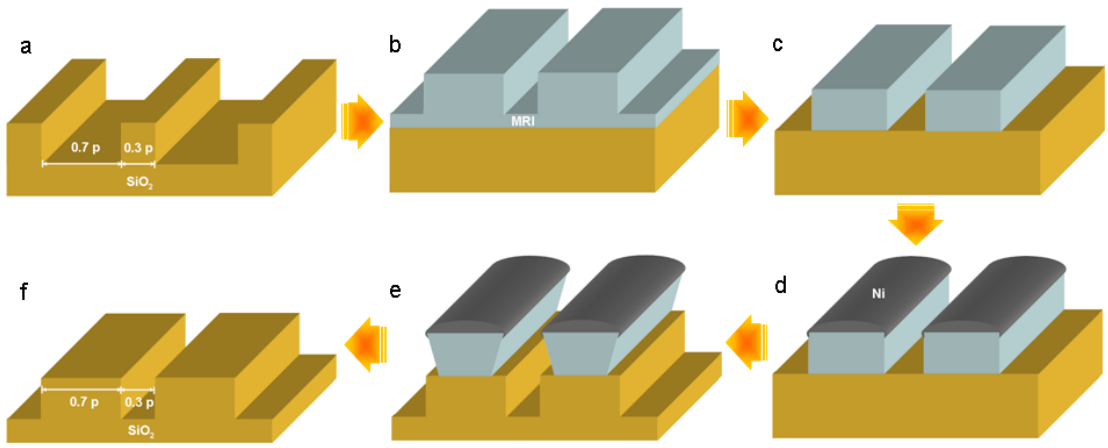

Figure 7.2 Schematic diagram of the fabrication of wide line-width SiO_2 mold: (a) SiO_2 mold having 0.3 duty cycle; (b) NIL on resist; (c) O_2 RIE to etch the residual layer; (d) Angled deposition of Ni to reinforce the polymer resist mask; (e) SiO_2 etching by RIE using Ni as a mask; (f) Elimination of etching mask.

After NIL by SiO_2 mold with 0.3 duty cycle on a resist, O_2 RIE was performed to eliminate the residual layer. In addition, the Ni was selectively deposited on resist to reinforce the nanograting patterns that will be used as etching masks of SiO_2 layer. Ni was selected as an etching mask due to its resistance to the RIE chemistry for SiO_2 etching. By etching SiO_2 layer using Ni-reinforced polymer patterns as a mask, wide line-width SiO_2 stamps were fabricated. Figure 7.3 shows the SEM images of the SiO_2 molds with narrow and wide line-width as references.

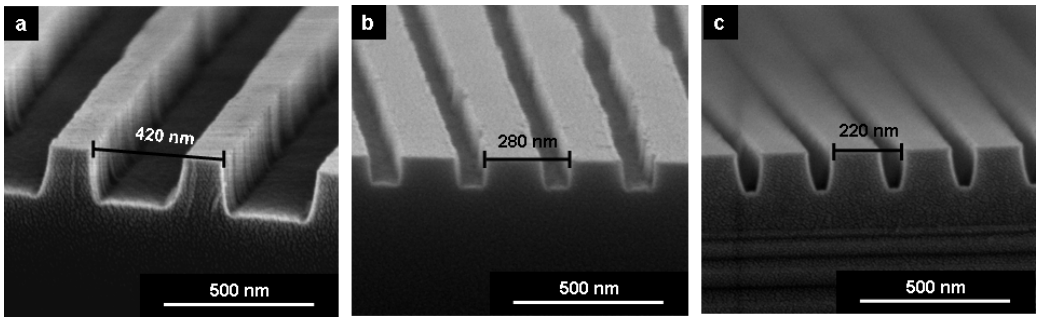

Figure 7.3 SEM images of (a) the narrow line-width SiO_2 mold with a period of 420 nm, (b) the wide line-width SiO_2 mold with a period of 280 nm, and (c) the wide line-width SiO_2 mold with a period of 220 nm.

Finally, the wide line-width SiO_2 mold having 0.7 duty cycle gave the wide line-width Au nanogratings having 0.7 duty cycle as depicted in Figure 7.4.

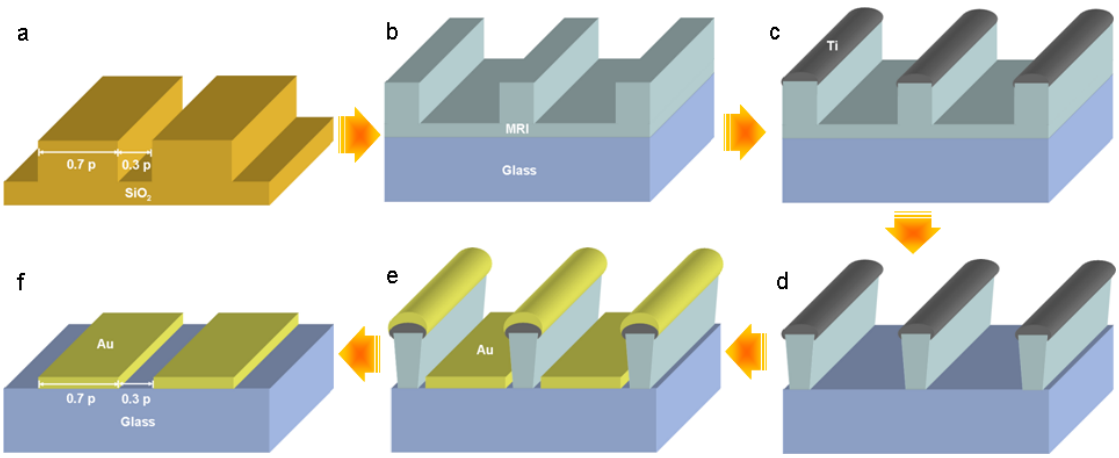

Figure 7.4 Schematic diagram of the fabrication of wide line-width Au nanogratings: (a) SiO_2 mold having 0.7 duty cycle; (b) NIL on resist; (c) Angled deposition of Ti to make undercut structures; (d) O_2 RIE to etch the residual layer. This step gives the undercut structure facilitating the lift-off process; (e) Au Deposition; (f) The lift-off process giving Au nanogratings.

After performing NIL on the resist using wide line-width mold having 0.7 duty cycle, Ti was selectively deposited on the nanograting resist. Ti deposited on the resist patterns induces the undercut structures during O_2 RIE, facilitating the lift-off process. After deposition of 40 nm Au with 1 nm Ti, the lift-off process completed the fabrication of Au nanograting structures on a glass substrate.

7.2.2 Dual-function device fabrication

Au nanogratings on glass were cleaned in acetone and isopropyl alcohol (IPA) under sonication for 20 min, respectively, and treated by O_2 plasma for 60 s. Cleaned substrates were then transferred to a N_2 purged glove box and the filtered PEDOT:PSS (H.C. Starck, Clevios PH 500) was spin-casted onto the Au nanograting electrodes to deposit ~ 30 nm thick layer which was subsequently baked at 115 °C for 15 min. For the photoactive layer, P3HT (Rieke Metals Inc., 4002-E, ~ 91 % regioregularity) and PCBM (American Dye Source, Purity: > 99.5 %) were used as received, and blend solutions were prepared by dissolving both components in chlorobenzene with 1:1 ratio by weight. The solution was stirred for ~ 12 h in the N_2 purged glove box to give homogeneous blend system and filtered using a 0.45 μm filter. The blend solution was spin-casted onto the PEDOT:PSS layer, and annealed at 130 °C for 20 min. The thickness of the blend film was controlled by changing the concentration of solution and the spin-coating speed. The thickness of organic layer was measured by Dektek profiler. After thermal treatment, LiF (1 nm) and

Al (75 nm) were deposited by thermal evaporator at pressure of 8×10^{-7} mbar through the circular-shaped shadow masks.

7.2.3 Solar cell performance measurements

Current versus voltage characteristics were measured with Keithley 2400 system by illuminating the OPV cells with AM 1.5 G simulated sun light using Oriel Solar Simulator with a irradiation intensity of 100 mW cm^{-2}, which was calibrated by power meter (OPHIR, Nova-Oriel) and a reference silicon solar cell.

7.3 Results and discussion

Since the reflectance type color filters act similarly to the color paint, i.e. absorbing light corresponding to specific wavelengths but reflecting the others, here we focus on the CMY color scheme where cyan, magenta and yellow are three primary colors. Figure 5a-c present the schematic diagram of the proposed energy-harvesting color filters, where the conjugated polymer layers composed of poly(3,4-ethylenedioxythiophene): poly(styrenesulfonate) (PEDOT:PSS) and poly(3-hexylthiophene):[6,6]-phenyl C_{61} butyric acid methyl ester (P3HT:PCBM) blend are sandwiched by an Au nanograting layer and a continuous thick Al film. The selection of each material and its role will be further explained later. Large area metallic nanostructures can be applicable to semi-transparent electrode for organic optoelectronics by controlling their optical transparency and electrical conductivity.[25] Accordingly, the key concept in our design is that the periodic Au nanogratings in the device act not only as nanostructures to modulate the

incident light to generate different colors, but also as semi-transparent anode for the OPV cells. In this structure the low work function Al film acts as cathode.

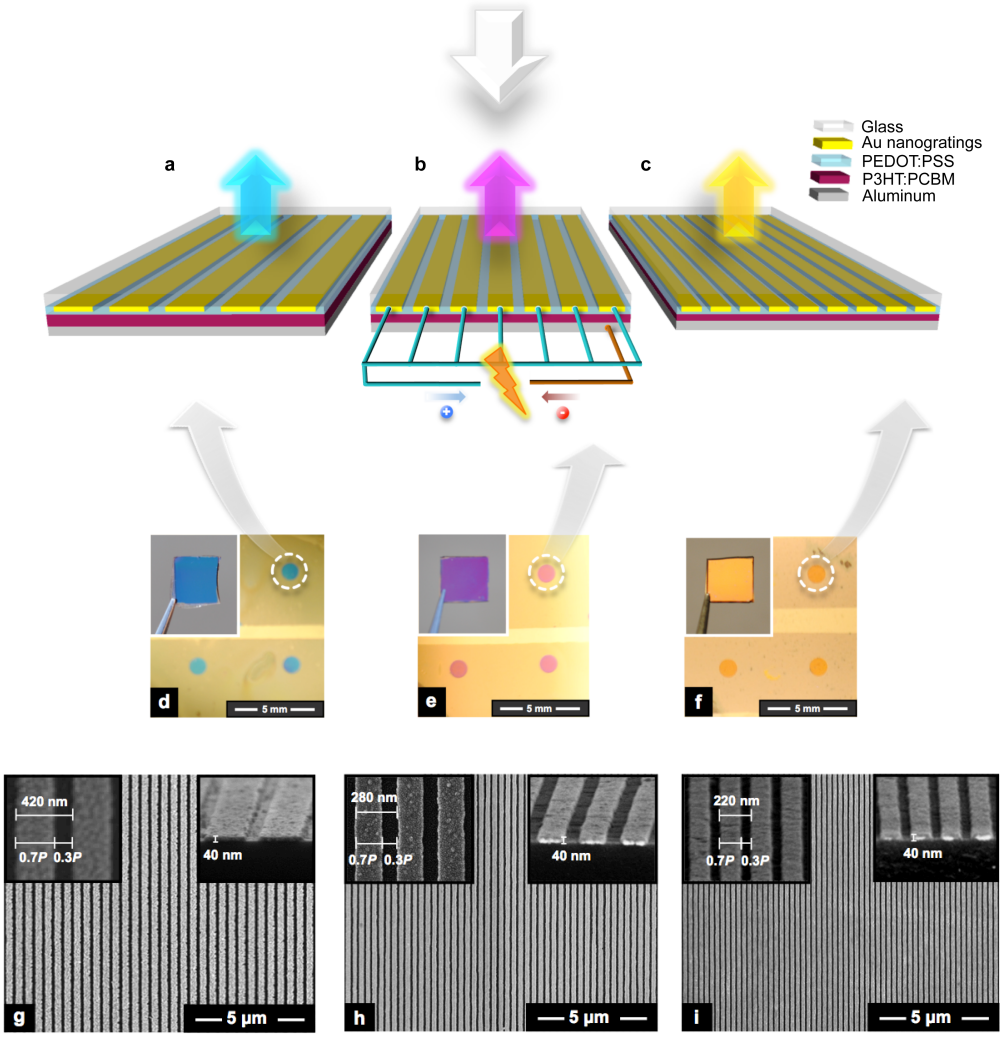

Figure 7.5 Energy-generating photonic color filters. (a)-(c) Schematic of dual-function devices. In all three cases, the thickness of Au nanogratings and PEDOT:PSS layer are 40 nm and 30 nm respectively. Au nanogratings have 0.7 duty cycle (Au linewidth is 0.7 of the period). The photovoltaic property is schematically described in (b) as a representative: (a) Cyan colored device having 420 nm period Au nanogratings and 90 nm thickness P3HT:PCBM photoactive layer; (b) Magenta colored device having 280 nm period Au nanogratings and 65 nm thickness photoactive layer; (c) Yellow colored device having 220 nm period Au nanogratings and 50 nm thickness photoactive layer. (d)-(f) Photographs of dual-function devices having 1 mm diameter circular shape. The inset images are the large area version having about 1 cm size: (d) Cyan; (e) Magenta; (f) Yellow. (g)-(i) Scanning electron microscope (SEM) images of Au nanogratings. The left and right inset images are the high magnification top and tilted views, respectively. The *P* in the left inset image represents the period of Au nanogratings: (g) 420 nm period; (h) 280 nm period; (i) 220 nm period.

Color filters are desired to be polarization insensitive to the natural incident light. To achieve this, we used different design strategies for the transverse electric (TE) and transverse magnetic (TM) waves so that similar reflection spectra for both polarizations can be obtained for each color. First of all, the structure resembles a Fabry-Pérot cavity. When the light impinges on the Au nanogratings, it will interfere with the waves reflected from the bottom Al film. When destructive interference occurs, the reflection spectra will reach a minimum, and the light energy of the corresponding color will be absorbed and complimentary color reflected by the structure. Figure 7.6a and b show the calculated reflection spectra maps for TE polarized light (the E-field is parallel to the Au nanograting direction) as a function of P3HT:PCBM blend layer thickness (Figure 7.6a, Au grating period fixed at 280 nm) and as a function of Au nanograting period (Figure 7.6b, blend layer thickness fixed at 50 nm), respectively. The blue regions in these maps represent the reflection minima where the light energy is absorbed by the structure. As expected from the Fabry-Pérot interference, the resonant absorption wavelength is linearly proportional to thickness of blend layer but almost independent of the nanograting period. For TM waves (the E-field is perpendicular to the Au nanograting direction), additional consideration needs to be taken, as it is well known that TM waves can be efficiently coupled to the plasmon modes through the subwavelength grating structures.[7,8] Figure 6c gives the calculated map of reflection spectrum for TM polarized waves as a function of Au nanograting period. Here the P3HT:PCBM blend layer thickness remains 50 nm. In addition to the absorption band produced by the Fabry-Pérot inteference, there are two more resonant absorption stripes (marked with white dashed lines) that originate from the splitting of SP modes in the plasmonic waveguide

structures.[26,27] The dispersion characteristics of these modes show strong dependence on the Au nanograting period because it provides the phase matching condition for the TM polarized light to couple to the SP mode. We can take the advantage of the insensitivity of Fabry-Pérot resonance to the Au nanograting period and choose a particular period so that the TM polarized light is absorbed around the same wavelength as the TE polarized light, thereby producing polarization independent reflection colors. Figure 6d shows the simulated magnetic field intensity for TM and TE waves at the same resonant absorption wavelength of 490 nm. The thickness of P3HT:PCBM blend layer and the periodicity of Au nanogratings are 50 nm and 220 nm, respectively. It can be clearly seen that the field distribution for TM polarization exhibits obvious plasmon behaviors at the Au-PEDOT:PSS and Al-P3HT:PCBM interfaces. For the TE polarization, the field distribution resembles that of conventional Fabry-Pérot interference, further supporting our design principle.

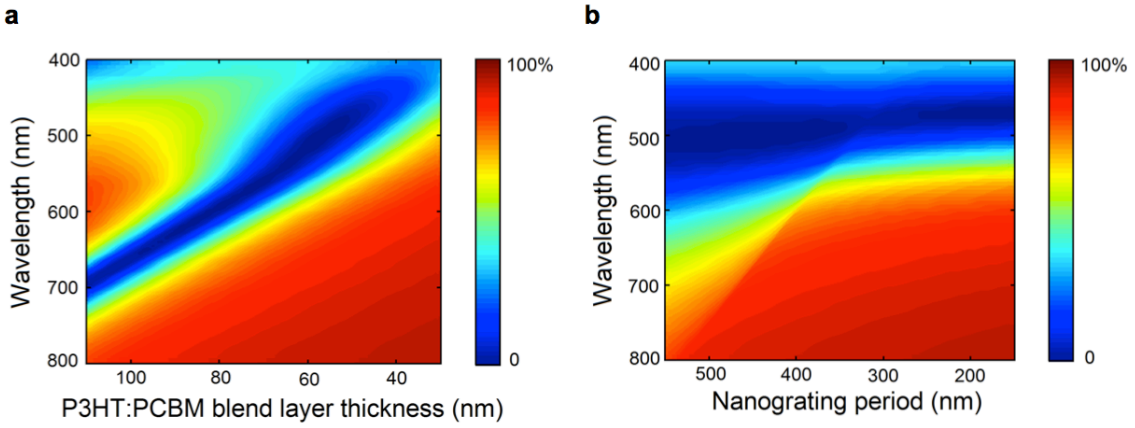

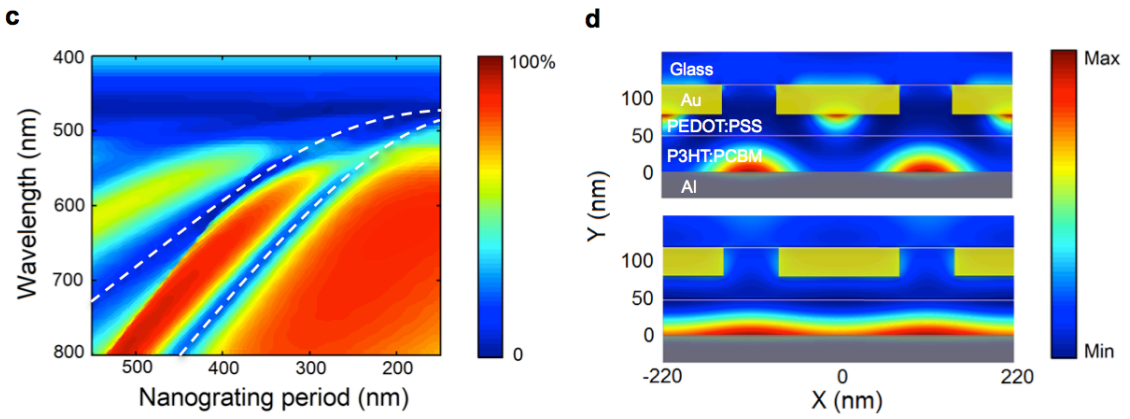

Figure 7.6 Calculated maps of the reflection for the proposed structures. The thickness of Au nanogratings and PEDOT:PSS layer are fixed at 40 nm and 30 nm, respectively. Au nanogratings have 0.7 duty cycle. (a)-(b) Reflection for TE polarized waves as a function of (a) the thickness of P3HT:PCBM blend photoactive layer (Au nanograting period is fixed at 280 nm) and (b) Au nanograting period (the thickness of photoactive layer is fixed at 50 nm). (c) Reflection for TM polarized waves as a function of Au nanograting period (the thickness of photoactive layer is fixed at 50 nm). (d) Magnetic field intensity distribution for TM (top) and TE (bottom) waves at the same resonant absorption wavelength of 490 nm. The thickness of photoactive layer and the period of Au nanogratings are 50 nm and 220 nm, respectively.

Figure 7.5g-i shows the scanning electron microscope (SEM) images of the fabricated Au nanogratings. Here Au was chosen due to its excellent conductivity and appropriate work function as an anode. The periodic Au nanograting structures were fabricated using nanoimprint lithography (NIL), followed by a reactive ion etching (RIE), metal deposition and lift-off process, to produce large area transparent electrode onto which OPV cells can be easily fabricated. The fabrication of the complete OPV structures using those Au nanogratings as an anode is as follows. Firstly, conductive PEDOT:PSS layer, often used in OPV structures as hole transporting layer and with the high work function for holes collecting, was casted on the Au nanograting anode. Such "composite" anode structures consisting of metallic nanogratings and PEDOT:PSS can ensure efficient hole collection and transport between the metal lines. Next, high performance bulk heterojunction (BHJ)[19-24,28] photoactive layer composed of P3HT and PCBM was

constructed, serving the function to convert the absorbed light to photocurrent. After thermal annealing to optimize the BHJ nanostructures, a continuous Al cathode layer was thermally deposited. Al was selected due to its excellent performance as a cathode material for the OPV cells when combined with a thin LiF layer and cost-effectiveness.[21,29] An ultrathin 1 nm LiF was used to improve the performance of OPV cells but did not affect the optical properties of the device. The Al layer also prohibits the direct transmission of the incident light.

Following the design guidelines and the fabrication processes described above, we demonstrate primary CMY colors (cyan, magenta and yellow) under natural light conditions. First, BHJ active layers of three thicknesses (90 nm, 65 nm and 50 nm) were selected to control the TE polarized light to generate CMY colors, respectively. Then Au nanogratings of three corresponding periods (420 nm, 280 nm and 220 nm) were selected to control the TM polarized light under the given photoactive layer thickness. In all three cases, the thicknesses of the Au nanogratings and the PEDOT:PSS layer are 40 nm and 30 nm, respectively. All the Au nanogratings have about 0.7 duty cycle (Au linewidth is 0.7 of the period). The light is illuminated onto the color filter from the Au anode side and the photograph images were taken showing distinct reflected CMY colors over large areas (Figure 5d-f). Figure 7.7 shows the reflection spectra of the CMY colors of the proposed structure: simulation results by rigorous coupled wave analysis (RCWA) method (upper panel), and experimental results measured by using a broadband white light source (lower panel). Clearly the expected color filtering behavior was obtained, and the experimentally measured spectra are well-matched with the simulation results calculated for both polarized and unpolarized light conditions. The angle dependence of

reflective filters was also tested by calculating the color variations for the CMY color in the CIE 1931 color space chromaticity diagram with increasing the incident angle (Figure 7.8). Experimental spectrum was further examined by changing the viewing angle between the light source and detector using spectroscopic ellipsometer (from 0° to 60°, Figure 7.9). Both results demonstrated that the color variation is not so dramatic and acceptable in some range (< 30°).

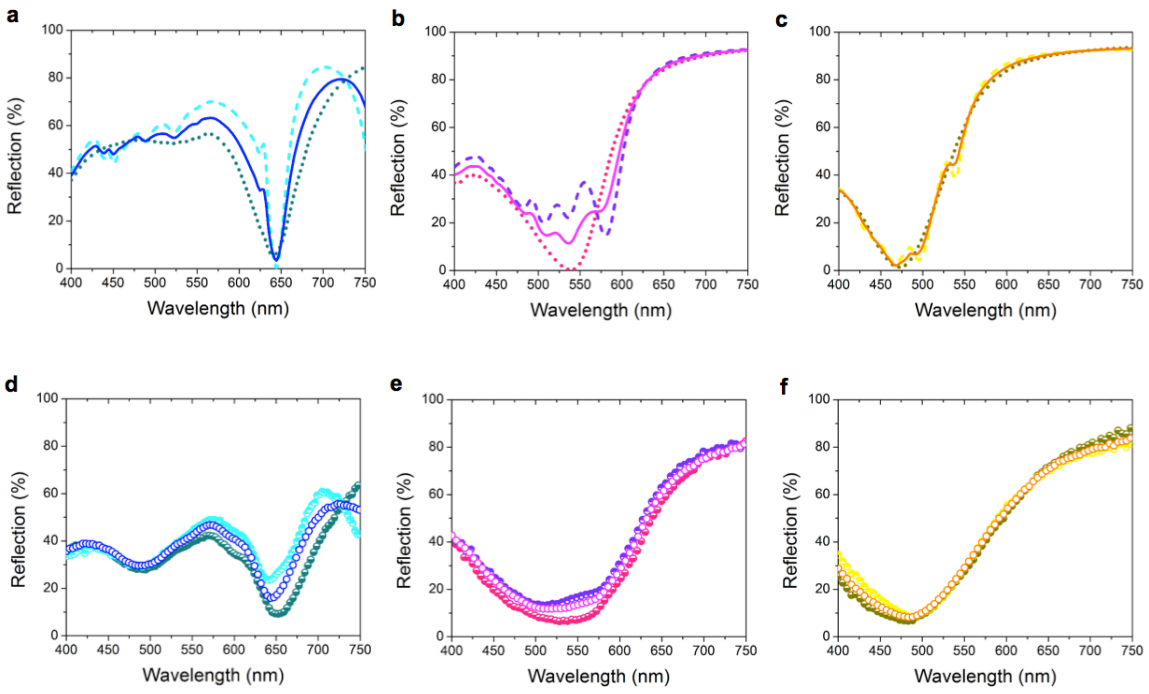

Figure 7.7 Color filtering behaviors in dual-function devices. (a)-(c) The reflection spectra calculated by RCWA simulation. Solid line, dashed line, and dotted line represent unpolarized condition, TM mode, and TE mode, respectively: (a) Cyan; (b) Magenta; (c) Yellow. (d)-(f) Measured reflection spectra. Open circle, half-down open circle, and half-up open circle represent unpolarized condition, TM mode, and TE mode, respectively: (d) Cyan; (e) Magenta; (f) Yellow.

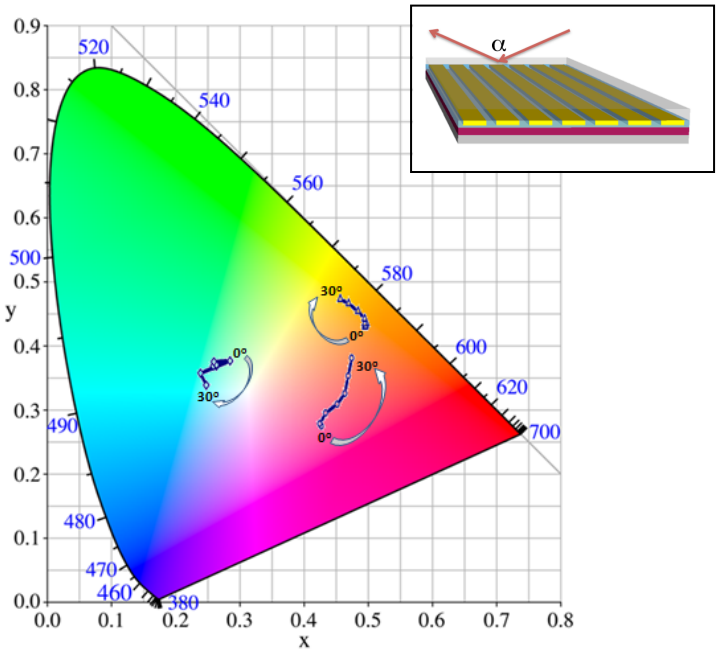

Figure 7.8 Simulated Color variations for the CMY color in the CIE 1931 color space chromaticity diagram with increasing the incident angle (α). Inset image depicts the direction of incident light.

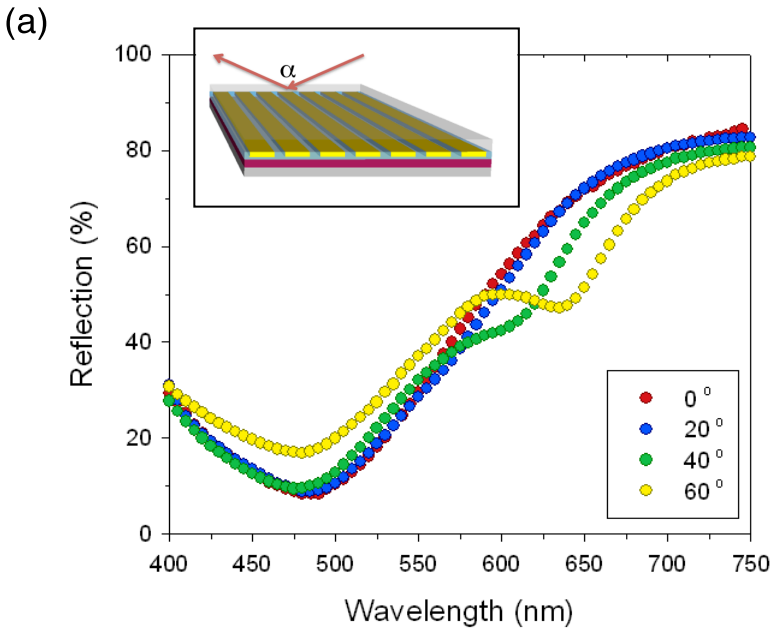

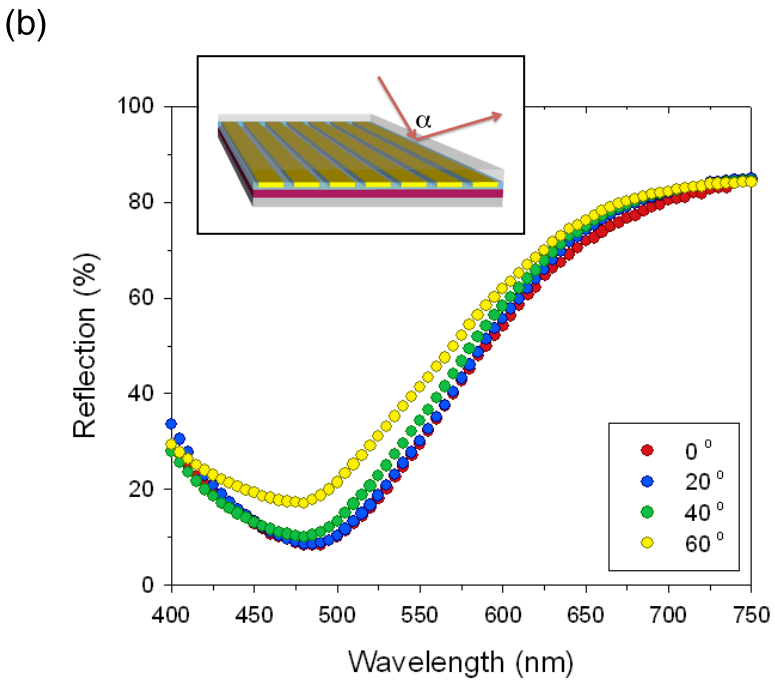

Figure 7.9 Reflection spectrum of yellow-colored filter measured by spectroscopic ellipsometer according to the incident angle (α). The direction of light is perpendicular (a) and parallel (b) to the metal nanogratings. Inset images depict the direction of incident light.

Finally photovoltaic properties of the reflective color filter devices were measured under AM 1.5 G simulated sun light (at 100 mW cm^{-2} intensity) and the current density versus voltage characteristics are summarized in Figure 7.10. The measured PCEs for the CMY color filters are 1.55 %, 0.82 %, and 0.60 %, respectively. The cyan colored devices with the thickest photoactive layer (~ 90 nm), leading to sufficient light absorption in this structure, showed the best efficiency with the highest short circuit current density (J_{sc}) and fill factor. The magenta colored devices having well-matched absorption near the maximum energy band of electron-donor materials P3HT, usually centered around 550 nm,[20,21,30] have the comparable J_{sc} with the cyan colored even with the thinner photoactive layer (~ 65 nm). The yellow colored filters also successfully generated electrical power as OPV cells, even though they have the reduced absorption

around the energy band of electron-donor with the thinnest photoactive layer (~ 50 nm) giving the lowest J_{sc}. Furthermore, we would like to point out that in our design because the metallic nanogratings simultaneously serve as the semi-transparent electrode for the solar cell, the use of wider metal lines (0.7 duty cycle) is highly desirable because they will significantly reduce the resistance of the electrode, which is essential for large area solar cells without degrading the PCE. As an example, current OPV cells built on ITO still suffer from the insufficient conductance of the transparent ITO when they are made large area due to the voltage drop on the resistive electrode.[31] Moreover, the superior flexibility of metallic nanostructures on the flexible substrate without conductance degradation under bent condition[32] and the applicability to large area roll-to-roll processing[21,32] make these dual-function devices appealing to large area flexible display applications.

As an alternative structure for reflective color filter, the continuous flat metal film can be also employed rather than metal nanogratings. In this scheme, the whole structure acts as a simple planar Fabry-Pérot cavity and the color filtering can be realized by the Fabry-Pérot interference effect. For the normal incidence, the TE and TM illuminations within the planar Fabry-Pérot cavity are theoretically indistinguishable and the resonant wavelength is similar to the TE component within the nanograting device. However, the devices composed of continuous flat metal films instead of nanograting structures suffer from significantly low optical transmission through the continuous metal film inducing negligible photocurrent. Furthermore, most of devices tend to have almost short circuit behavior, which are still under investigation.

Another interesting aspect of our design is that the longitudinal thickness of the this photonic color filter is less than 200nm, which is about 2 orders of magnitude thinner than that of traditional colorant based ones. This is very attractive for the design of ultrathin colored devices.

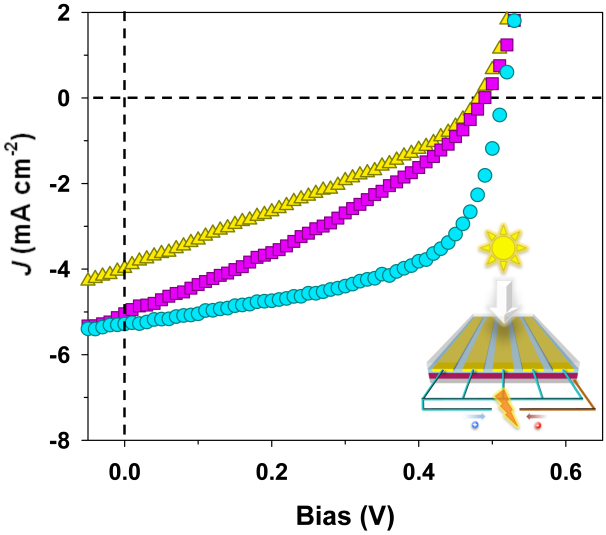

Figure 7.10 Photovoltaic behaviors in dual-function devices. Circle, square, and triangle symbols represent the devices showing cyan, magenta and yellow colors, respectively. *J–V* plots of dual-function devices. All data were measured at AM 1.5 G with an intensity of 100 mW cm^{-2}. Average solar cell characteristics such as short circuit current density (J_{sc}), open circuit voltage (V_{oc}), fill factor (FF) and power conversion efficiency (PCE) are summarized as follows: cyan (J_{sc} = 5.28 mA cm^{-2}, V_{oc} = 0.51 V, FF = 57.5 %, PCE = 1.55 %); magenta (J_{sc} = 5.04 mA cm^{-2}, V_{oc} = 0.49 V, FF = 33.1 %, PCE = 0.82 %); yellow (J_{sc} = 3.98 mA cm^{-2}, V_{oc} = 0.48 V, FF = 31.2 %, PCE = 0.60 %). The inset image is a schematic of dual-function device showing photovoltaic property.

7.4 Conclusion

In summary, we demonstrated reflective color filtering elements that simultaneously integrate the OPV function into a single device. The absorbed light by the color filter, which are otherwise totally wasted, are harvested by the OPV to generate photocurrents.

The dual-function devices, which are expected to lead to higher efficiency, are currently under investigation according to the design principles suggested in this paper. Considering the scalability of OPV devices to large areas, the unique energy-generating property of the dual-functional color filters may lead to more energy-efficient e-media. The dual-functionality can find another attractive application, where decorative colored OPV panels can be envisioned for light energy conversions.

7.5 References

1. Morton, O. Solar energy: a new day dawning?: silicon valley sunrise. *Nature* **443**, 19–22 (2006).
2. Snyder, G. J. & Toberer, E. S. Complex thermoelectric materials. *Nature Mater.* **7**, 105–114 (2008).
3. Cha, S. N., Seo, J.-S., Kim, S. M., Kim, H. J., Park, Y. J., Kim, S.-W. & Kim, J. M. Sound-driven piezoelectric nanowire-based nanogenerators. *Adv. Mater.* **22**, 4726–4730 (2010).
4. Harbers, G., Bierhuizen, S. J. & Krames, M. R. Performance of high power light emitting diodes in display illumination applications. *J. Display Tech.* **3**, 98–109 (2007).
5. Joannopoulos, J. D., Villeneuve, P. R. & Fan, S. Photonic crystal. *Solid State Commun.* **102**, 165–173 (1997).
6. Joannopoulos, J. D., Johnson, S. G., Winn, J. N. & Meade, R. D. Photonic Crystals: Molding the Flow of Light, Second Edition (Princeton University Press, 2008).
7. Barnes, W. L., Dereux, A. & Ebbesen, T. W. Surface plasmon subwavelength optics. *Nature* **424**, 824–830 (2003).

8. Zayats, A. V., Smolyaninov, I. I. & Maradudin, A. A. Nano-optics of surface plasmon polaritons. *Phys. Rep.* **408**, 131–314 (2005).

9. Ozbay, E. Plasmonics: merging photonics and electronics at nanoscale dimensions. *Science* **311**, 189–193 (2006).

10. Genet, C. & Ebbesen, T. W. Light in tiny holes. *Nature* **445**, 39–46 (2007).

11. Lee, H.-S., Yoon, Y.-T., Lee, S.-S., Kim, S.-H. & Lee, K.-D. Color filter based on a subwavelength patterned metal grating. *Opt. Express* **15**, 15457–15463 (2007).

12. Laux, E., Genet, C., Skauli, T. & Ebbesen, T. W. Plasmonic photon sorters for spectral and polarimetric imaging. *Nature Photon.* **2**, 161–164 (2008).

13. Diest, K., Dionne, J. A., Spain, M. & Atwater, H. A. Tunable color filters based on metal-insulator-metal resonators. *Nano Lett*. **9**, 2579–2583 (2009).

14. Xu, T., Wu, Y.-K., Luo, X. & Guo, L. J. Plasmonic nanoresonators for high-resolution colour filtering and spectral imaging. *Nat. Commun.* **1**, 59 (2010).

15. Arsenault, A. C, Puzzo, D. P., Manners, I. & Ozin, A. G. Photonic crystal full-colour display. *Nature Photon.* **1**, 468–472 (2007).

16. Kolle, M., Salgard-Cunha, P. M., Scherer, M. R. J., Huang, F., Vukusic, P., Mahajan, S., Baumberg, J. J. & Steiner, U. Mimicking the colorful wing scale structure of the papilio blumei butterfly. *Nature Nanotech*. **5**, 511–515 (2010).

17. Cao, L., Fan, P., Barnard, E. S., Brown, A. M. & Brongersma, M. L. Tuning the color of silicon nanostructures. *Nano Lett.* **10**, 2649–2654 (2010).

18. Zhao, X., Meng, G., Xu, Q., Han, F. & Huang, Q. Color fine-tuning of CNTs@AAO composite thin film ciaisotropically etching porous AAO before CNT and color modification by water infusion. *Adv. Mater.* **22**, 2637–2641 (2010).

19. Coakley, K. M. & McGehee, M. D. Conjugated polymer photovoltaic cells. *Chem. Mater.* **16**, 4533–4542 (2004).

20. Li, G., Shrotriya, V., Huang, J., Yao, Y., Moriarty, T., Emery, K. & Yang, Y. High-efficiency solution processable polymer photovoltaic cells by self-organization of polymer blends. *Nature Mater.* **4**, 864–868 (2005).

21. Park, H. J., Kang, M.-G., Ahn, S. H. & Guo, L. J. Facile route to polymer solar cells with optimum morphology readily applicable to roll-to-roll process without sacrificing high device performances. *Adv. Mater.* **22**, E247–E253 (2010).

22. Chen, H.-Y., Hou, J., Zhang, S., Liang, Y., Yang, G., Yang, Y., Yu, L. Wu, Y. & Li, G. Polymer solar cells with enhanced open-circuit voltage and efficiency. *Nature Photon.* **3**, 649–653 (2009).

23. Kang, M.-G., Park, H. J., Ahn, S. H., Xu, T. & Guo, L. J Toward low-cost, high-efficiency, and scalable organic solar cells with transparent metal electrode and improved domain morphology. *IEEE J. Sel. Top. Quantum Electron.* 16, 1807–1820 (2010).

24. Chen, L.-M., Hong, Z., Kwan, W. L., Lu, C.-H., Lai, Y.-F., Lei, B., Liu, C.-P. & Yang, Y. Multi-source/component spray coating for polymer solar cells. *ACS Nano* **4**, 4744–4752 (2010).

25. Kang, M.-G. & Guo, L. J. Nanoimprinted semitransparent metal electrodes and their application in organic light emitting diodes. *Adv. Mater.* **19**, 1391–1396 (2007).

26. Zia, R., Selker, M. D., Catrysse, P. B. & Brongersma, M. L. Geometries and materials for subwavelength surface plasmon modes. *J. Opt. Soc. Am. B* **21**, 2442–2446 (2004).

27. Dionne, J. A., Sweatlock, L. A., Atwater, H. A. & Polman, A. Plasmon slotwaveguides: towards chip-scale propagation with subwavelength-scale localization. *Phy. Rev. B* **73**, 035407 (2006).

28. Yu, G., Gao, J., Hummelen, J. C., Wudl, F. & Heeger, A. J. Polymer photovoltaic cells: enhanced efficiencies via a network of internal donor-acceptor heterojunctions. *Science* **270**, 1789–1791 (1995).

29. Brabec, C.J., Shaheen, S. E., Winder, C., Sariciftci, N. S. & Denk, P. Effect of LiF/metal electrodes on the performance of plastic solar cells. *Appl. Phys. Lett.* **80**, 1288 (2002).

30. Sunderberg, M., Inganas, O., Stafstrom, S., Gustafsson, G. & Sjogren, B. Optical absorption of poly(3-alkylthiophenes) at low temperatures. *Solid State Commun.***71**, 435–439 (1989).

31. Lungenschmied, C., Dennler, G., Neugebauer, H., Sariciftci, S. N., Glatthaar, M., Meyer, T. & Meyer, A. Flexible, long-lived, large-area, organic solar cells. *Sol. Energy Mater. Sol. Cells* **91**, 379–384 (2007).

32. Kang, M.-G., Park, H. J., Ahn, S. H., & Guo, L. J. Transparent Cu nanowire mesh electrode on flexible substrates fabricated by transfer printing and its application in organic solar cells. *Sol. Energy Mater. Sol. Cells* **94**, 1179–1184 (2010).

CHAPTER 8

Conclusion

8.1 Summary of thesis

I have suggested the ways to realize low-cost, high efficiency and scalable Organic solar cell (OSC) in this thesis. For this purpose, my research has been focused on various nanostructures, which we have to control for better performance of OSCs or we can apply to maximize the performances of OSCs, and the effective fabrication processes to achieve those nanostructures. The novel device concepts based on those nanostructures have been also introduced.

First part of my research is about the control of the nanostructures in photoactive layers to develop more efficient OSC devices. I have developed a new process named as evaporation of solvent through surface encapsulation and with induced alignment of polymer chains by applied pressure (ESSENCIAL) inducing the optimized nanoscale bulk heterojunction (BHJ) morphology. The OSCs fabricated by this process showed the superior performances compared with conventional spin-casting based BHJ OSCs treated by thermal and solvent annealing. Moreover, this process was extended to high-speed roll-to-roll process even without sacrificing high device performance. A new type of heterojunction nanostructures based on bilayer concept was also developed. By maximizing interdiffusion of donor and acceptor, I could realize the optimized heterojunction morphology of donor and acceptor having internal quantum efficiency

approaching about 100%. Furthermore, for ideal interdigitated heterojunction nanostructure, sub-20 nm scale conjugated polymer nanopillars were successfully fabricated. Secondly, various nanostructures such as plasmonic nanostructures and light trapping structures were developed to enhance the absorption of light in OSC devices. OSCs with those nanostructure showed the improved power conversion efficiency (PCE). Lastly, the dual-function devices working as color filter and solar cell were developed by applying photonic nanostructures to OSCs. This new conceptual device can recycle the wasted energy in color filter to generate the electricity for the revolutionary energy-saving e-media. I expect that this device can suggest alternative application of OSCs, which complements the great efforts in improving PCE and practical fabrication methods.

8.2 Summary of specific achievement

The nanostructures in photoactive layer were controlled to give better exciton generation, dissociation, and transportation, resulting in higher PCE. Non-uniform vertical distribution of donor and acceptor BHJ in OSCs, which is inevitably generated by conventional spin-casting based thermal and solvent annealing methods, was solved by ESSENCIAL process inducing much uniform vertical distribution of components. The BHJ photoactive layer fabricated by ESSENCIAL process showed higher crystallinty and superior charge transportation property (hole mobility: 1.26×10^{-3} $cm^2\ V^{-1}\ s^{-1}$, electron mobility: 1.46×10^{-3} $cm^2\ V^{-1}\ s^{-1}$) compared with those fabricated by conventional spin-casting based annealing process (hole mobility: 3.29×10^{-4} $cm^2\ V^{-1}\ s^{-1}$, electron mobility: 4.95×10^{-4} $cm^2\ V^{-1}\ s^{-1}$). The charge balance (electron mobility / hole mobility) was improved from 1.50 to 1.16. AFM and PL also showed that the excitons were much

efficiently dissociated in BHJ photoactive layer fabricated by ESSENCIAL process. Consequently, the PCE of P3HT:PCBM system OSCs fabricated by ESSENCIAL process was improved from 3.23 % (J_{sc} = 8.14 mA cm^{-2}, V_{oc} = 0.61 V, FF = 65.1 %, R_s = 3.3 Ω cm^2, conventional thermal annealing) to 4.46 % (J_{sc} = 10.68 mA cm^{-2}, V_{oc} = 0.60 V, FF = 69.1 %, R_s = 1.2 Ω cm^2) under AM 1.5 G / 100 mW cm^{-2} condition. The OSCs fabricated by roll-to-roll process, extended version of small scale ESSENCIAL process, showed similar PCE (J_{sc} = 10.59 mA cm^{-2}, V_{oc} = 0.60 V, FF = 67.3 %, R_s = 1.4 Ω cm^2, PCE = 4.40 %) without sacrificing high device performances. The solar cells fabricated by roll-to-roll processing were prepared even without PEDOT:PSS layer.

The additional thin C_{60} buffer layer between photoactive layer and LiF/Al cathode solve the charge imbalance problem in thick BHJ layer (over 300 nm), improving the electron mobility in cathode side and decreasing contact resistance for better charge transportation. Using this buffer layer, I could further increase the PCE of P3HT:PCBM system BHJ OSCs to 5.50 % (J_{sc} = 14.53 mA cm^{-2}, V_{oc} = 0.58 V, FF = 64.8 %).

A new type of bilayer-based heterojuntion photoactive layer fabricated by maximizing the interdiffusion of donor and acceptor have significantly improved the crystallinity of nanodomains for better charge transportation and decreased bimolecular recombination compared with BHJ structures. Resultant OSC devices having internal quantum efficiency about 100 % showed the ultrahigh short circuit current (15.10 mA cm^{-2}), ultimately giving 5.15 % PCE based on P3HT:PCBM system.

Sub-20 nm scale SiO_2 nanopillar and nanohole structures were developed using polystyrene (PS) nano-template fabricated by block copolymer self-assembly. Using

nanoimpront lithography (NIL) sub-20 nm conjugated polymer nanopillars were successfully fabricated to realize the ideal interdigitated heterojunction photoactive layer.

In order to increase the absorption of light in given photoactive layer, plasmonic nanostructure and light trapping structures were introduced in OSC devices using NIL-based nanofabrication. The P3HT:PCBM system BHJ OSCs showed improved PCE from 3.31 % (J_{sc} = 8.53 mA cm^{-2}, V_{oc} = 0.62 V, FF = 62.6 %) to 3.66 % (J_{sc} = 9.58 mA cm^{-2}, V_{oc} = 0.60 V, FF = 63.5 %) after introducing plasmonic nanostructures to OSCs. The light trapping structure also improved PCE from 3.36 % (J_{sc} = 8.84 mA cm^{-2}, V_{oc} = 0.60 V, FF = 63.2 %) to 4.16 % (J_{sc} = 10.85 mA cm^{-2}, V_{oc} = 0.60 V, FF = 63.8 %).

The dual-function devices working as color filters and solar cell were developed for versatile application of OSCs in display. Three types of devices showing cyan, magenta and yellow reflective colors were designed to demonstrate CMY color system and those are efficiently worked as solar cells. (cyan: J_{sc} = 5.28 mA cm^{-2}, V_{oc} = 0.51 V, FF = 57.5 %, PCE = 1.55 %; magenta: J_{sc} = 5.04 mA cm^{-2}, V_{oc} = 0.49 V, FF = 33.1 %, PCE = 0.82 %; yellow: J_{sc} = 3.98 mA cm^{-2}, V_{oc} = 0.48 V, FF = 31.2 %, PCE = 0.60 %).

I believe that all of the technologies addressed in this work can pave ways to realize low-cost, high efficiency and scalable OSCs.